UNIVERSITÀ DELLA CALABRIA

Ph.D thesis in joint supervision

La physique de la particule à la matière condensée (France)

Scienze e Tecnologie delle Mesofasi e dei Materiali Molecolari (Italy)

Presented by

M. Said Houmadi

To obtain grade of

DOCTEUR de l'UNIVERSITÉ PIERRE ET MARIE CURIE – FRANCE

DOTTORE DI RICERCA DEL'UNIVERSITA' DELLA CALABRIA - ITALY

Atomic force microscopy study of physico-chemical and nanotribological properties of hydrophobin protein

Presented on January 10th 2010

Mr. Michele Giocondo CNR – University of Calabria – Italy (Supervisor)

Ms. Emmanuelle Lacaze CNRS – University Pierre and Marie Curie (Supervisor)

Approved by:

Mr. Ugo Zammit Associate professor - University of Rome Tor Vergata (Reviewer)

Ms. Sophie Cantin rivière Maître de conférence - Cergy Pontoise University (Reviewer)

Ms. Régine Perzynski Professor - University Pierre and Marie Curie (Examiner)

Mr. Stefano Corni Researcher INFM - University of Modena and Reggio Emilia (Examiner)

Université Pierre & Marie Curie - Paris 6
Bureau d'accueil, inscription des doctorants et base de données
Esc G, 2ème étage
15 rue de l'école de médecine
75270-PARIS CEDEX 06 - France

Università della Calabria
Campus di Arcavacata
BTSST cubo 31 c
via Pietro Bucci
87036 Arcavacata di Rende (CS)
Italy

Table of contents

Introduction

1. Hydrophobins p.1

1.1 Definition of hydrophobins p. 1

1.2 Classification of hydrophobins p. 2

1.3 Amphiphilic character of hydrophobins p. 4

1.4 Description of some hydrophobins p. 5

1.5 Potential applications of hydrophobins p. 6

1.6 Aggregation of hydrophobins p. 7

1.6.1 Rodlets formation p. 7

1.6.2 Self-assembly in solution p. 9

1.6.3 Ordered structure of hydrophobin films p. 10

1.7 Protein purification p. 10

1.8 Aims of the study p. 12

Bibliography p. 12

2. Langmuir technique p. 17

2.1 Brief history of Langmuir films p. 17

2.2 Langmuir films p. 18

2.2.1 Thermodynamic properties of Langmuir Film p. 19
2.2.2 Surface pressure p. 21
2.2.3 Isotherm p. 23
2.3 Film transfer on solid substrate p. 26
2.3.1 Langmuir-Blodgett deposition p. 26
2.3.2 Langmuir-Schaefer (LS) deposition p. 27
2.4 Surface pressure feedback control p. 28
2.5 Substrates Preparation p. 29
Bibliography p. 30

3. Atomic Force Microscopy p. 31
3.1 Introduction p. 31
3.2 Principles of AFM p. 31
3.3 AFM probes p. 32
3.4 Imaging modes p. 34
3.4.1 Review of Harmonic Oscillators p. 34
3.4.2 Modeling the AFM Cantilever p. 36
3.4.3 Non contact resonant mode p. 37
3.4.4 Tapping Mode p. 38
3.4.5 Topography imaging p. 41
3.4.6 Phase imaging p. 43
3.5 Atomic force spectroscopy p. 46
3.5.1 Amplitude phase distance curves p. 46
3.5.2 Amplitude dependence on tip-sample distance p. 48
3.5.3 Phase distance curve p. 50

3.6 Contact mode p. 51
3.6.1 Calibration of the cantilever deflection p. 53
3.6.2 Force curves measurements p. 54
3.6.3 Friction p. 55
Bibliography p. 59

4. Langmuir films of hydrophobin protein from *Pleurotus ostreatus* p. 61
4.1 Introduction p. 61
4.2 Experimental procedure p. 63
4.3. Theoretical basis p. 64
4.4 Results and discussion p. 65
4.4.1 Analysis of Langmuir film at the air-water interface p. 65
4.4.2 Characterization of deposited hydrophobin films p. 71
4.4.2.1 Modification of wetting properties of surfaces p. 73
4.4.3 Characterization of Hydrophobin LB film transferred onto SiO_2 surface after repeated compression p. 76
4.4.3.1 A possible model for rodlets formation p. 79
4.4.3.2 Imaging of hydrophobin LB film in dry conditions p. 81
4.5 Conclusion p. 83
Bibliography p. 83

5. Beyond Topography using force spectroscopy measurements p. 87

5.1 Introduction p. 87
5.2 Experimental procedure p. 89
5. 3 Theoretical aspect of the tip-sample interactions p. 90
5.3.1 Van der Waals force p. 90
5.3.2 Wetting phenomenon and capillary forces p. 95
5.3.2.1 Introduction p. 95
5.3.2.2 Theory p.98
5.3.3 Energy Dissipation p.100
5.4 Results and discussion p.101
5.4.1 Determination of Hamaker constant p.101
5.4.2 Local wettability of hydrophobin films p. 105
5.4.2.1 Wetting properties of hydrophobin LS monolayer p. 105
5.4.2.2 Wettting properties of hydrophobin LB monolayer p. 110
5.4.3 Phase distance curves and visco-elastic properties p.112
5.4.3.1 Phase distance curves at ambient humidity p. 112
5.4.3.2 Phase distance curves in dry conditions p. 114
5.4.3.3 Adhesion force on hydrophobin films p.116
5.4.3.4 Energy dissipation between the tip and hydrophobin film p. 118
5.4.3.5 Validation of the assumption by numerical simulations p. 119
5.4.4 Phase distance curves on hydrophobin LB monolayer and rodlets p. 120
5.5 Conclusion p. 123
Bibliography p. 124
6. Nanotribological properties of hydrophobin films p. 128
6.1 Introduction p. 128
6.2 Friction at nanoscale p. 129

6.3 Experimental procedure p. 131

6.4 Results and discussions p. 132

6.4.1 Frictional properties of hydrophobin monolayers in ambient humidity p. 132

6.4.2 Effect of relative humidity on the of friction coefficient for hydrophobin films and SiO_2 Surfaces p. 136

6.4.3 Frictional properties of hydrophobin bilayers p. 140

6.5 Conclusion p. 143

Bibliography p. 144

7. Conclusion p. 146

Introduction

The science at the nanoscale is one of the most important growth areas of this century. It is a multidisciplinary field covering atomic, molecular and solid state physics, as well as much of chemistry and biological materials. Nanostructures are known to exhibit novel and improved material properties, fundamentally because the physical and chemical properties are very different when dimensions are reduced to the nanometer scale.

Local probe microscopy techniques have been developed for material characterization at the nanoscale level. One of the most important and popular techniques for nano-materials study is the atomic force microscopy (AFM). AFM is a high-resolution imaging technique that allows to obtain information about samples at the local scale. In biology for example AFM offers the prospect of high resolution images of biological material, images of molecules and their interactions even under physiological conditions. My work is related to investigation of thins films of protein prepared via the Langmuir technique using atomic force microscopy as well as atomic force spectroscopy.

I have focused the study on hydrophobion protein from the fungus *Pleurotus ostreatus* by investigating physical and tribological properties of well controlled hydrophobin films. The goal was to obtain information on the structure of hydrophobin assemblies, with the motivation of a deeper understanding of the assemblies structure and of the surface properties of this protein, mainly using the AFM technique. More specifically, the precise aims of the study can be stated as follows:

- Establishing the right experimental conditions enabling the studies of thin hydrophobin films using Langmuir trough. In particular, it consists in finding a way to study the self assembled hydrophobin films at the air-water interface as Langmuir

films and when deposited on solid hydrophilic/hydrophobic substrates as Langmuir-Blodgett films and Langmuir-Schaeffer films. The interest in Langmuir film is indeed associated with the fact that their geometry is controlled, at least better controlled than usual films, obtained through incubation procedure.

- Characterizing the obtained hydrophobin films using atomic force spectroscopy measurements, by performing the approach-retract curves in tapping mode and hence analyzing amplitude and phase versus tip-sample distance. This will allow to probe the local wettability and mechanical properties of obtained hydrophobin films using AFM probe.
- Investigating the nano-tribological properties of obtained films by analyzing the friction between AFM tip and surface of films. The goal consists then to analyze the possibility of using hydrophobin as coating agents of low friction.

This thesis is organized as follows:

In the chapter 1, I present a general overview about hydrophobin proteins and about the previous work carried out in order to understand their molecular structure, the self-assemblies that can form . Indeed, due to their specific properties, many study have been devoted to the investigation about the hydrophobins assemblies.

In the chapter 2, I present a description of the Langmuir technique, which I have used in my thesis for hydrophobin film deposition.

In the chapter 3, I present the atomic force microscopy technique, and I describe the different operating mode AFM.

In the chapter 4, I have presents results about Langmuir films at the air water interface as well as when deposited onto hydrophilic and hydrophobic substrates.

Chapter 5 reports on characterization of hydrophobin films using force spectroscopy measurements in order to probe the locale properties of the protein monolayers including wetting and visco-elasticity.

In the chapter 6, results about frictional properties of hydrohobin films at the nanoscale level are presented.

We were then able to probe the local properties of hydrophobin films and we have revealed using AFM in tapping mode a viscio-elastic difference between hydrophobin LS film and hydrophobin LB film.

We have demonstrated that the by AFM one can have more information about the properties of samples beyond the topography.

1. Hydrophobins

1.1 Definition of hydrophobins

In order to study and understand the physical aspect of hydrophobin proteins, it is necessary to present some biological properties of hydrophobins. They are a family of small proteins that are secreted by fungi; they are amphiphilic, thus characterized by hydrophilic and hydrophobic areas dispersed on their surface [1]. Hydrophobins have been described as the most surface active proteins known [2]. Here, the term "surface activity" refers to a tendency to adsorb to surfaces and interfaces, such as the air-water interface. In fungi, hydrophobins seem to play several different roles. In particular, they help the fungi to survive in and adapt to the environment [1], mainly because of their remarkable structural characteristics, they fulfill various structural roles including that focused on pharmaceutical and other medical applications [3, 4]. Hydrophobins work as coatings, adhesive agents and they self-assemble at air-water interfaces into amphipathic films with the hydrophobic side exposed to the air [5, 6]. Thus, of primary interest of hydrophobins is their ability to interact with surfaces, coating the surfaces [7], modifying their hydrophilicity and lowering surface tension [8]. Many works have been devoted to the study of these hydrophobins, in particular, in order to understand the structure of different assembly states of the molecules and their relation with hydrophobicity.

1.2 Classification of hydrophobins

In order to understand the current research on hydrophobins it is essential to know that early results led to the classification of hydrophobins into two

classes, class I and class II. In fact, all hydrophobins have a large proportion of hydrophobic residues and contain eight cysteines. The classification of proteins is then based on the distribution of the cysteines and the occurrence of hydrophilic and hydrophobic amino acid residues in the protein sequence. Another classification is associated with their hydropathy plots, as well as on the properties of the formed aggregates [9]. Class I hydrophobin biofilms are not disrupted when treated with surfactants, solvents, and denaturing agents [9, 10]. They are very stable and strongly interact with hydrophobic solids [11]. Only trifluoroacetic acid (TFA) has been found to dissociate the corresponding supramolecular structures [10]. On the other hand, films formed by class II hydrophobins are easily disrupted with surfactants or solvent mixtures such as 60% ethanol/water [12]. Sequences of a representative subset of class I and class II hydrophobins is illustrated in the figure 1 taken from ref. [13]. Class II hydrophobins are generally smaller than class I proteins (ca. 70 residues versus ca. 85–95 residues) and display substantially more sequence similarity to one another [1].

Figure 1. Amino acid sequence comparison of class I and class II hydrophobins. Only amino acids between the first and last Cys residues are shown due to high sequence variation outside this region. The conserved Cys residues are highlighted in yellow, with the conserved disulfide bonding pattern indicated with brackets.

A common feature of hydrophobins is that they are small proteins, containing around 100 amino acids. The primary sequence is characterized by a conserved

pattern of eight cysteine residues [14, 15, 16]. By comparing amino acid sequence of class I and class II hydrophobins shown in figure above, Kwan et al [13] have shown that the length of the polypeptide segments between cysteines 3 and 4 (the Cys3–Cys4 loop) and that between cysteines 4 and 5 (the Cys4–Cys5 loop) are fully conserved in class II hydrophobins, and the other inter-cysteine regions are also well conserved. In contrast, class I hydrophobins display much greater sequence variation. In particular, the length of the inter-cysteine regions is highly variable. This could be related to the difference between the assemblies formed by class I on one hand and class II on the other hand. Indeed, in studies of the air–water interface it was observed that some hydrophobins from class II such as HFBI and HFBII assemble into films that can present a very ordered structure of nanometer dimensions [1, 17] (see figure 3B).

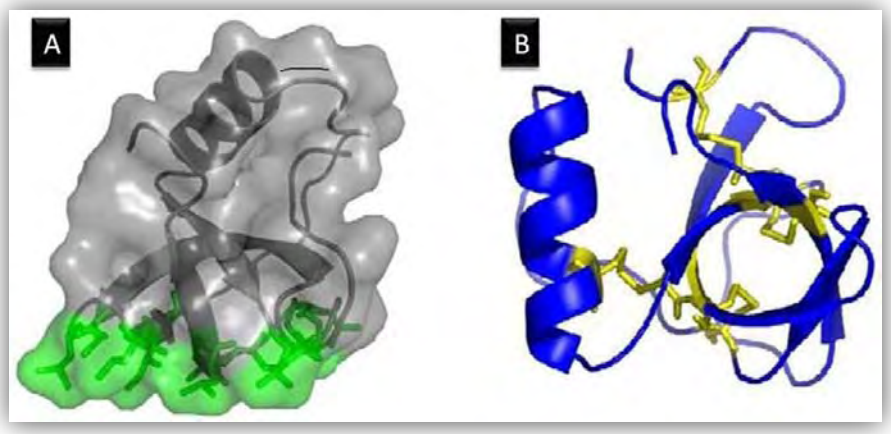

Figure 2. Structure of HFBII hydrophobin. The hydrophobic patch is shown in green, with the rest of the hydrophilic surface in light grey. The exposed hydrophilic side chains give the molecule the character of an amphiphile. B). a small antiparallel β-barrel formed by two β-hairpins connected by a stretch of α-helix [18].

On the other hand, rodlets formation is characteristic of class I hydrophobins such as SC3 (see figure 3A). Rodlets are typically formed when a solution of hydrophobin is dried down on a solid surface, and appear to be formed at the air–water interface [1]. In addition, aggregates of SC3 hydrophobin have been

identified in solution, but the details of this association in solution are not known [5].

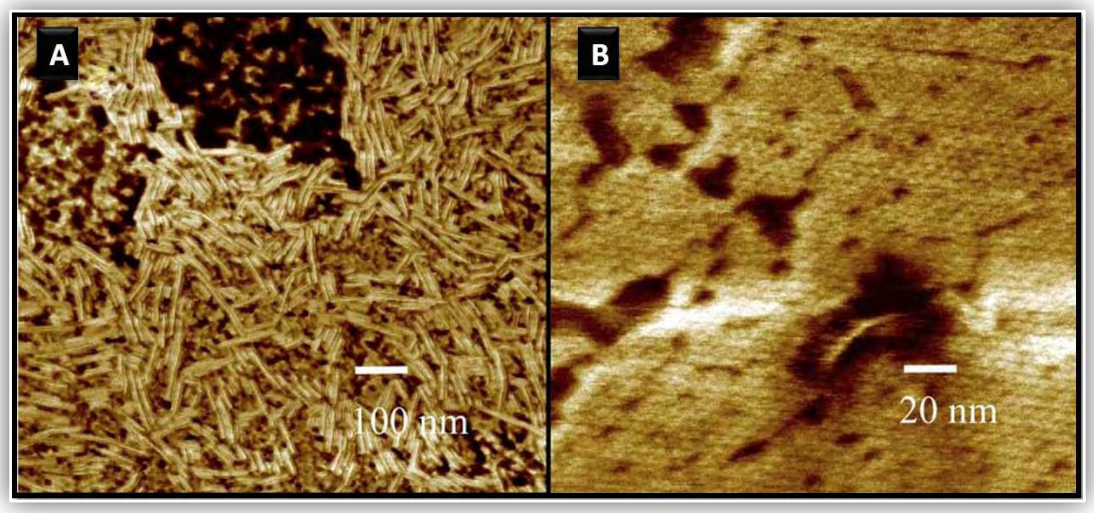

Figure 3. Supramolecular assemblies of hydrophobins. A) An atomic force microscopy (AFM) image of a S. commune SC3 sample showing rodlets. The sample was prepared by drying down a solution of protein on a sheet of mica. B) An (AFM) image of a surface membrane of HFBI class II hydrophobin showing an ordered structure. The film was formed at the air–water interface and lifted onto mica using the Langmuir–Blodgett technique. Images taken from ref. [1].

1.3 Amphiphilic character of hydrophobins

The important feature of the protein is that one side of the hydrophobin consists solely of hydrophobic aliphatic side chains that form a planar hydrophobic patch whereas the other protein side is mostly hydrophilic. Furthermore, Linder [18] has described the formation of hydrophobic patch of HFBII hydrophobin that is formed to a large extent by two loop regions in the central β-barrel structure and contains only aliphatic residues. He explained that these surface hydrophobic residues form about half of all hydrophobic residues in the protein. This is remarkable, because usually hydrophobic residues are buried in the core of proteins stabilizing the folded conformation of proteins. This amphiphilic and rigid structure is believed to be responsible for the hydrophobins interfacial properties [19]. The hydrophobin structure could then be described to look like any surfactant with one hydrophobic and one

hydrophilic part, only the size and structural details (see figure 2) are very different from typical surfactants. In fact, the diameter of the protein is approximately 2.5 - 3 nm [18, 5].

1.4 Description of some hydrophobins

The most studied class I hydrophobins to date are SC3 from *Schizophyllum commune*, and EAS; from *Neurospora crassa*, on the other hand HFBI and HFBII from Trichoderma reesei are the most studied class II hydrophobins. On the other hand, the molecular structure of vmh2 class I hydrophobin is not well known to date. Indeed, Penas and co-workers [20] have investigated the primary structures and expression of hydrophobins from *Pleurotus ostreatus* with the aim of understanding their different functions. They found that the family of genes coding for these proteins was more complex than expected. They suggested that their function should be related not only to the molecular structure but also regulated by time or developmental stage.

Hydrophobins have functions in biology that are not well understood. Also the relationship between molecular structure and self assemblies or aggregations is not well understood. Thus an important step towards the understanding of hydrophobins function came with the first crystallographic structure. The molecular structure of the class II hydrophobins HFBI and HFBII has been described by Hakanpaa et al [14, 15] (see the molecular structure of HFBII in figure 2). The crystal structures of HFBI and HFBII have provided valuable insights into the molecular basis for the surface properties of hydrophobins. However, in some senses the class I proteins are more striking, because of the robustness and regularity of the rodlet layer that they form [21].

Tripleresonance NMR method has been used to determine the molecular structure of the class I hydrophobin EAS [16]. By NMR study of this protein it

has also been suggested that the EAS hydrophobin is largely unstructured in solution, showing only a small region of β-sheet structure [22]. In addition, Zangi et al [23] have proposed that the protein refolds at hydrophobic-hydrophilic interfaces. Similarly, studies on the SC3 hydrophobin have suggested that the protein has different conformational states and different secondary structure contents when in solution [24, 25]. This change in conformation allows likely hydrophobin molecules to form different assemblies that are very important for biotechnological perspectives.

1.5 Potential applications of hydrophobins

When the hydrophobin membrane is transferred onto a substrate, the wettability of this surface can be controlled, and hydrophobic behavior can be converted into hydrophilic behavior, and vice versa [6, 26, 27, 28]. De Stefano and co-workers [29] have demonstrated that the hydrophobin membrane protects the silicon nanocrystalites from basic dissolution in NaOH, and leaves unaltered the sensing ability of porous silicon optical microcavity that works as an optical transducer for vapor and liquid detection. This consequently adds chemical stability, which can be key in biomolecular experiments. It has been also demonstrated that rodlets may be formed in vitro on both hydrophobic and hydrophilic substrates with the like face of the rodlets adhering to the surface and the other face directed outwards [27]. Thus, for example, hydrophobic surfaces may be coated with rodlets or hydrophobin layer to allow the subsequent attachment of cells or proteins in biosensor design, or to increase their biocompatibility in applications such as tissue engineering. The latter use would be assisted by the observation that humans have been ingesting hydrophobins from mushrooms and other edible fungi for many years without apparent side effects [30].

1.6 Aggregation of hydrophobins

1.6.1 Rodlets formation

The important characteristic of class I hydrophobins is their capability to form rodlets [31]. The formation of this rodlet-like film is accompanied by β-sheet-state structure formation, as detected by de Vocht et al. [25] using polarization-modulation infrared reflection absorption spectroscopy (PM-IRRAS). In effect, PM-IRRAS has been used to study the self-assembly of SC3 directly at the air–water interface. SC3 accumulates rapidly at the air–water interface and is seen to undergo a conformational transition from a mixture of secondary structure elements to a mainly β-sheet form. On the other hand, Yu et al. [33] have investigated the HGFI class I hydrophobin from *Grifola Frondosa* using Langmuir trough and found that rodlets are formed at the air–water interface after repeated compression cycles of a surface film of HGFI. This suggests that energy is necessary to form rodlets.

In reference [25], authors give information about the orientation of secondary structure elements in a sample, relative to the incident surface. They indicated by PM-IRRAS spectra from SC3 rodlets, collected from the interface, that the hydrogen bonds are oriented preferentially parallel to the air– water interface. Since the hydrogen bonds lie in the plane of the β-sheet, this indicates that the β-sheets in the SC3 rodlets are parallel to the surface and therefore also co-planar with the long axis of the rodlets. Askolin [32] has proposed that rodlets formation is caused by conformational changes of the hydrophobin molecules together with intermolecular interaction (figure 4A). He suggested that the reason for the conformational change may be stabilization of the hydrophobin film by strengthening of the interaction between individual molecules. He proposed a model for rodlets based on the formation of rodlets as a monolayer.

The proposed model is supported by the observations of de Vocht and co-workers [3] indicating that changes in secondary structure of SC3 occur prior to rodlet formation. However most of the models suggest that the rodlets are formed as a monolayer. Kwan et al. [16] have equally proposed a model for the rodlets structure adopted by the class I hydrophobin EAS (figure 4B). In this model the rodlets form a monolayer of interacting molecules at the air-water interface with a hydrophobic side that faces air and a hydrophilic side that contacts water.

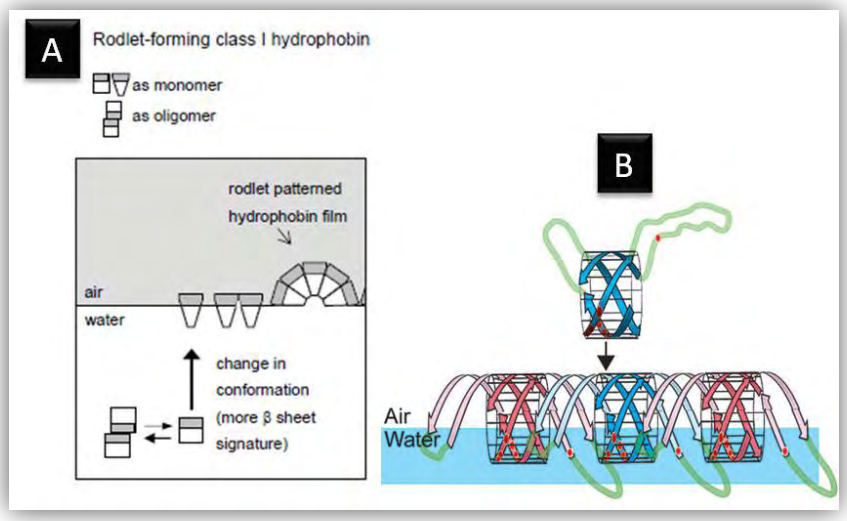

Figure 4. Models of rodlets formation: (A) is taken from [32] and (B) from [16]

However all of these structural studies need to reconcile the models for hydrophobin conformation with the measured thickness of rodlets. The thickness of the SC3 monolayer has been reported several times. de Vocht et al. [36] used scanning force microscopy and estimated that the rodlets, had an average diameter of 9–15 nm. This suggests that the rodlets thickness is about 9-15 nm if they have a cylindrical form. These results are supported by other studies of class I hydrophobins, which generally report rodlet diameters for class I hydrophobins of about 10 nm [1]. However, Wösten et al. [37] have calculated the occupied area by SC3 molecule on Teflon on one hand and at the

water–air interface on the other hand, concluding that, SC3 would occupy about 7 nm^2 if spherical, suggesting that the protein should adopt an extended conformation when it forms rodlet if the rodlets thickness is indeed about 10 nm. Moreover, these values are in contradiction with the results reported by Wang et al. [38] for SC3 hydrophobin using ellipsometry measurements. They determined the thickness of a membrane formed at an air-water interface after several hours of incubation. When protein concentration was high (100 mg/ml), the membrane thickness after 10 min was determined to be 2.3 nm, and it slowly increased to the maximum of 3 nm after 5 hours incubation. This difference may be due to the fact that the membrane formed at low protein concentration is less compact; either a larger space exists between molecules, or the orientation of the protein in the membrane is different.

The difference in the obtained values for rodlets thickness reported in the references [1, 36, 37] on one hand and [38] on the other hand, anyway, it remains possible that in [38] , the rodlet film is still not fully compact for 100 mg/ml finally suggests that the rodlets are not cylindrical but their width is probably larger than thickness.

1.6.2 Self-assembly in solution

The hydrophobin SC3 self-association in water was also investigated. Martin et al. [34] have reported utilizing dynamic light scattering, that complexes ranging from approximately 100 to 200 nm diameter were formed in solution at low concentrations of the protein (1 μg/mL). At higher concentrations (4-10 μg/mL), an additional population of aggregates in the micrometer range was observed. The size of the loosely associated structures in solution was shown to be dependent on the protein concentration; surface tensiometry experiments showed a critical aggregation concentration of approximately 1 μg/mL.

1.6.3 Ordered structure of hydrophobin films

AFM studies of HFBI and HFBII films produced by the Langmuir–Blodgett technique have also reported by Paananen et al [35], they have shown highly crystalline domains of the hydrophobins with regular features and a monolayer height of about 1.3 nm. Elsewhere, significant structural insight into class II hydrophobin films has been achieved with high resolution AFM studies of HFBI variants where the monolayer films have been probed from both the hydrophobic and hydrophilic sides [17]. These class II hydrophobin layers do not have a rodlet-like morphology but instead display a striking hexagonal repeating pattern that arises spontaneously at the air–water interface.
Concerning the thickness question, as noted above, Paananen and coworkers [35] have reported the thickness of a class II hydrophobin layer to be 1.3 nm. Szilvay et al. [17] report thicknesses of 1.3–2.8 nm, depending on the manner of preparation of the film and conclude that the films are monomolecular layers, with the diameter of the globular, soluble form of HFBI being 2–3 nm.

In order to have idea about the rodlets size, it is reasonable to compare their thickness to that of monolayer formed by class II hydrophobin which is about 2-3 nm thick. In doing this, and in taking into account the thickness reported in [1, 36, 37] it can be concluded that if a hiegh thickness for rodlets would be confirmed, the rodlets should be formed as multilayer or the molecules of class I hydrophobin adopt an extended shape when they form rodlets.

1.7 Protein purification

In this thesis, I have investigated physical and nanotribological properties of vmh2 class I hydrophobin purified from the fungus *Pleurotus ostreatus*. It has

been purified in the group of Pr P. Giardina at the department of Organic Chemistry and Biochemistry, Federico II University, Naples- Italy.

White-rot fungus, *P. ostreatus* (Jacq.:Fr.) Kummer (type: Florida) (ATCC no. MYA-2306) was maintained through periodic transfer at 4 °C on potato dextrose agar (Difco) plates in the presence of 0.5 % yeast extract (Difco). Mycelia were inoculated (by adding six agar circles of 1 cm diameter) in 2 l flasks containing 500 ml potato dextrose (24 g/l) broth supplemented with 0.5% yeast extract (PDY) or 2% malt extract (ME) and grown at 28 °C in static cultures.

After 10 days of fungal growth, mycelia were removed by filtration and hydrophobins released into the medium were aggregated by air bubbling using a Waring blender. Foam was then collected by centrifugation at 4,000 x *g*. The precipitate was freeze-dried, treated with TFA for 2 hours and sonicated for 30 min. After centrifugation at 3200 x *g* for 20 min, the supernatant was dried again in a stream of air, and then dissolved in water (Hyd-w) or 60% ethanol (Hyd-et). In the latter case, the solution was kept at 4 °C overnight and then centrifuged at 3200 x *g* for 10 min. Before use the protein was always disassembled with pure TFA, dried, and then the monomeric protein dissolved. Protein concentration was evaluated by bicinchoninic acid (BCA) assay (Pierce, Rockford, IL) using bovine serum albumin as standard or evaluated by measuring the absorbance band at 280 nm, using a value of ε=1.44 ml mg^{-1} cm^{-1}, when the hydrophobin was dissolved in EtOH solution. This extinction coefficient has been estimated on the basis of the concentration determined using the protein dissolved in water and tested by BCA assay. Molecular mass of the protein (8568 Da) has been determined by MALDI TOF (Voyager-DE STR, Applied Biosystems) analysis.

1.8 Aims of the study

In this thesis work in a broad sense, the aim was to investigate the hydrophobin protein in order to obtain information on the structure of hydrophobin assemblies, with the motivation of a deeper understanding of the surface properties of the vmh2 class I hydrophobin from the fungus *pleurotus ostreatus*, mainly, using the AFM technique. More specifically, the precise aims of the study can be stated as follows:

- Establishing the right experimental conditions enabling the studies of thin hydrophobin films using Langmuir trough. In particular, it consists in finding a way to study the selfassembled hydrophobin films at the air-water interface as Langmuir films and when deposited on solid hydrophilic/hydrophobic substrates as Langmuir-Blodgett films and Langmuir-Schaeffer films.
- Characterizing the obtained hydrophobin films using atomic force spectroscopy measurements, by performing the approach-retract curves in tapping mode and hence analyzing amplitude and phase versus tip-sample distance.
- Probing the local wettability and mechanical properties of obtained hydrophobin films using AFM probe.
- Investigating the nano-tribological properties of obtained films by analyzing the friction between AFM tip and surface of films.

Bibliography

[1] Linder, M. B.; Szilvay, G. R.; Nakari-Setälä, T.; Penttilä, M. E. *FEMS Microbiol. Re*V. **2005**, *29*, 877–896

[2] Askolin S, Linder M, Scholtmeijer K, Tenkanen M, Penttila M, de Vocht ML, et al. Interaction and comparison of a class I hydrophobin from Schizophyllum

commune and class II hydrophobins fromTrichoderma reesei. Biomacromolecules 2006;7:1295–301.

[3] de Vocht, M. L.; Reviakine, I.; Wösten, H. A.; Brisson, A.; Wessels, J. G.; Robillard, G. T. *J. Biol. Chem.* **2000**, *275*, 28428-28432.

[4] Wösten, H. A.; de Vocht, M. L. *Biochim. Biophys. Acta* **2000**, *1469*

[5] X. Wang, J. F. Graveland-Bikker, C. G. De Kruif, G. T. Robillard, *Protein Science* (2004), 13:810–821

[6] Wösten, H.A.B., Schuren, F.H.J., and Wessels, J.G.H. 1994.. *EMBO J.* **13:** 5848–5854

[7] Paul A. Stroud, J. Shawn Goodwin, Peter Butko, Gordon C. Cannon, and Charles L. McCormick. Biomacromolecules, Vol. 4, No. 4, 2003 **957.**

[8] S. O. Lumsdon, J. Green, B. Stieglitz, Colloids and Surfaces B: Biointerfaces 44 (2005) 172–178

[9] Wessels JGH. Annu Rev Phytopathol 1994;32:413–37.

[10] de Vries, O.M.H., kkkes, M.P., Wosten, H.A.B., and Wessels, J.G.H. (1993). lnsoluble hydrophobin complexes in the walls of Scbizopby/- /*um* commune and other filamentous fungi. Arch. Microbiol. 159, 330-335.

[11] M. I. Janssen, M. B. M. van Leeuwen, K. Scholtmeijer, T. G. van Kooten, L. Dijkhuizen, H. A. B. Wöste, Biomaterials 23 (2002) 4847–4854

[12] Russo, P. S.; Blum, F. D.; Ipsen, J. D.; Yusuf, J. A.; Miller, W. G. *Can. J. Bot.* **1982**, *60*, 1414–1422.

[13] Ann H. Kwan, Ingrid Macindoe, Paul V. Vukašin, Vanessa K. Morris, Itamar Kass, Rima Gupte, Alan E. Mark, Matthew D. Templeton, Joel P. Mackay and Margaret Sunde, J. Mol. Biol. (2008) 382, 708–720

[14] Hakanpää J, Szilvay, G.R., Kaljunen, H., Maksimainen, M., Linder, M., Rouvinen, J., 2006. Two crystal structures of Trichoderma reesei hydrophobin HFBI—The structure of a protein amphiphile with and without detergent interaction. Protein Sci. 15, 2129–2140.

[15] Hakanpaa J, Paananen A, Askolin S, Nakari-Setala T, Parkkinen T, Penttila M, et al. Atomic resolution structure of the HFBII hydrophobin, a self-assembling amphiphile. J Biol Chem 2004;**279**: 534–539.

[16] Kwan, A., Winefield, R.D., Sunde, M., Matthews, J.M., Haverkamp, R.G., Templeton, M.D., Mackay, J.P., 2006. Structural basis for rodlet assembly in fungal hydrophobins. Proc. Natl. Acad. Sci. U.S.A. 103, 3621–3626.

[17] Szilvay, G. R.; Paananen, A.; Laurikainen, K.; Vuorimaa, E.; Lemmetyinen, H.; Peltonen, J.; Linder, M. B. *Biochemistry* **2007**, *46*, 2345–2354.

[18] Linder MB, Hydrophobins: Proteins that self assemble at interfaces, Curr Opin Colloid Interface Sci (2009), doi:10.1016/j.cocis.2009.04.001

[19] Géza R. Szilvay, Kaisa Kisko, Ritva Serimaa, Markus B. Linder, FEBS Letters 581 (2007) 2721–2726

[20] María M. Penas, Brian Rust, Luis M. Larraya, Lucía Ramírez, and Antonio G. Pisabarro, APPL. ENVIRON. MICROBIOL. VOL. 68, 2002, 3891–3898

[21] M. Sunde**,** Ann H.Y. Kwan, Matthew D. Templeton, Ross E. Beever and Joel P. Mackay**. /**Micron 39 (2008) 773–784

[22] Mackay, J. P., Matthews, J. M., Winefield, R. D., Mackay, L. G., Haverkamp, R. G., and Templeton, M. D. (2001) *Structure* **9,** 83–91

[23] Zangi, R., De Vocht, M. L., Robillard, G. T., and Mark, A. E. (2002) *Biophys. J.* **83,** 112–124

[24] de Vocht, M. L., Reviakine, I., Wosten, H. A., Brisson, A., Wessels, J. G., and Robillard, G. T. (2000) *J. Biol. Chem.* **275,** 28428–28432

[25] de Vocht, M. L., Reviakine, I., Ulrich, W. P., Bergsma-Schutter, W., Wosten, H. A., Vogel, H., Brisson, A., Wessels, J. G., and Robillard, G. T. (2002) *Protein Sci.* **11,** 1199–1205

[26] R. Wang, Y.Yang, M. Qin, L. Wang, L. Yu,B. Shao, M. Qiao,C.Wang, X. Feng, Chem. Mater. 2007, 19, 3227.

[27] Wösten, H.A.B., Ruardy, T.G., van der Mei, H.C., Busscher, H.J., and Wessels, J.G.H. (1995). Coll. Surf. *B*. Bioint. *5*, 189–195.

[28] Lugones LG, Bosscher JS, Scholtmeijer K, de Vries OMH, Wessels JGH. An abundant hydrophobin (ABH1) forms hydrophobic rodlet layers in Agaricus bisporus fruiting bodies. Microbiology **142** (1996), 1321-1329

[29] Luca De Stefano, Ilaria Rea, Paola Giardina, Annunziata Armenante, and Ivo Rendina, Adv. Mater. 2008, 20, 1529–1533

[30] Wessels, J.G.H. (1997) Adv. Microb. Physiol. *38*, 1–45

[31] Wessels, J. G. H. *Annu. Re*V. *Phytopathol.* **1994**, *32*, 413-437

[32] Askolin S. Characterization of the *Trichoderma reesei* hydrophobins HFBI and HFBII, Ph.D thesis *Helsinki University of Technology (Espoo, Finland)*

[33] Yu, L.; Zhang, B.; Szilvay, G. R.; Sun, R.; Jänis, J.; Wang, Z.; Feng, S.; Xu, H.; Linder, M. B.; Qiao, M. *Microbiology* **2008**, *154*, 1677 1685.

[34] Martin, G. G.; Cannon, G. C.; McCormick, C. L. Sc3p Hydrophobin Organization in Aqueous Media and Assembly onto Surfaces As Mediated by the Associated Polysaccharide Schizophyllan *Biomacromolecules* 2000, *1*, 49-60.

[35] Paananen, A.; Vuorimaa, E.; Torkkeli, M.; Penttilä, M.; Kauranen, M.; Ikkala, O.; Lemmetyinen, H.; Serimaa, R.; Linder, M. B., *Biochemistry*, **42**, 5253–5258., (2003).

[36] de Vocht, M.L., Scholtmeijer, K., van der Vegte, E.W., de Vries, O.M.H., Sonveaux, N., Wosten, H.A.B., Ruysschaert, J.M., Hadziioannou, G., Wessels, J.G.H., Robillard, G.T., 1998. Structural characterization of the hydrophobin SC3, as a monomer and after self-assembly at hydrophobic/hydrophilic interfaces. Biophys. J. 74, 2059–2068.

[37] Wösten, H.A.B., Asgeirsdottir, S.A., Krook, J.H., Drenth, J.H.H., Wessels, J.G.H., 1994. The fungal hydrophobin Sc3p self-assembles at the surface of aerial hyphae as a protein membrane constituting the hydrophobic rodlet layer. Eur. J. Cell Biol. 63, 122–129.

[38] The SC3 Hydrophobin Self-Assembles into a Membrane with Distinct Mass Transfer Properties, X. Wang, Fuxin Shi, H. A. B. Wosten,§ H. Hektor, B. Poolman, G. T. Robillard, Biophysical Journal, 88 (2005) 3434–3443.

2. Langmuir technique

2.1 Brief history of Langmuir films

Humanity was already familiar with molecular films on water in the ancient times. In fact, since ancient Greece, sailors stories recount that a film of oil spilled in surface water tends to calm the waves. Since then, numerous studies were conducted to understand the origin of this phenomenon. From the late 19th century, concept of monolayer appeared, but this is Irving Langmuir, Nobel Prize in 1932, who really began to focus on thermodynamic properties of floating monolayers on water. He was the first to introduce the concept of amphiphilic molecules that contain two distinct components, hydrophobic and hydrophilic part. These molecules allow to obtain two-dimensional systems. Named after Irwin Langmuir, Langmuir films are rapidly growing in importance in the scientific community. The name Blodgett was added several years later when Katherine Blodgett gave a detailed description of monolayer transfer on substrate. Langmuir films usually refer to floating monolayers, and Langmuir-Blodgett films refer to a monolayer deposited by vertical lifting method on solid substrate.

Thin films are the source of high expectations as being useful components in many practical and commercial applications such as sensors, detectors, displays and electronic circuit components [1]. They are of vital importance for the building of electric, optical, and biotechnological sensors. Constrained by the progress of technology but also by the miniaturization of electronic components, industrial organisms have developed techniques to build up structures by deposition atom by atom, using the epitaxy techniques [2]. But the cost of these methods is high and their use is complex. In this context, Langmuir

technique has received increasing attention since many years, and Langmuir films preparation has been extensively investigated.

2.2 Langmuir films

The Langmuir film is usually built of a single layer of amphiphilic molecules on the surface of liquid called subphase. The most commonly used subphase is water, due to its large surface tension (γ_0 = 73 mN/m, at normal conditions of temperature and pressure). However, other liquids, as mercury [3] and glycerol [4], were also used as subphases. The Langmuir trough consists mainly of three parts: a plane trough containing the aqueous solution, the electronic device used to adjust molecular surface density and movable barriers.

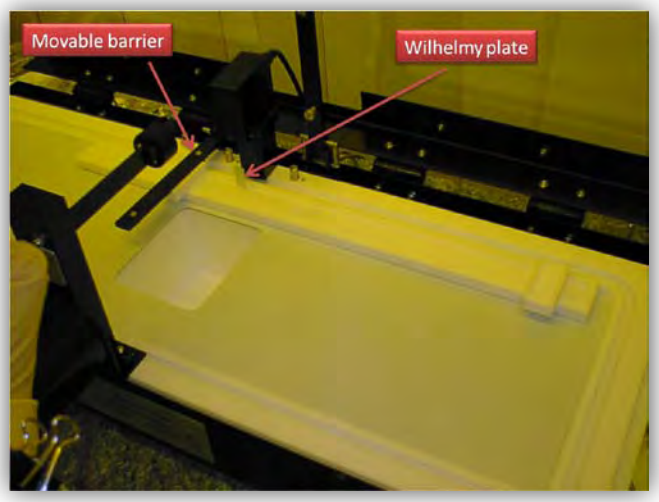

Figure 1: Photography of the used Langmuir trough at LiCryL laboratory.

The Langmuir trough is often made of Teflon in order to prevent any leakage of the subphase [5]. The amphiphilic molecules are dissolved in an organic solvent which is a good solvent for these molecules, and spread over the subphase. The solvent evaporates rapidly, and the molecules remain at the liquid–gas interface. The amphiphilic nature of the molecules dictates the orientation of the molecules at the liquid–gas interface in such a way that the hydrophilic part is immersed in the water, while the hydrophobic part of the

molecules remains in the gaseous side of the interface. When the available surface area is so high that the intermolecular distance is large, the mutual interactions of the molecules are small and the monolayer thus formed can be considered as the two-dimensional (2D) analogue of a gas (gaseous phase) (see figure 2a). The surface tension of the liquid surface is hardly affected by the presence of the monolayer, which will become different when movable barriers are used to reduce the surface area, the hydrophobic part of the molecules exerts a repulsive force and tends to "stand up," with the hydrophilic part still immersed in the liquid (see figure 2b). If we continue to exert a compression of the film, the hydrophobic part of the molecules tends to minimize the available volume, and becomes organized in a compressed monolayer solid-like (see figure 2c).

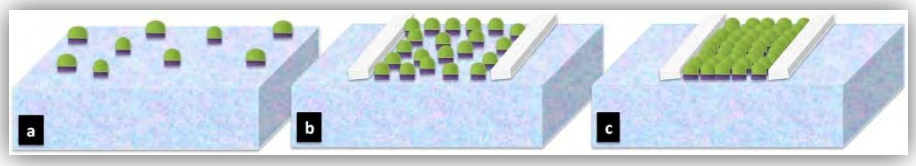

Figure 2. Monolayer of amphiphilic molecules molecules in a liquid–gas interface: (a) small concentration of molecules; (b) large concentration of moderately compressed molecules; (c) large concentration of compressed molecules.

2.2.1 Thermodynamic properties of Langmuir Film

A two-dimensional homogeneous system can be characterized by the following non-independent parameters:

Temperature: The film is in thermal equilibrium with the water that allows to maintain the temperature of the monolayer equal to that of water. In our experiment the temperature of the water was controlled at 18 °c using thermostated circulating water in channels placed underneath the Langmuir trough.

Area per molecule: The mean area per molecule noted *A* is the average area available for each amphiphilic molecule constituting the Langmuir film and

varies according to the movable barriers position in the Langmuir trough. It should be noted that the mean area has a minimum corresponding to the compact arrangement of molecules. Below this area, the Langmuir film begins to collapse and multilayers are created. The value of A, if compared to the known dimensions of the particular molecule, may be used to infer the orientation of the molecule, its behavior at the water surface and the interactions between neighboring molecules. It can be calculated as the ratio between the trough area S and the number n of molecules present at the interface as following: $A = S/n$. (1)

The calculation of area per molecule therefore requires knowledge of the number of molecules that have been spread from solution. This requires knowledge of several contributing values as solution concentration, solution quantity and molecular weight of monolayer material. The unity of area per molecule generally used is square nanometer or square angström per molecule. However, a difficulty for this calculation can occur if some spread molecules can plunge into the sub-phase or form tridimensional aggregates. As a consequence, the number of molecules at the interface and hence the area per molecule become unknown.

Surface tension: The molecules in a liquid have a certain degree of attraction to each other. The degree of this attraction, also called cohesion, is dependent on the properties of the molecule. The interactions of a molecule in the bulk of a liquid are balanced by an equally attractive force in all directions. The molecules on the surface of a liquid have fewer neighbors (see figure 3). This organization is not as favorable in terms of energy, because a molecule at the air/water interface has a larger attraction towards the liquid phase than towards the air or gas phase. Therefore, there will be a net attractive force towards the

bulk and the air/water interface will spontaneously minimize its area and contract.

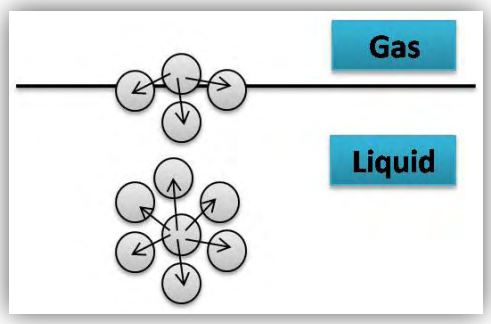

Figure 3. Schematic illustration of the interaction of molecules at an interface and in bulk

The net effect of this situation is the presence of free energy at the surface. The excess energy is called surface free energy and can be quantified as a measurement of energy per area. It is also possible to describe this situation as having a line tension or surface tension which is quantified as a force per length measurement. Surface tension can also be said to be a measurement of the cohesive energy present at an interface. The used unit for surface tension is mN/m, but it may also be expressed in dynes/cm. These units are equivalent. Polar liquids, such as water, have strong intermolecular interactions and thus high surface tensions. Any factor which decreases the strength of this interaction will lower surface tension. Thus an increase in the temperature of this system will lower surface tension. Any contamination, especially by surfactants, will lower surface tension. Therefore researchers should be very cautious about the issue of contamination.

2.2.2 Surface pressure

When the available surface area of the monolayer is reduced by a barrier system (see Figure 2) the molecules start to exert a repulsive effect on each other. For a

monolayer deposited on the surface of water, the differential of the free energy of surface can be expressed by:

$$dF_s = -S_s dT - \gamma d\Sigma + \sum_i \mu^i dn_s^{\ i}$$

Where S_s is the entropy, T is the absolute temperature, and γ is the surface tension in presence of monolayer, Σ is the area, n_s^i are the number of moles of different species present at the interface and μ^i are the corresponding chemical potentials.

Thus, the energy of the monolayer can be expressed as:

$$dF_s^{\ film} = dF_s - dF_s^{\ water}$$

with

$$dF_s^{\ water} = -S_s^{water} dT - \gamma_0 d\Sigma$$

where γ_0 is the surface tension in absence of a monolayer .

then

$$dF_s^{\ film} = -\left(S_s^{water} - S_s\right)dT + \left(\gamma_0 - \gamma\right)d\Sigma + \sum_i \mu^i dn_s^i$$

The two-dimensional analogue of a pressure is called surface pressure, and is defined as

$$\Pi = \left(\frac{\partial F_s^{\ film}}{\partial \Sigma}\right)_{T,n_i} = \gamma_0 - \gamma$$

This relation implies that the surface pressure is nothing more than the reduction of the surface tension of the air-water interface by the presence of the

monolayer. The pressure Π is a measure of the repulsive force between amphiphilic molecules spread over the subphase.

2.2.3 Isotherm

The most important indicator of the monolayer properties of an amphiphilic material is given by the measure of the surface pressure Π. We plot Π as a function of the area per molecule in order to characterize the properties of the surface monolayer spread over a subphase. This plot is called surface pressure-area isotherm [2] or simply "isotherm". This is carried out at constant temperature. Usually an isotherm is recorded by compressing the film (reducing the area with the barriers) at a constant rate while continuously monitoring the surface pressure. As the surface area per molecule decreases with compression, the typical behavior of Π depends on the molecules and subphase. Although the isotherms depend on the nature of molecules, a generalized isotherm showing the different phases that can be encountered is schematized in figure 4. During the compression of the layer, four phases can be encountered [6, 7]:

Gaseous (G) where the molecules are not in close contact and thus do not display any significant mutual interaction. Liquid expanded (LE), in this phase the molecules are aligned almost parallel with all hydrophobic part standing up in a 2D solid-like structure. Liquid condensed (LC) where the molecules are organized in a close-packed monolayer. And finally, solid phase, where the molecules are organized perpendicularly to the surface of water as a compact monolayer. Upon further compression, the available surface area can no longer contain the close packed monolayer, which will inevitably lead to the collapse of this monolayer and the formation of bi- and multilayers. It should be noted

the presence of plateau between different phases indicating a first-order transition.

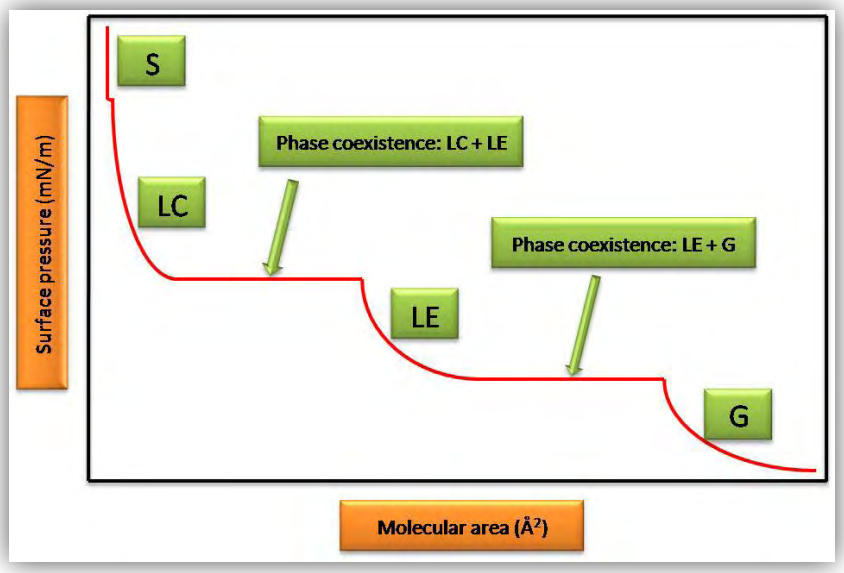

Figure 4. Generalized surface pressure-area isotherm of a Langmuir monolayer. Horizontal sections of the isotherm are phase coexistence regions at first order transitions [7].

The unit of surface pressure is Millinewton per meter (mN / m) which means that we have a force per unit length by analogy with the force per unit area in 3D. It is measured by the Wilhelmy plate-method. In this method we determine the force due to surface tension on a plate suspended and partially immersed in the subphase (see Figure 5). This force is converted into surface tension (usually mN/m) with the help of the dimensions of the plate.

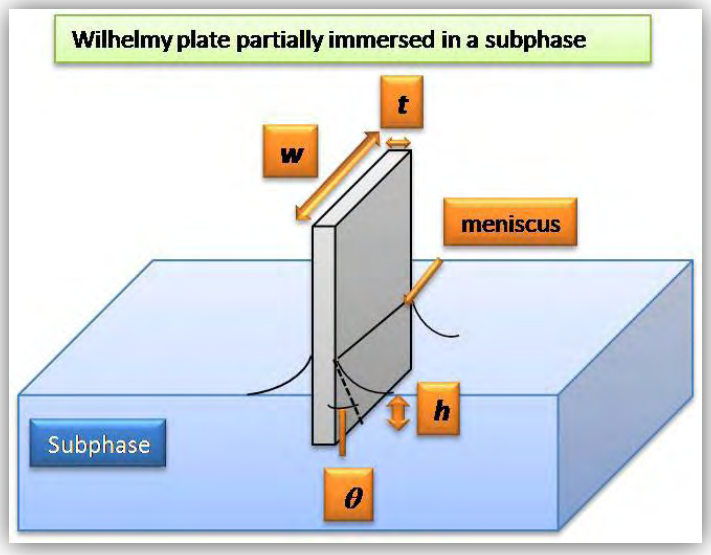

Figure 5. A Wilhelmy plate partially immersed in a water surface

The plate is often very thin and made of platinum, but even plates made of glass, quartz, mica and filter paper can be used. In all our Langmuir trough experiments, we have used filter paper that absorbs the liquid. The forces acting on the plate consist of the gravity and surface tension downward, and Archimedes thrust. For a rectangular plate of width w and thickness t, of material of masse m, immersed within a depth h in a liquid of density ρ the net downward force is given by the following equation:

$$F = mg + 2\gamma(t + w)\cos\theta - \rho t\omega hg$$

Where γ is surface tension in presence of monolayer, θ is the contact angle of the liquid on the solid plate (θ = 0 in our case) and g is the gravitational constant. As the value of the water surface tension is ca. 73 mN/m, at the temperature 18 °C . The surface pressure can be determined by measuring the force F at the depth (h = 0) in this case, the Archimedes thrust is negligible, on the other hand, measuring the force F when the plate is not in contact with the surface of water, leads to the determination of the plate weight. We thus obtain the γ value and consequently the surface pressure.

2.3 Film transfer on solid substrate

Monolayer films do not only exist in the form of a Langmuir film on the water surface. They can also be transferred on to solid substrates. This allows to form thin films, using one or several monolayer. The techniques employed in our experiments to fabricate solid film samples are Langmuir-Blodgett (LB) and Langmuir-Schaefer (LS) techniques.

2.3.1 Langmuir-Blodgett deposition

As demonstrated by Blodgett, stable Langmuir monolayers can be transferred from the air-water interface onto solid substrates. However, this transfer can be performed in several different ways, depending on the properties of the monolayer and of the substrate. For a relatively flexible monolayer, the Langmuir-Blodgett dipping method is often used. In our experiment, we have used in particular the technique where the substrate is dipped vertically through the monolayer at the air-water interface as shown in Figure 6; in this technique the hydrophilic substrate is required. In the figure 6, a deposition setup with the compression barrier and the displacement transducer is illustrated. The substrate is initially introduced vertically in the trough before film compression, then, the monolayer is compressed slowly (5 mm/mn) to a suitable surface pressure. This pressure is kept constant during the deposition, by a computer controlled feedback system between the electrobalance measuring the surface pressure and the barrier moving mechanism.

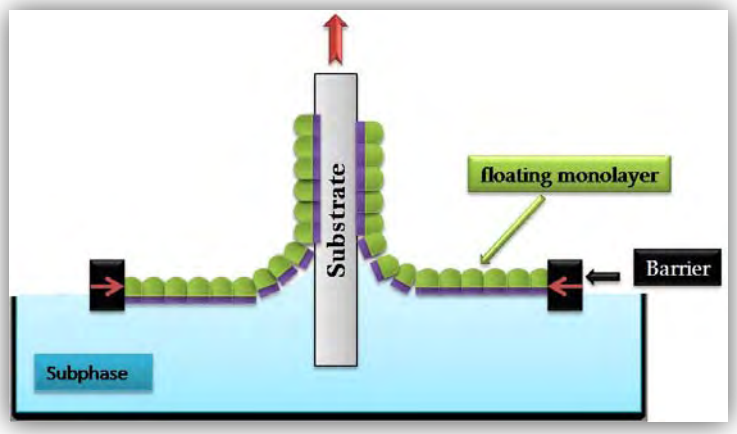

Figure 6. Schematic representation of Langmuir-Blodgett transfer

After stabilization of monolayer, the substrate is withdrawn from the liquid side of the interface towards the gaseous side. Consequently the floating monolayer is adsorbed to the solid substrate. In this case, the hydrophilic part of the molecule is placed in contact with the solid substrate.

2.3.2 Langmuir-Schaefer (LS) deposition

Another way for monolayer transfer on solid substrate was introduced by Langmuir and Schaefer [8]. In this LS dipping method, the substrate is aligned almost parallel to the air-water interface and is lowered until it just touches the monolayer. The monolayer will adhere to the substrate when it is withdrawn again, as shown in Figure 7.

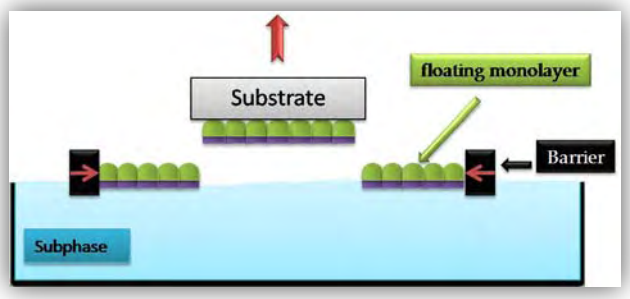

Figure 7. Schematic representation of Langmuir-Schaefer transfer

For this transfer method hydrophobic substrates must be used, as it is important that only the monolayer is lifted off from the interface and that as little water as possible adheres to the substrate. Upon drying, this water could cause redistribution of the material in the monolayer, in particular disordering structure.

2.4 Surface pressure feedback control

To ensure the transfer of Langmuir film on solid substrate at a constant surface pressure, the monolayer surface pressure is controlled via feedback loop as illustrated in the figure 8; in fact, a voltage derived from electro-balance is compared with a voltage corresponding to the desired surface pressure. The differential signal activates a motor which drives the compression barrier to either decrease or increase the monolayer area during the transfer.

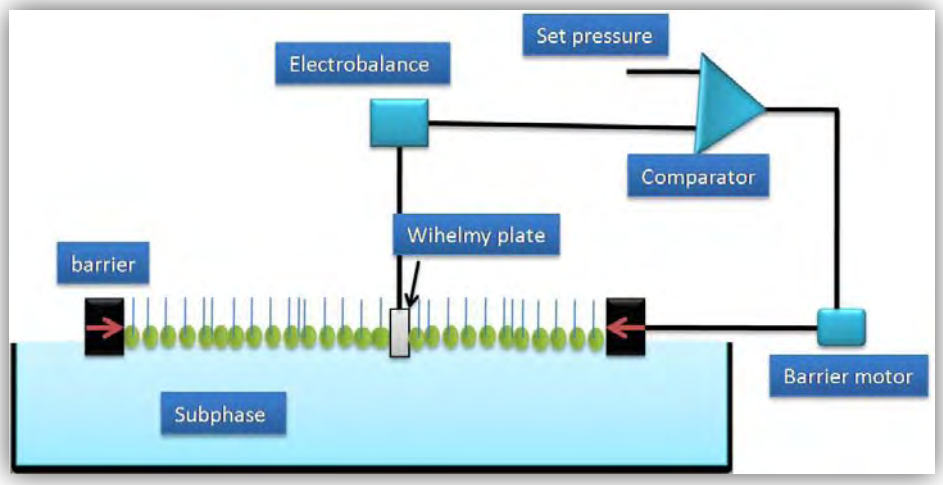

Figure 8. Feedback loop to control monolayer surface pressure and schematic illustration of a Langmuir film balance with a Wilhelmy plate electrobalance measuring the surface pressure, and barriers for reducing the available surface area.

2.5 Substrates Preparation

In my work, the study is focused in hydrophobin films deposited using Langmuir Blodgett technique and by Langmuir Schaefer one. In order to obtain hydrophilic surfaces suitable for Langmuir-Blodgett transfer, pieces of Si were washed in an ultrasound bath of chloroform for 3 minutes to eliminate carbon contamination. After drying, the Si pieces were immersed in a so called standard piranha solution containing sulfuric acid and hydrogen peroxide, 30% of H_2O_2 [30%] and 70% of H_2SO_4 [98%], and heated at 60 °C for 15 minutes. This step resulted in an oxidized SiO_2 surface thick enough to be considered as a silica surface in force measurements [9]. Pieces were hence washed with ultrapure water; and then dried with a nitrogen flow. The pieces were stored inside closed plastic boxes.

On the other hand, in order to obtain hydrophobic surfaces suitable for Langmuir-Schaeffer deposition, Si wafers were silanized using octadecyltriethoxysilane (OTE), with the help of Dr I. Bou Malham from INSP, Following the procedure described in ref. [10]

Self-assembled monolayers of n-octodecyltriethoxysilane (OTE 94%, from ABCR, Germany, used as received) were deposited on Si wafer following a protocol similar to that proposed initially by Kessel and Granick [11] and modified by Xiao et al. [12] OTE was prehydrolyzed by dissolving 0.4470 g of silane in 50 mL of tetrahydrofuran (THF puriss. from Riedel-de Haen, Germany) containing hydrochloric acid at a concentration of 0.1 M. The solution was stirred at room temperature for 3-5 days. 2.5 mL of the prehydrolysis solution was then diluted in 50 mL of cyclohexane (puriss. grade, Riedel-de Haen), while continuously stirring. After 30 min of agitation, the solution was filtered through a 0.2 μm PTFE membrane and brought to controlled temperature by immersion of the beaker in a dodecane bath

thermoregulated at (± 0.2 °C using a water-circulating system. OTE layers were deposited on plasma-treated Si surfaces at temperature 18 °C, the surfaces were immersed in the deposition solution during 20 s. The samples emerged almost completely dry from the silane solution, and residual droplets on the samples were immediately blown off in a stream of argon. Without further rinsing or post-treatment, Si silanized surfaces were then used for Langmuir Schaffer deposition.

Bibliography

[1] Roberts, G., Ed. *Lagmuir-Blodgett Films*, Plenum Press, New York (1990).

[2] S.M. Sze, Physics of semi-conducture devices, 2nd Ed. Wiley, New York, 1981.

[3] A. H. Ellison (1962). J. Phys. Chem. 66, 1867.

[4] A. Barraud, J. Leloup, and P. Lesieur (1985). Thin Solid Films 133, 113.

[5] Adamson A.W. (1976) *Physical Chemistry of Surfaces*. Wiley & Sons, New York.

[6] Adamson A.W, Gast A.P. *Physical Chemistry of Surfaces*, *Sixth Edition*, Wiley & Sons, New York.

[7] V.M. Kaganer, H. Mohwald, P. Dutta, Rev. Mod. Phys, 1999, Vol. 71 No. 3, 779-819.

[8] Langmuir, I., Schaefer, V.J. *J.Am.Chem.Soc.* **1938**, *60* ,1351

[9] A. B. Gurevich, M. K. Weldon, Y. J. Chabal, R. L. Opila, and J. Sapjeta. 1257, 1999, Appl. Phys. Lett. , Vol. 74.

[10] Ibrahim B. Malham, Lionel Bureau, *Langmuir* 2009, *25(10),* 5631–5636.

[11] Kessel, C. R.; Granick, S. Langmuir 1991, 7, 532.

[12] Xiao, X. D.; Liu, G. Y.; Charych, D. H.; Salmeron, M. Langmuir 1995, 11, 1600

3. Atomic force microscopy

3.1 Introduction

In 1986, Binnig et al. [1] revolutionized microscopy through the invention of the atomic force microscope (AFM). The AFM technique is a very high-resolution type of scanning probe microscopy. Since its invention, it has become important tool for nanometer-scale characterization of surface topography, but it is also a powerful tool for sensitive force measurements and thus for the study of different kinds of surface properties. After description of AFM apparatus, different modes in which an AFM can be operated will be detailed in this section.

3.2 Principles of AFM

The AFM technique is based a mechanical interaction between a tip and the surface of the sample. It consists of a microscale cantilever with a sharp tip at its end that is used to scan the sample surface. The cantilever is generally made of silicon or silicon nitride with a tip radius of curvature of the order of few nanometers. When the tip is brought into proximity of a sample surface, forces between the tip and the sample lead to a deflection of the cantilever. Forces that are measured in AFM include mechanical contact force, van der Waals forces, capillary forces, chemical bonding, electrostatic forces, etc. As well as force, additional quantities may simultaneously be measured through the use of specialized types of probe such as for example, the scanning thermal microscope that probes the local temperature and thermal conductivity of an interface.

In the AFM technique, the cantilever deflection is measured using a laser spot reflected from the top surface of the cantilever into an array of photodiodes (see figure 1). A feedback mechanism is used in order to adjust the tip-sample distance and to maintain a constant force between them. Generally, the sample is mounted on a piezoelectric tube, which can move the sample in the z direction for adjusting the force, and in the x and y directions for scanning the sample.

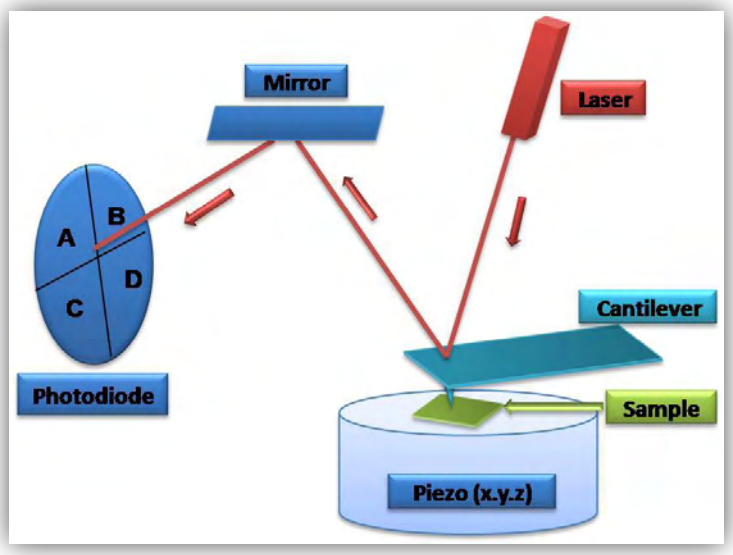

Figure 1. Schematic illustration of an AFM setup. The sample is maintained on a piezoelectric tube, which can be finely moved in x, y, and z. A laser beam is reflected from the backside of the cantilever into a photodiode to measure the deflection of the cantilever. In tapping mode, an additional piezo-electric is used to continuously excite the cantilever.

3.3 AFM probes

Cantilever and tip are among the most important features of the AFM. The cantilever shape is usually triangular (V shaped) or long and rectangular. In this work, I have used rectangular silicon cantilever in tapping mode measurements, and "V" shaped silicon nitride cantilever in contact mode measurements. Their mechanical and dynamical properties are represented by

Young modulus, resonance frequency, and quality factor. In the figures 2, 3 and 4 technical specifications taken from the manufacturer website are presented.

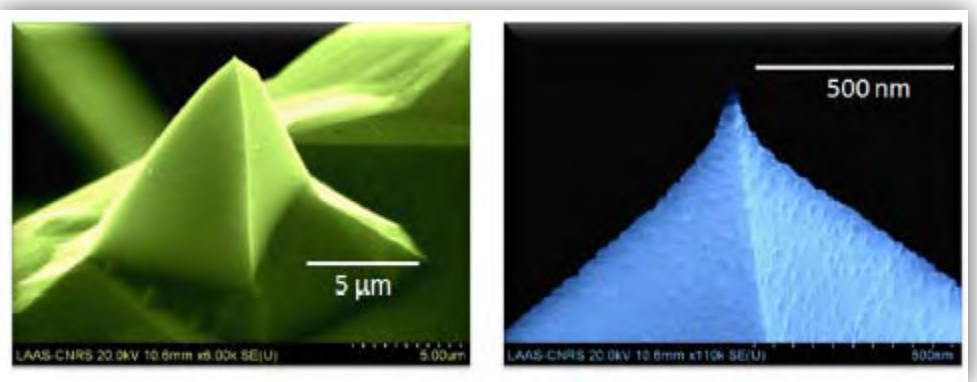

Figure 2. Scanning electron microscopy images of Si tip used in our work in tapping mode, from Nanosensors (nanosensors.com).

Shape	Length (L)(µm)			Width (w)(µm)			FREQ.(KHz)			k(N/m)		
	Nom.	Min.	Max.	Nom.	Min.	Max.	Nom.	Min.	Max.	Nom.	Min.	Max.
Rectangular	125	110	140	40	30	50	320	230	410	42	10	80

Tip Specification

Geometry:	Anisotropic
Tip Height (h):	10 - 15µm
Front Angle (FA):	25 ± 2.5°
Back Angle (BA):	15 ± 2.5°
Side Angle (SA):	22.5 ± 2.5°
Tip Radius (Nom):	8nm
Tip Radius (Max):	10nm
Tip SetBack (TSB)(Nom):	15µm
Tip Set Back (TSB)(RNG):	5 - 25µm

Figure 3. Technical characterization of the second tip used in our work in tapping mode, from veeco (veecoprobes.com)

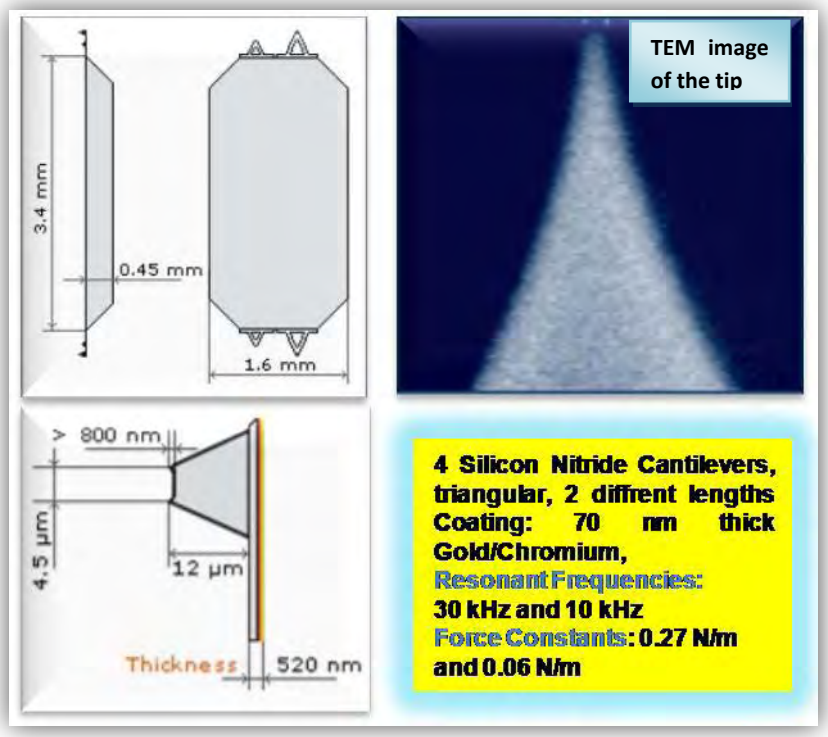

Figure 4. Si_3N_4 AFM probe model used in our work for contact mode measurements furnished by Budget sensors (budgetsensors.com).

3.4 Imaging modes

The AFM can be operated in a number of modes, depending on the application. In general, possible imaging modes are divided into static also called contact modes and a variety of dynamic modes where the cantilever is vibrated. In order to understand dynamic AFM mode, let us understand oscillators. I will therefore first do a little review.

3.4.1 Review of harmonic oscillators

In classical mechanics, a harmonic oscillator with a force constant k_c and an effective mass m is a system which, when displaced from its equilibrium position, experiences a restoring force, F, proportional to the displacement, z according to Hooke's law:

$$F(z) = -k_c z \qquad (1)$$

By Newton's Second Law, this is equal to

$$m\frac{dz^2(t)}{dt} = -k_c z \qquad (2)$$

There are two additional forces besides the tension in the spring which affect the motion of most oscillators one encounters, including the AFM cantilever. These forces are damping and driving.

Damping is frictional force, which tends to reduce the amplitude of oscillations in the oscillatory system; it is proportional to the velocity (i.e. it opposes to the motion). Thus,

$$F_{damping} = -\beta\frac{dz(t)}{dt} \qquad (3)$$

β is the damping coefficient defined as follows $\beta = \frac{m\omega_0}{Q}$, where ω_0 and Q are the resonance frequency and the quality factor of the oscillator. The last is a dimensionless parameter that describes how under-damped the oscillator. Higher Q indicates a lower rate of energy loss relative to the stored energy of the oscillator.

The expression for the driving force depends on how the oscillator is driven. Generally, a typical driving force is

$$F_{driving} = F_0\cos(\omega t) \qquad (4)$$

Thus the driving force has maximum amplitude F_0 and a frequency ω. Summing the forces, we get the equation for damped, driven oscillators.

$$\sum F = F_{spring} + F_{damping} + F_{driving} = -k_c z - b\frac{dz}{dt} + F_0\cos(\omega t)$$

We have then $$m\frac{d^2z}{dt^2}+\frac{m\omega_0}{Q}\frac{dz}{dt}+k_c z = F_0\cos(\omega t) \qquad (5)$$

3.4.2 Modeling the AFM cantilever

The AFM cantilever is a harmonic oscillator that interacts with the surface of sample. Its dynamical behavior can therefore be approximately described using the equation (5). In this case the tip-sample interaction f_{ts} must be taken into account and the differential equation of motion is:

$$m\frac{d^2z}{dt^2}+\frac{m\omega_0}{Q}\frac{dz}{dt}+k_c z = F_0\cos(\omega t)+ f_{ts}(z_0) \qquad (6)$$

where z_0 is the average tip-sample distance as indicated in the figure 5.

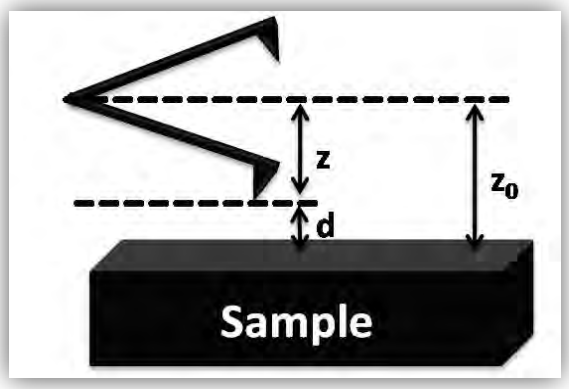

Figure 5. Scheme of the cantilever-tip and the sample. The instantaneous tip-surface separation *d*, the instantaneous position of the tip z are plotted.

The most simple case is when the interaction depends only on the tip-sample distance $z_0 - z$. The complexes behaviors take place, if the dissipative phenomena of adhesion, visco-elasticity or capillarity have to be taken into account.

Even in the simple case, $f_{ts}(z_0) = F(z_0 - z)$, the equation of motion of the system is generally non-linear:

$$m\frac{d^2z}{dt^2}+\frac{m\omega_0}{Q}\frac{dz}{dt}+k_c z = F_0\cos(\omega t)+F(z_0-z) \quad (7)$$

3.4.3 Non contact resonant mode

One can describe easily the operation of the linear mode AFM, which corresponds to a non dissipative and to an oscillator with low amplitude oscillation, far from the surface ($z << z_0$). A first order development of the tip-interaction force in the equation (7) leads to:

$$m\frac{d^2z}{dt^2}+\frac{m\omega_0}{Q}\frac{dz}{dt}+k_c z = F_0\cos(\omega t)+F(z_0)+F'(z_0)z \quad (8)$$

where $F'(z_0)$ is the gradient force at the central position of the cantilever (see figure 5). The constant term $F_0(z_0)$ leads to a shift of the rest position of the tip, which is generally negligible in comparison to the oscillation amplitude. One gets thus the equation relative to the new relative position:

$$m\frac{d^2z}{dt^2}+\frac{m\omega_0}{Q}\frac{dz}{dt}+[k_c-F'(z_0)]z = F_0\cos(\omega t) \quad (9)$$

The relation (9) corresponds to the equation of motion of a harmonic oscillator with the resonance frequency $\omega'^2_0=\omega_0^2\left(1-\frac{F'(z_0)}{k_c}\right)$

Therefore, the resonance frequency of the cantilever is shifted due to the gradient interaction. The gradient force can then be characterized by the resonance frequency.

3.4.4 Tapping mode

Tapping Mode AFM that is called also intermittent contact is the most commonly used of all AFM modes to probe the topography of soft sample by lightly tapping the surface with an oscillating probe tip. The cantilever is excited at or near its resonance frequency with amplitude ranging typically from 20 to 100 nm, and the cantilever's oscillation amplitude changes with sample surface topography, thus the topography image is obtained by monitoring these changes and closing the z feedback loop to minimize them. The Tapping mode can be characterized by some advantages in comparison with contact mode. First of all, in this mode the force exerted by the cantilever onto the surface is weak; this allows to work with softer materials. Moreover, the lateral forces that can damage soft samples and reduce image resolution are considerably weak in tapping mode.

In free air, i.e. far from the sample surface, a piezo stack excites the cantilever vertically at a constant frequency, causing the cantilever to move up and down. As the cantilever moves vertically, the reflected laser beam is deflected in a regular pattern over a photodetector, generating a sinusoidal, electronic signal. When the cantilever is at the sample surface, although the piezo stack continues to excite the cantilever with the same energy, the tip deflects in its encounter with the surface. The evolution of the reflected laser beam reveals information about the vertical height of the sample surface and characteristics of the sample material itself. These material characteristics include elasticity, magnetism, ect. The measured signal in volts is proportional to the root mean square of the oscillation amplitude. To obtain the cantilever's vibration amplitude in nanometers the conversion factor is obtained from amplitude versus distance plot as the one shown in Figure 6. It is assumed that, in the tapping mode case, changes in the cantilever base position are identical to changes in the oscillation

amplitude; therefore, the amplitude sensitivity is obtained from the slope of the amplitude versus the z piezo position when the tip is in contact with a hard sample.

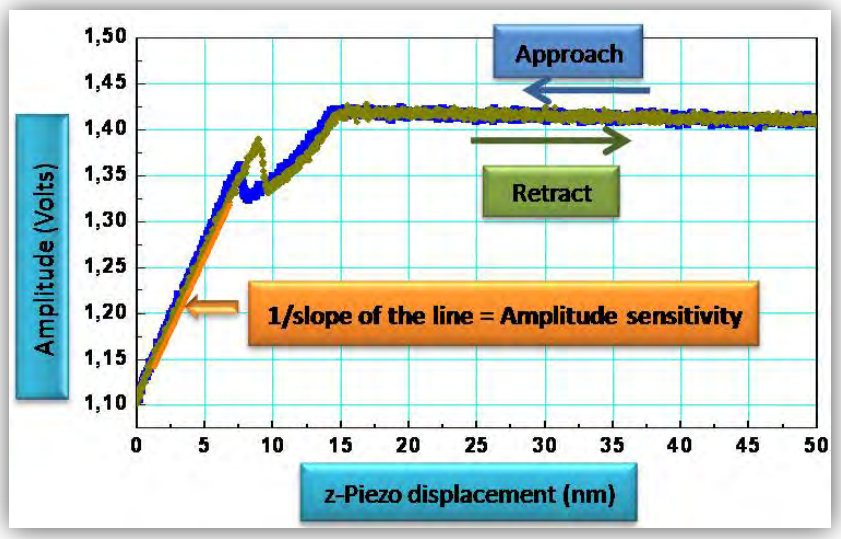

Figure 6. Experimental amplitude vs. z-Piezo displacement taken on SiO_2 wafer. The amplitude sensitivity is obtained from amplitude vs. distance curve. This consists in relating vertical displacement (in nm) of the piezo with the RMS amplitude in volts measured by the photodetector. This step is made in order to obtain amplitude in nanometers instead of volts.

The plot in figure 6 represents the amplitude for one complete extension-retraction cycle of the piezo. The vertical axis of the graphs represents the amplitude in volts, while the position of z-piezo plots along the horizontal axis. The cantilever amplitude decreases as the tip moves closer to the sample, and the slope in repulsive regime allows the conversion of amplitude in nm.

A thorough understanding of tapping mode AFM operation requires solving the equation of motion of the cantilever-tip ensemble under the influence of tip-surface forces.

In tapping mode AFM, the tip oscillates near to the surface and/or the oscillation amplitude is high. A first order development of the tip-interaction force in the equation of motion (6) is then usually not possible. The cantilever motion is described by:

$$m\frac{d^2z}{dt^2}+\frac{m\omega_0}{Q}\frac{dz}{dt}+k_c z = F_0\cos(\omega t)+ f_{ts}(z_0) \qquad (6)$$

Generally, a permanent solution is sought as follows: $z = A\cos(\omega t-\phi)$ where A is the oscillation amplitude and ϕ is the phase difference between the driving force and the cantilever response.

As we will see in the chapter 5, in general, f_{ts} is a nonlinear function of the tip–sample distance z, which contains both conservative and dissipative forces.

In tapping mode imaging an important step corresponds to a frequency sweep of the cantilever in order to determine its natural frequency. Qualitatively, the amplitude behavior as function of excitation frequency is shown in figure 7. The oscillation amplitude and the width of this curve depend on the quality factor Q. Increasing Q (i.e. smaller viscosity, operation in relative vacuum) results in higher oscillation amplitude and sharper resonance peak. Experimentally, the quality factor Q and the resonance frequency can be found from the *frequency spectrum* shown in Figure 7. Q is estimated as: $Q = \sqrt{3}\frac{\omega_0}{\Delta\omega}$, where $\Delta\omega$ is the width of the resonance curve when the amplitude is equal to $A(\omega_0)/2$.

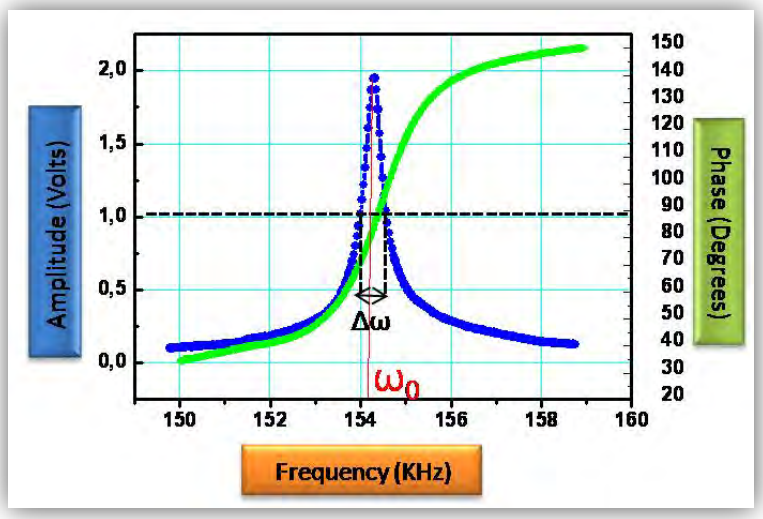

Figure 7. Experimental amplitude (in blue) and phase (in green) versus frequency response of the AFM cantilever. From these measurements, resonance frequency and quality factor of the cantilever-tip system are determined. The resonance frequency of the cantilever is ω_0 = 154.25 KHz. The corresponding phase curve showed a 90° phase shift at the resonance frequency, which is required for TM-AFM. The obtained quality factor is Q = 476. It has to be noted that the phase is presented here in real degrees (see paragraph phase imaging)

As illustrated in the Figure 7, the cantilever is excited with a piezoelectric ceramic. In one hand, at the resonance frequency ω_0, there is a large increase in the vibration amplitude of the cantilever. On the other hand, at ω_0 there is a 90 degree phase shift in the cantilever motion with respect to the forcing signal.

3.4.5 Topography imaging

When the probe tip interacts with a surface, the resonance frequency shifts to a lower value, and there is a corresponding change in the phase and amplitude. The average tip-sample distance being still larger than the *amplitude setpoint*, when tip and sample are brought close to each other interactions between both arises. Tip-sample interaction has as consequence, the diminution of oscillation amplitude. For topography imaging, the oscillation amplitude is consequently kept constant at the so called *amplitude setpoint* value. The value of the oscillation amplitude defines the magnitude of tip sample interaction and then controls the average tip-sample distance. If oscillation amplitude gets below the *set point* value, then the vertical position of cantilever base is incremented by the

feedback loop. In the opposite case the position is lowered. Measurements of the vertical position of cantilever at each x-y point lead to a construction of the sample topography.

Careful selection of the scan parameters is important. The optimal settings for the scan parameters depend on the sample and the information required. Main experimental parameters set in tapping mode AFM imaging are:

Drive frequency and *drive amplitude* which are the first parameters to be chosen. For imaging mode, *Drive frequency* is chosen to be slightly smaller than the resonance frequency.

Drive amplitude is the amplitude of the force at which the cantilever is driven. In the present work, these parameters are fixed from consideration of frequency spectra as in Figure 7 in order to fix the target amplitude as follows:

An important input parameter during a frequency spectrum is the *target amplitude*. For all experiments, the target amplitude was set to 2 volts which resulted in free oscillation amplitudes of about 50 nm.

The number of *pixels* used to create the images was 256×256. Indeed, the image quality is given by the number of lines and the number of pixel per line in the final image.

Image size, it defines the size of the scan by controlling the voltage applied to the X and Y piezos accordingly to the size of features that one is looking for. Generally, most images were in the range 400-3000 nm.

Amplitude setpoint, is the value of the RMS of the cantilever vibration amplitude that the feedback loop maintains constant for imaging

Scan speed, it controls the rate at which the cantilever scans across the sample area. In our experiment, it was in the range of 1-4 μm/s.

Integral and *proportional gains* that determine how is sensitive the feedback loop to variations in the tip's amplitude of oscillation; they were set to values

between 0.2-0.4 and 0.4-0.8, respectively. Typically, the settings for proportional gain were 35 – 100% larger than integral gain settings.

Tapping mode AFM measurements presented in this work were obtained using two apparatus furnished by Veeco Instruments: Nanoscope Dimension 3100 and Multimode, both with Extender Modules[1]. In this case, two piezos were needed to perform the experiments: one allowing the cantilever to be vibrated at its resonance frequency, as it was the case in approach-retract measurements, or at a frequency close to its resonance frequency for imaging mode, and a second piezo allowing to move the sample. However, in contact mode only the Nanoscope dimension 3100 which its laser detector has four quadrants was used. Microscopes were mounted on top of vibration isolating systems in order to diminish external noise and improve stability. Measurements were performed under ambient conditions but also in controlled humidity.

When the AFM measurement is performed at controlled humidity, the microscope is placed inside a glass box. A self made humidifier allowed the control of the relative humidity by varying the ratio of dry/wet nitrogen flowing into the glass chamber. Humidity was measured using a commercial hygrometer with a range of measurements between 0 to 100 %RH with a precision of ±0.5 %RH. To avoid local gradients of water vapor, the system was left to stabilize for a long time, at least half an hour.

3.4.6 Phase imaging

In addition to surface topography, tapping mode AFM provides a phase image [3], which is built from changes in the lag between the cantilever oscillation and the external excitation. It is a powerful signal for studying the properties of the sample surface [4]. Phase images often compliment topography images by

[1] Extender modules are electronic boxes that enable the microscope to acquire phase signals.

mapping the various regions of the sample surface each of which interact with the tip in a different way. This difference is sometimes not noticeable in the topography image, but clearly visible in the contrast variations in the phase image [5]. AFM images in the figure 8 present Topography and phase images respectively of a LB film of hydrophobin protein deposited on SiO_2 wafer. Thanks to the phase image we can distinguish between rodlets formed by the protein, while these rodlets are not clearly distinguished in the height image.

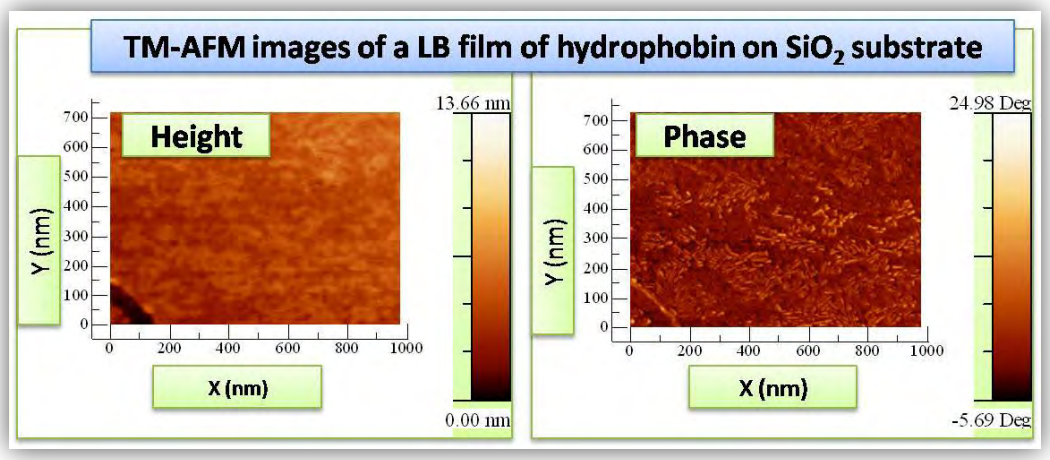

Figure 8. Example of the "complementarity" of information collected simultaneously in AFM height and phase mode on a LB film of hydrophobin protein deposited on SiO_2 wafer. Herein, the rodlets formed by the hydrophobin are clearly distinguished in phase image.

The Figure 9 shows the evolution of the phase shift versus excitation frequency on. At resonance, the phase shift is 90°, excitation frequencies well below ω_0 result in zero phase shift, while excitation frequencies well above resonance produce a phase shift equal to 180°. The phase shift is given as function of driving frequency as $\phi = \tan^{-1}\left(\frac{\omega_0 \omega / Q}{\omega_0^2 - \omega^2}\right)$.

When the tip interacts with the sample, an interesting interpretation is in terms of overall tip-sample interaction defining an attractive regime when $\phi > 90°$ or repulsive when $\phi < 90°$ [6, 7].

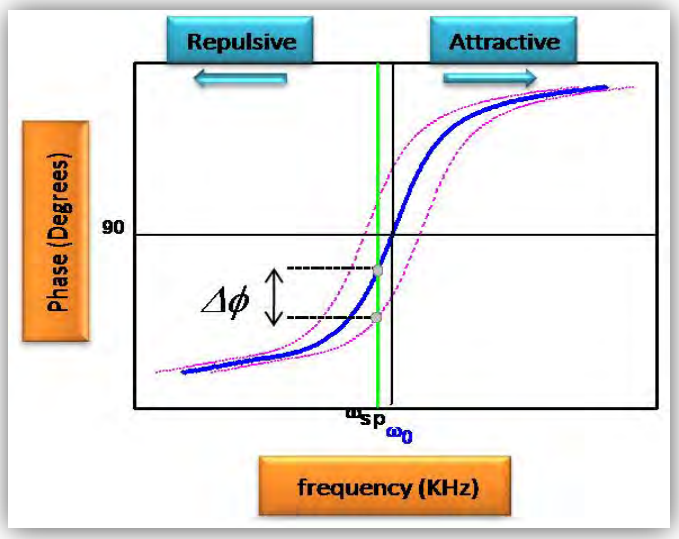

Figure 9. Phase shift frequency sweep curve upon engagement of the cantilever probe to a sample surface in different force regimes. Single harmonic oscillator (blue solid line) and under influence of attractive and repulsive forces (dashed lines).

When the cantilever operates under attractive forces, a shift of phase lag curve to lower frequencies occurs and the phase lag increases (see figure 9). As the cantilever experiences repulsive forces, the curve of phase lag as a function of excitation frequency shifts to higher frequencies and the phase lag at ω_{sp} changes. In both the repulsive and attractive regimes, the amplitude of cantilever is used as feedback parameter to restore the tip surface interaction.

The contrast in a phase image has been related to surface geometry [8], adhesion between the tip and the surface, variation in the elastic and viscoelastic properties of the surface [9, 10]. Changes in phase contrast were also attributed to the energy dissipated by the tip-sample forces [11, 12]. It should be noted that, in our AFM machines (from Veeco Instruments), the value of phase shift is not in degrees unit but in '*Bocek degrees*'. Consequently, for conversion to degrees unit, I have used the following formula $\phi = arccos(\phi_{veeco}/90)$. This relation is given by Adam Bocek (from dimensional instrument DI) [13]. However, Bocek conversion given by this formula is only approximate,

which means that, transformed phases would be good if their values are in the range 90±10 *Bocek degrees*.

3.5 Atomic force spectroscopy

In addition to study of surface topography by AFM, the specific properties as well as local mechanical and physico-chemical properties or chemical composition of samples can be investigated [14,15,16]. In this aims force spectroscopy has been implemented [17]. Indeed atomic force spectroscopy is an interesting technique to measure local interaction force between the AFM tip and the surface of sample on the nanometer scale. It is used in a variety of research fields including physics, chemistry, biology and engineering [18]. While AFM imaging is performed by scanning the sample in the *XY*-direction, force spectroscopy is performed by approaching and retracting the tip in the *Z*-direction.

3.5.1 Amplitude phase distance curves

In the intermittent contact case, one can observe tip–sample interactions by measuring changes in cantilever amplitude and phase versus the tip–sample distance, referred in this thesis as apd curves (amplitude phase distance curves).

Experimentally, to ensure better data reproducibility of apd curves, some detail must be taken into account. Indeed, when performing apd curve measurements, I start with AFM in its imaging mode, in performing the image on the point of interest where apd curve will be collected. Then by shifting to "force calibration mode" the horizontal scanning of the sample is stopped, and the cantilever base is lifted to the *starting position* where the approach/retract cycle starts. However, sometime it occurs that the start vertical position chosen

automatically by the microscope is too close to the sample. As a consequence, in the lowest point of approach the tip would already be hitting the surface which could induce irreversible modification of the tip geometry and damage the sample. Therefore, it is necessary to increment the start position by incrementing the *amplitude setpoint* of imaging just before shifting to force mode. In my work, all amplitude phase distance curve measurements were performed by exciting the cantilevers at the resonance frequency.

As a result of the applied voltage, the cantilever moves up and down relative to the stationary sample as shown in figure 10. The main parameters that must be controlled for apd curve measurements are: (i) Ramp size, this parameter defines the total travel of the z-Piezo. Increasing the value of this parameter increases the horizontal axis scale on the apd plot (figure 11). (ii) z-scan start, this parameter sets the offset of the piezo travel. Decreasing the value of this parameter shifts the apd curve on the display to the lift, while increasing the parameter shifts the curve to the right. This later must be done carefully to avoid damaging the tip, because increasing the value of z-scan start implies reducing tip-sample distance. (iii) Scan rate, this parameter defines the rate in which apd plots are collected. Generally, scan rate was set to 1 Hz for a ramp size ranging from 25 to 50 nm. The technical characteristics of an approach-retract measurement are given in both figures (10 and 11). In figure 10 the piezo travel in force calibration mode is shown, whereas a typical experimental apd curve is given in figure 11.

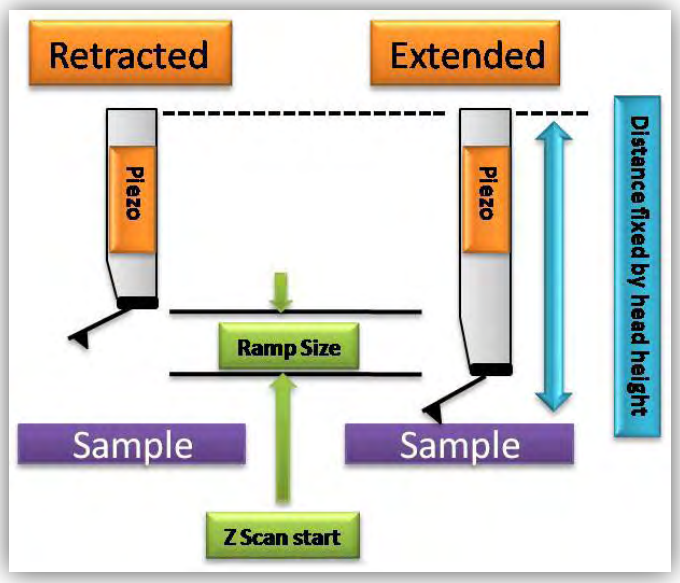

Figure 10. Piezo travel in force calibration mode. The z-stop is given by folowing relation : z-stop = z Scan start – Ramp size in retracting case and z-stop = z Scan start in extending case.

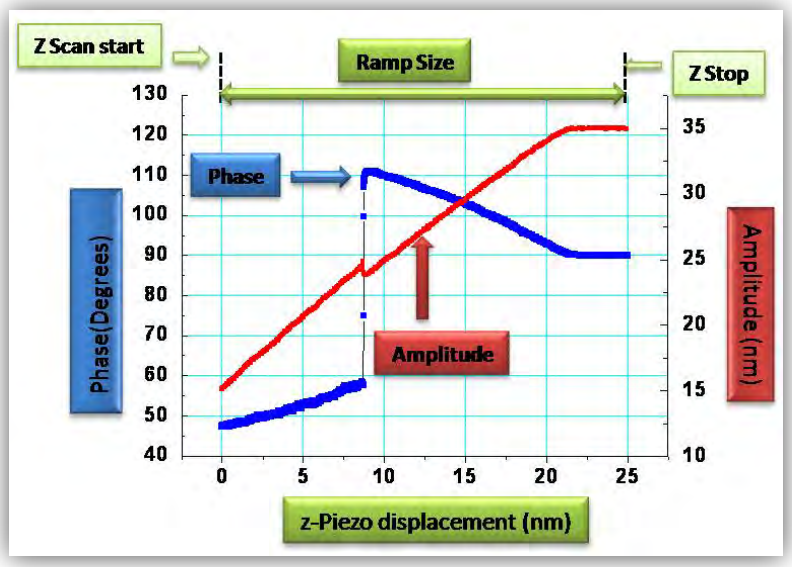

Figure 11. Typical amplitude (in red) and phase (in blue) curves as function of the tip-surface separation obtained in tapping mode AFM. Tecnichal characteristics of an apd curve given in figure 10 *(piezo travel)* are presented. For clarity the retracting parts of the apd curve are not presented here.

3.5.2 Amplitude dependence on tip-sample distance

Amplitude-distance curves are useful tool to optimize resolution and contrast in Taping mode AFM. Indeed, the oscillation amplitude is one of the most

important experimental parameters used in tapping mode AFM [18]. Figure 12 shows experimental amplitude versus distance curve obtained on SiO_2 surface where the oscillating behavior of the cantilever was measured while the tip is approached towards the sample surface using SiO_2 tip.

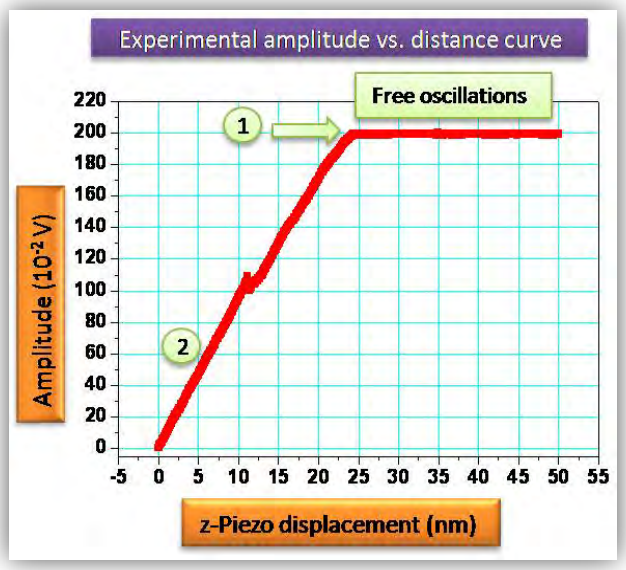

Figure 12. Experimental amplitude versus distance curve measured for SiO_2 tip against SiO_2 surface

In the figure 12, the horizontal line in the plot represents the amplitude of the oscillations far from the surface (free oscillation). At the point (1), the oscillating amplitude starts to decrease as tip-sample distance decreases before showing the presence of a transition point corresponding to the nonlinear dynamics of the tip-cantilever system in interaction with the surface. Then the amplitude decreases with the distance as soon as an intermittent contact happens (domain 2). As the piezo is extended further, the distance between the tip and the surface tends toward zero and oscillation eventually ceases and the amplitude tends toward zero. In fact, once the tip encounters the sample surface, the oscillation amplitude of the cantilever decreases as the piezo is extended. We can also note that the slopes of the lines before and after the transition point are not the same. An interesting interpretation of apd curves is term of attractive and repulsive

tip-sample interaction [17]. For large tip-sample distance (free oscillation) the effect of attractive forces on the oscillation is negligible, whereas at separations slightly larger than the free oscillation amplitude, the cantilever starts to sense the long-range attractive force. However, the amplitude curve by itself does not reveal if its reduction is due to attractive interactions, repulsive interactions, or a combination of both interactions [17]. A complementary tool for understanding the tip-sample interactions is the phase versus distance curve.

3.5.3 Phase distance curve

As I mentioned above, in dynamic AFM mode the oscillation amplitude and the phase shift may be recorded. This allows to perform simultaneous data acquisition. The dynamic mode may not only reduce the sample damage, but also offers the possibility to investigate the sample properties. Thus, in this aim, and in order to determine the operating regime, phase versus tip-sample separation measurements was recorded.

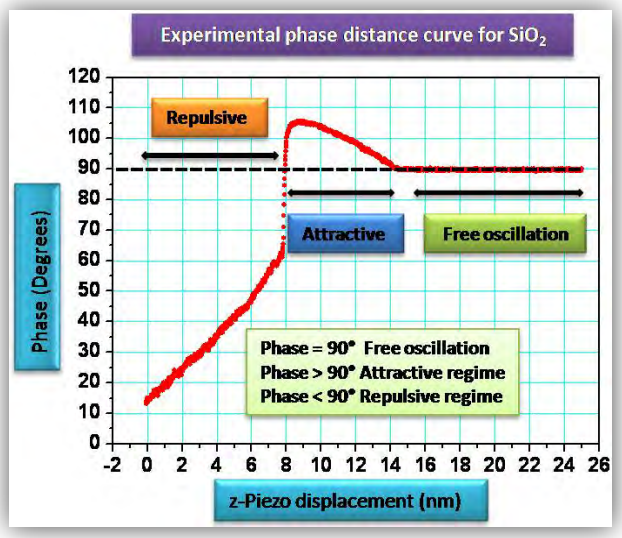

Figure 13. Experimental phase distance curve performed for SiO_2 tip against SiO_2 surface: Different tip-sample interaction regimes as defined by the behavior of the phase shift are presented.

In the figure 13, the phase versus tip-sample distance between a SiO_2 tip against a SiO_2 surface is plotted. The different tip-sample interaction regimes are

presented. Indeed, using the phase behavior, Garcia et al. [17] were able to define two elemental tip-sample interaction regimes present in tapping mode, attractive and repulsive. When the average separation between tip and sample is so large, the interaction between them is negligible; the phase lag value is 90º (this is true if the cantilever is excited at its resonance frequency). As the separation is decreased, the tip will experience attractive long range forces which is evidenced when phase take values above 90º. There is a transition position from a net attractive tip sample interaction to a net repulsive interaction which is marked by a jump in the phase curve from values above 90° to values below 90°.

In this work, we will show that the phase distance measurements are very useful to probe different properties of samples. My work is based on experience acquired in our group with phase distance curves on hard samples, trough the thesis of R.D. Rodriguez who was able to simulate experimental approach-retract curves in dynamic mode with van der Walls interactions and contact forces given by Dejarguin-Muller-Toporov contact mechanic (DMT). In my work, I will extend this experience mainly from the experimental point of view taking into account capillary forces as well as visco-elastic one.

3.6 Contact mode

In contact mode the probe is in continuous contact with the sample during scanning and the image is formed using the deflection of the cantilever. The forces in contact mode AFM are short-range repulsive forces, and the cantilevers used for this mode have force constants that are typically smaller than 1 N/m. Despite their small values, the forces are sufficient to generate tens of nanometers of cantilever deflection. The stresses applied to the sample

during imaging may induce deformation that alters the surface profile. Thus, this mode is a priori more appropriate for imaging hard samples.

The probe is sensitive to normal forces as well as lateral forces. A feedback loop maintains a constant deflection between the cantilever and the sample by vertically moving the scanner at each (x,y) data point to maintain this setpoint deflection. The deflection of the cantilever spring is directly proportional to the tip-sample interaction force. It is detected by the photodiode thorough the position of the laser, itself proportional to the cantilever deflection. However, there are two measurements required to convert the photodetector signal into quantitative value of force. The first stage consists in calibrating the distance that the cantilever actually deflects as a function of the change in photodetector voltage. This value depends on the type of cantilever but also on the optical path of the AFM detection laser. It will be slightly different each time the cantilever is mounted in the instrument. Once the deflection of the cantilever is known as a distance, z, the spring constant, k_c, is needed to convert this value into a force F, using the well-known Hooke's law: $F = k_c z$. In my work, for experiments performed in contact mode I have used the nominal spring constant furnished by the manufacturer, while the lateral force constant is determined according to the described method in the reference [19]. On the other hand, for cantilevers used in tapping mode, the Sader method [20] was used for spring constant determination. An interesting way to determine spring constants consists in attaching a known mass microparticle to the cantilever end to measure the deflection caused by the particle's weight [21]. k_c is determined by measuring the cantilever resonance frequency, ω, as a function of the added mass. The spring constant is then given by the slope of the line obtained from added mass versus ω^{-2} curve.

3.6.1 Calibration of the cantilever deflection

To obtain the cantilever's deflection in nanometers instead of volts, a force curve between a cantilever tip and a hard substrate is used to determine the cantilever sensitivity, which relates cantilever deflection to the voltage of the z-piezo. The sensitivity is given by the slope of the deflection-versus-z curve when the tip is in contact with the sample as shown if figure 14. This is a measurement of the deflection of the cantilever in nanometers for a given movement of the detection laser on the photodetector. A typical force calibration curve obtained for SiO_2 wafer and Silicon nitride cantilever in contact mode is given in Figure 14. The repulsive contact region, where the deflection rises steeply upwards, is linear for a hard surface and tip.

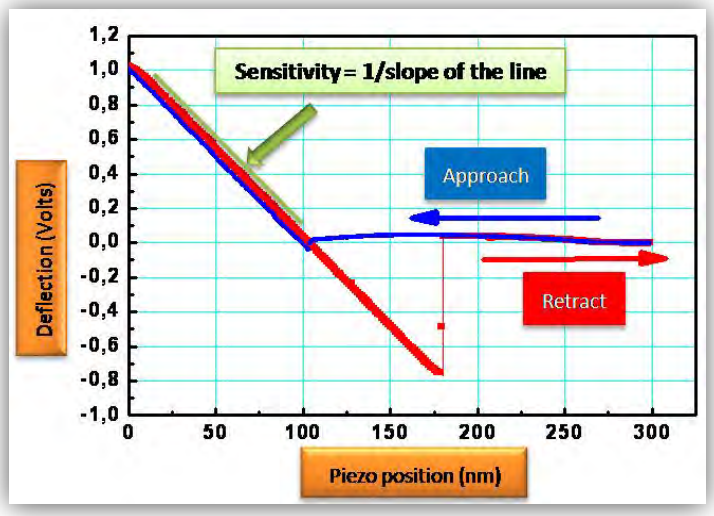

Figure 14. Force curve taken on SiO_2 wafer in contact mode. The deflection sensitivity is deduced from the slope of the line in repulsive contact region.

Multiplying the deflection of the cantilever in volts by the sensitivity obtained from the force curve on hard substrate, the cantilever deflection will be given in units of length, and then it is easy to convert to force in Newtons using linear Hook's law explained above. In all experiment performed in contact mode the

Si_3N_4 cantilevers having a nominal spring stiffness of ca. 0.06 N/m were used and this value was used to convert the cantilever deflection to the force unit.

3.6.2 Force curves measurements

In addition to the topographic measurements, the AFM can also provide much more information using the force curve measurements. This technique allows to measure the long range attractive or repulsive forces between the tip and the sample surface, elucidating local chemical and mechanical properties of samples like adhesion, elasticity and capillarity. Force curves typically show the deflection of the free end of the AFM cantilever while approaching and moving away from the surface. Experimentally, this is done by applying a voltage to the electrodes for the *z*-axis scanner. This causes the scanner to extend and then retract in the vertical direction, generating relative motion between the cantilever and sample. The deflection of the free end of the cantilever is measured and plotted at many points as the *z*-axis scanner extends the cantilever towards the surface and then retracts it again. The example in figure 15 shows a typical force versus distance performed for a Si_3N_4 tip and SiO_2 surface.

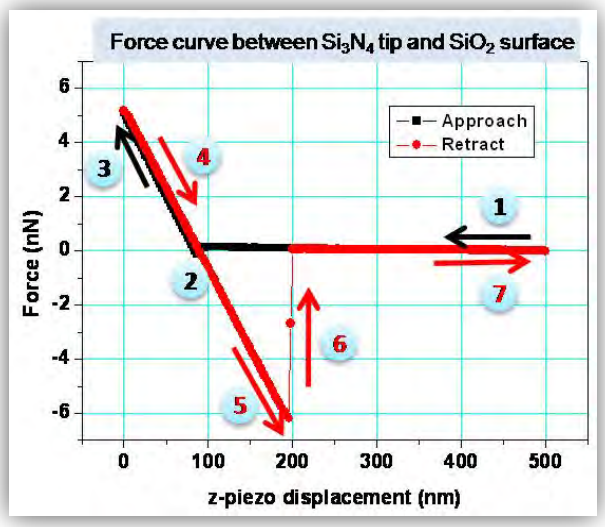

Figure 15. Experimental force curve measurements performed for a Si_3N_4 tip against a SiO_2 surface

Several points along a typical force curve are shown schematically in Figure 15. The cantilever starts (point 1) without touching the surface. In this region, if the cantilever feels a long-range attractive (or repulsive) force it will deflect downwards (or upwards) before making contact with the surface. In the case shown, there is minimal long-range force, so this part of the force curve shows no deflection. As the tip is brought very close to the surface, it jumps into contact (part 2) if it feels sufficient attractive force from the sample. Once the tip is in contact with the surface, cantilever deflection will increase (part 3). If the cantilever is sufficiently stiff, the tip may indent into the surface at this point. In this case, the shape of the contact part of the force curve (part 4) can provide information about the elasticity of the sample surface.

After loading the cantilever to a desired force value, the process is reversed. As the cantilever is withdrawn, adhesion or bonds formed during contact with the surface may cause the cantilever to adhere to the sample (part 5). A key measurement of the AFM force curve is the point 6 at which the adhesion is broken and the cantilever comes free from the surface. This can be used to measure the rupture force required to break the bond or adhesion. In the step (7), as the z-piezo continues retracting, the tip continues to move away from the surface. There is no further interaction with the sample surface during this cycle.

In my work, the force curve measurements were used in order to measure the adhesion force between AFM tip and hydrophobin films.

3.6.3 Friction

Friction force is the force opposing relative motion of two objects that are in contact with each other. At a nanoscale level, relative differences in surface frictional characteristics are identified and mapped by lateral force microscopy

(LFM) that is a scanning probe microscopy technique applied with contact AFM method.

In contact mode AFM, the sample can be scanned perpendicularly to the cantilever axis. In such case, the frictional force induces a twisting of the extremity of the cantilever, which induces a displacement of the laser spot in the horizontal plan (figure 16). The determination of this displacement is obtained by measuring the intensity difference between the right and left photo-detectors. This intensity difference is proportional to the twisting angle of the cantilever and hence to the magnitude of friction force.

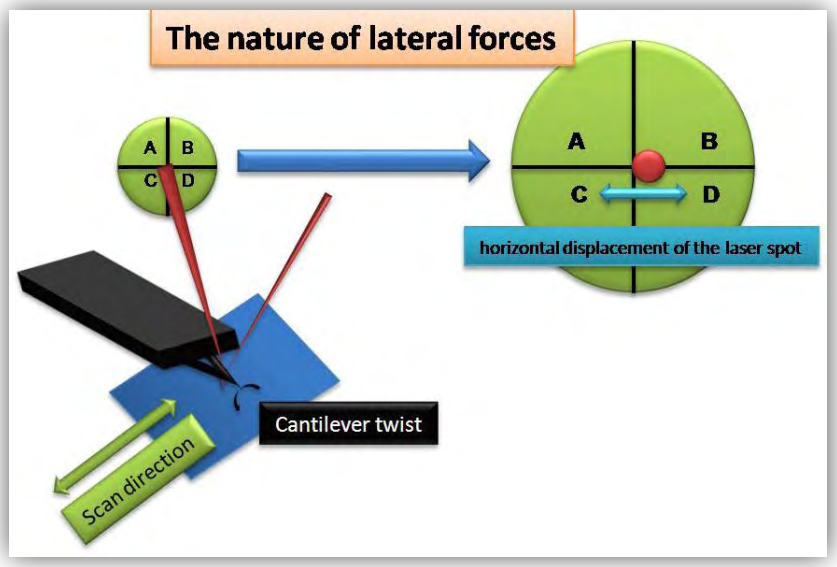

Figure 16. Scanning and detection with lateral force microscopy (LFM). To measure the frictional forces, the sample is scanned perpendicularly to the cantilever axis. The induced torsion corresponds to the horizontal displacement of the laser spot over the photo-diodes, it is given by following relation $(V_A+V_C) - (V_B+V_D)$.

Indeed, the degree of torsion of the cantilever supporting the tip is a relative measure of surface sample friction caused by the lateral force exerted on the scanning probe. The torsion, or twisting, of the cantilever will increase or decrease depending on the frictional characteristics of the surface (greater torsion results from increased friction). Since the laser detector has four quadrants (Figure 16), it can simultaneously measure and record topographic

data and lateral force data. Both of these data sets may be viewed simultaneously in real time, and stored and processed independently. The Figure 17 shows a typical friction loop obtained in contact mode AFM for a SiO_2 wafer.

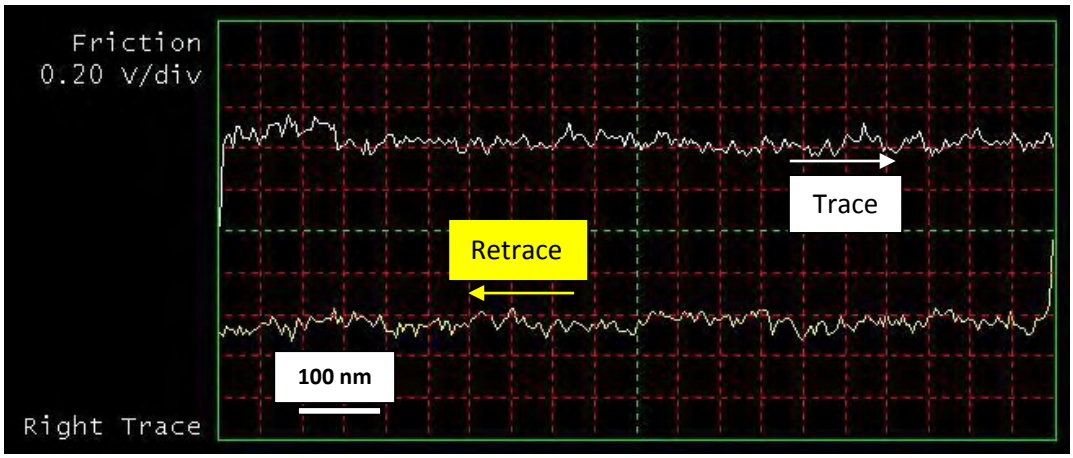

Figure 17. Typical friction trace and retrace, performed by AFM measurements for SiO_2 surface at the setpoint 3 v.

In the loop shown in the figure 17, left to right (forward) direction is defined as Trace (T) and the right to left (backward) direction as Retrace (R). The larger the separation between the friction trace and retrace (TMR), the larger the friction force. From Figure 17, it can be noticed that the sign of the friction signal is reversed for the Retrace scan compared to that of the Trace scan, which is due to the reversal of the torque applied to the end of the tip when the scanning direction is reversed. So, peaks in two-dimensional friction voltage signal correspond to high friction for Trace data and low friction for Retrace. Lighter regions in the Trace friction image correspond to higher values of friction force while in the Retrace image; lighter regions correspond to lower friction force.

The frictional force is an aggregate effect arising from various physical phenomena: elasticity, adhesion, viscosity, capillary forces, surface chemistry,

phononic and electrostatic interaction, etc. Any of them can dominate depending on conditions.

In this work, friction force studies were carried out on the hydrophobin films deposited on solid substrates by different ways. Hydrophobin Langmuir-Blodgett film and Langmuir-Schafer film were investigated as well as hydrophobin bi-layers. Si_3N_4 cantilevers having a nominal spring stiffness of ca. 0.06 N/m were used for friction force studies.

Friction force was measured under different loads using a 90° scan angle and 1 μm scan size, for all the experiments. A scan speed of 1 Hz was used. The applied load was calibrated according to the procedure explained in the paragraph 3.6.1 above.

The friction voltage signal (half of the difference between Trace and Retrace scans) was converted to units of force using the lateral spring constant of cantilever, determined taking into account the triangular geometry and the elastic properties of the cantilever [19]. The lateral sensitivity of the cantilever was determined from the curve of the friction loop [22, 23] recorded each time on SiO_2 surface on the small scan size (see figure 18).

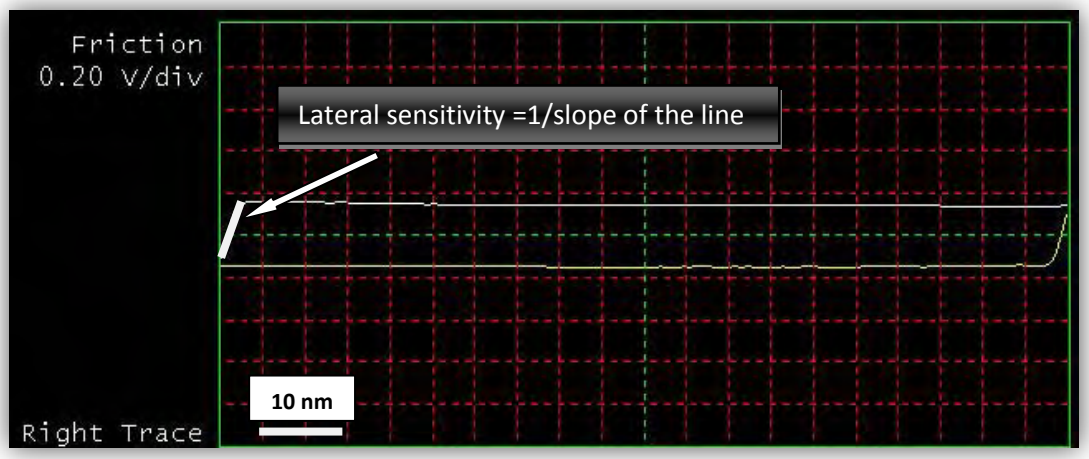

Figure 18 Trace Minus retrace measured for SiO_2 surface using a Si_3N_4 tip

The coefficient of friction of materials μ is defined by the Amonton's law [24], according to which μ is equal to the ratio of friction force applied to a probe, to

the normal force applied to a probe, shifted by adhesive force. Hence, slope of the plot between friction force and normal force provided the coefficient of friction.

Bibliography

[1] G. Binning, C. Gerber, C. Quate, Phys. Rev. lett. 1986, 56, 930.

[2] J. Tamayo and R. Garcia, Langmuir **12**, 4430, (1996)

[3] Garcia R., Magerle R., Perez R. Madrid : s.n., 2007, Nature Publishing Group, Vol. 6, pp. 405-411

[4] Jose R. Lozano and Ricardo Garcia, Phys. REV B 79, 014110 (2009).

[5] Garcia R., Tamayo J., San Paulo A. 1999, Surf. Interface Anal., Vol. 27, pp. 312-316.

[6] Garcia R., Paulo Alvaro San. 7, 1999, Physical Review B, Vol. 60.

[7] Chen X., Roberts C. J., Zhang J., Davies M. C., Tendler S. B. J. 2002, Surface Science Letters, Vol. 519, pp. 593–598.

[8] W. N. Sharpe, Springer Handbook of Experimental Solid Mechanics, Springer Science+Business Media, LLC New York 2008,

[9] J. Tamayo, R. Garcia, Appl. Phys. Lett. 71 (1997) 2394.

[10] J. P. Cleveland, B. Anczykowski, A.E. Schmid, V.B. Elings, Appl. Phys. Lett. 72 (1998) 2613-2615.

[11] Anczykowski B., Gotsmann B., Fuchs H., Cleveland J. P., Elings V. B. 1999, Applied Surface Science, Vol. 140, pp. 376-382.

[12] Tamayo J., Garcia R. 1998, Applied Physics Letters, Vol. 73, pp. 2926-2928.

[13] D. Bocek. 01-5, 2001, Microscopy Today

[14] S. Kopp-Marsaudon, P. Leclère, F. Dubourg, R. Lazzaroni, and J. P. Aimé, Langmuir **16**, 8432 (2000).

[15] G. Bar, Y. Thomann, R. Brandsch, H.-J. Cantow, and M.-H. Whangbo, Langmuir **13**, 3807 (1997).

[16] A. Knoll, R. Magerle, and G. Krausch, Macromolecules **34**, 4159 (2001).

[17] R. Garcia, R. Pérez, Surface Science Reports 47 (2002) 197-301.

[18]Atomic force microscopy and spectroscopy Yongho Seo andWonho. Jhe Rep. Prog. Phys. 71 (2008) 016101 (23pp).

[19] A. Noy, C. Daniel Frisbie L. F. Rozsnyai, M. S. Wrighton, C. M. Lieber, *J. Am. Chem. SOC. 1995,117,* 7943-7951

[20] J. E. Sader, J. W. M. Chon and P. Mulvaney, Rev. Sci. Instrum., 70, 3967 (1999)

[21] Cleveland, J. P.; Manne, *S.;* Bocek, D.; Hansma, P. K. *Rev. Sci. Instr.* 1993, *64, 403.*

[22] Yihan Liu, D. Fennell Evans, *Langmuir* 1996, *12,* 1235-1244

[23] les nouvelles microcopies à la découverte du nanomonde, L. Aigouy, Y. De Wilde, C. Frétigny, collection échelles, édition Belin 2006

[24] Amontons, G. De la Résidence Causée dans les Machines, **1699**, Mem. de l'Académie Royale A, 275-282.

4. Langmuir films of hydrophobin protein from *Pleurotus ostreatus*

4.1 Introduction

Recently, research on hydrophobins has focused on utilizing their physical properties for biotechnological applications. Efforts include modification of either hydrophobic surfaces such as porous silicon [1], or hydrophilic surfaces such as mica [2] using hydrophobin films. One of the best ways to prepare well defined films of controlled hydrophobicity for amphiphilic molecules is Langmuir method. As amphiphilic molecules, hydrophobins are applicable for Langmuir films. Previously, Langmuir-Blodgett and Langmuir Schaefer films of class I and class II hydrophobin proteins have been presented [3, 4, 5]. It was shown by AFM imaging in ambient conditions that the monomolecular films of both HFBI and HFBII class II hydrophobins obtained by LB transfer onto mica substrate present a highly ordered structure, but distinctly different [4]. The average thickness of the single-crystalline domains of HFBI was measured as 1.3 ± 0.2 nm, corresponding to a monolayer thickness. By contrast, the height of HFBII domains was not determined by AFM measurement, because of the presence of the amorphous regions between the single-crystalline domains. Kisko and co-workers [6] have investigated HFBI and HFBII proteins and were able to obtain highly ordered hydrophobin multilayers deposited onto SiO_2 surface using LB technique. They deposited sixteen layer LB films. Based on the molecular size; the thickness of the 16-layers film should be more than 20 nm. However, they measured the thickness of the deposited multilyers using x-ray reflectivity technique and found it to be 6.4 nm. They concluded that part of the protein material is missing and that some amount of water is also transferred.

Since class II hydrophobins are soluble in water, part of them might be washed away with the water when the substrate is lifted. A recent study [3] presented a self-assembled film of hydrophobin HFBI transferred to a graphite substrate using the Langmuir-Schaefer (LS) technique, and thereafter kept and imaged in water. The film was highly crystalline and had a thickness of 2.8 nm. This value is about 2 times higher than the obtained thickness in ambient conditions given in the reference [4] for LB monolayer. This highlights the importance of in situ studies.

To our knowledge, HFBI and HFBII are the only class II hydrophobins that are studied by the Langmuir technique to date. On the other hand, the class I that is investigated using this technique is HGFI protein from the edible mushroom G. frondosa [5]. In the reference [5], using Langmuir films, the authors were able to obtain AFM images of both the hydrophobic (LB) and hydrophilic (LS) sides of films formed at the air–water interface. No ordered structure was observed for HGFI class I hydrophobin. However, homogenous layer is observed by AFM in films compressed only once, whereas rodlet structures appear to be formed during compression of the film when several compression-expanssion cycles were performed.

In this chapter, we investigated vmh2 class I hydrophobin purified from the fungus *Pleurotus ostreatus* using the Langmuir technique both at the air-water interface as Langmuir films, and when deposited onto solid substrates as LB and LS films. Most of the results presented in this chapter were published in the reference [7]. The experimental isotherm curves obtained at the air-water interface were interpreted using the equation of state proposed by Volmer [8] and the deposited films were analyzed by Atomic Force Microscopy (AFM) in order to understand the assembly process of this protein. Indeed, hydrophobins could offer new options for surface modification and nanostructured functional

surfaces once the assembly processes and the structural hierarchy, as well as their effects on adhesion and surface activity, can be controlled at the molecular level. This brings the interest in hydrophobins into the field of nanostructured materials.

4.2 Experimental procedure

The hydrophobin protein was purified from the fungus *Pleurotus ostreatus* as described in the chapter 1.

The Langmuir films were prepared in a Nima Tech 632D1D2 LB system trough and home trough, using ultrapure water, at pH 5.5, and T = 18.0 ± 0.5 °C for the subphase. The required pH of the solutions was obtained by adding a suitable amount of HCl. The dried protein, as obtained from the purification procedure, was dissolved in 60 % ethanol in ultrapure water in order to get a protein concentration of 0.15 mg/mL. This solution is then spread on the subphase by the usual micro-syringe technique; small droplets were deposited at different places distributed over the whole trough area in order to get a uniform distribution at the interface. In order to monitor the interfacial film formation, the surface pressure was recorded at constant trough area as a function of time after 2000 μL of the protein solution was spread at the air-water interface on a 1200 cm^2 trough. Surface pressure was measured using a Wilhelmy plate attached to a sensitive balance with an accuracy of ± 0.5 mN/m. Compression of the monolayer was started after the surface pressure had stabilized, about 3 hours after spreading. The monolayer was compressed to the deposition pressure of 36 mN/m. The Langmuir films were then transferred at constant pressure onto SiO_2 substrates by the vertical lifting method at a rate of 10 mm/min to obtain Langmuir-Blodgett films, while silanized SiO_2 surface was used for Langmuir-Schaefer deposition. For the LB deposition we started by the

films deposition at 36 mN/m after only one compression, in the second time we have deposited the LB films after several compressions. In order to optimise the use of the available hydrophobin sample, we have modified our trough by considerably reducing its size (see figure 5) down to 102 cm^2. This allowed us to save material and then to use fresh solution for each experiment. In this case 250 μL of the protein solution was spread at the air-water interface.

The AFM measurements were carried out in the ambient conditions except for the results presented in the paragraph (2.4.24) where the measurements were performed in dry conditions. In this case, the microscope is placed inside a glass box and a continuous flow of dry-nitrogen is established until the relative humidity inside the box attained values smaller than 2%.

4.3 Theoretical basis

The experimental data were analyzed using the Volmer's equation [8], which describes the equation of state for amphiphilic monolayers [9-11]. In the cited references authors show that for monolayers in the Gaseous or Liquid Expanded phase, in the case $A > A_c$ (where A is the actual area per molecule and A_c is the area per molecule corresponding to the onset of the phase transition, i.e., when $\Pi = \Pi_c$), the equation of state is

$$\Pi = \frac{mkT}{A - \omega} - \Pi_{coh} \qquad \text{Equation 1}$$

where Π is the surface pressure, k is the Boltzmann constant, T is temperature, ω is the limiting area of a molecule in the gaseous state, A is the area per molecule, Π_{coh} is the cohesion pressure, accounting for the intermolecular interactions and m is the number of kinetically independent units, accounting for the aggregation. As reported in ref [12], Eq.1 can be used to analyze protein surface films.

4.4 Results and Discussion

4.4.1 Analysis of Langmuir film at the air-water interface

The surface pressure versus area isotherm is shown in Figure 1. The isotherm features a smooth rise of the surface pressure, and a collapse point close to 40 mN/m.

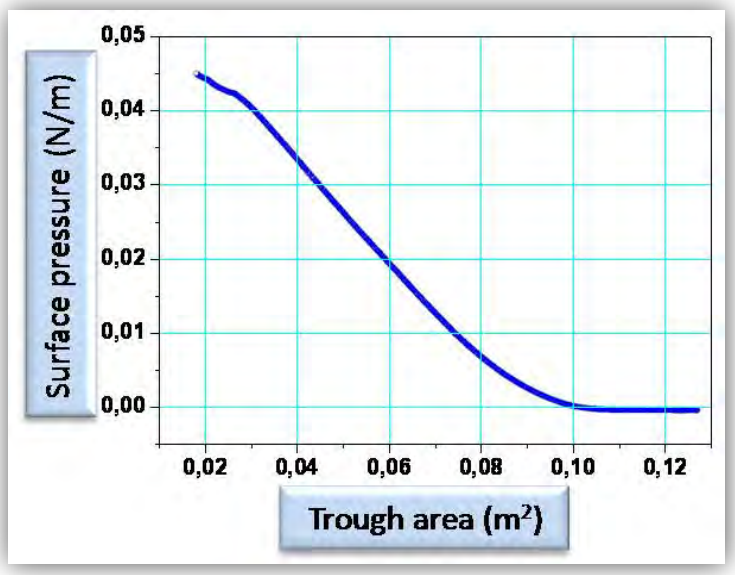

Figure 1. Surface pressure Vs. Area isotherm of class I hydrophobin at air/water interface @ pH 5.5. Note that the surface pressure is plotted as function of the trough area instead of the usual molecular area because of the film solubility in the subphase.

With reference to Figures 1, 3 and 5, we want to point out that the surface pressure is plotted as a function of the trough area instead of the usual molecular area. In fact we noticed that the film at the interface exhibits a molecular depletion in the subphase. This feature becomes evident in Figure 2 where the area as a function of time is plotted, in order to keep constant a given surface pressure value. A decrease about 19% in the area over a period of 20 min was observed.

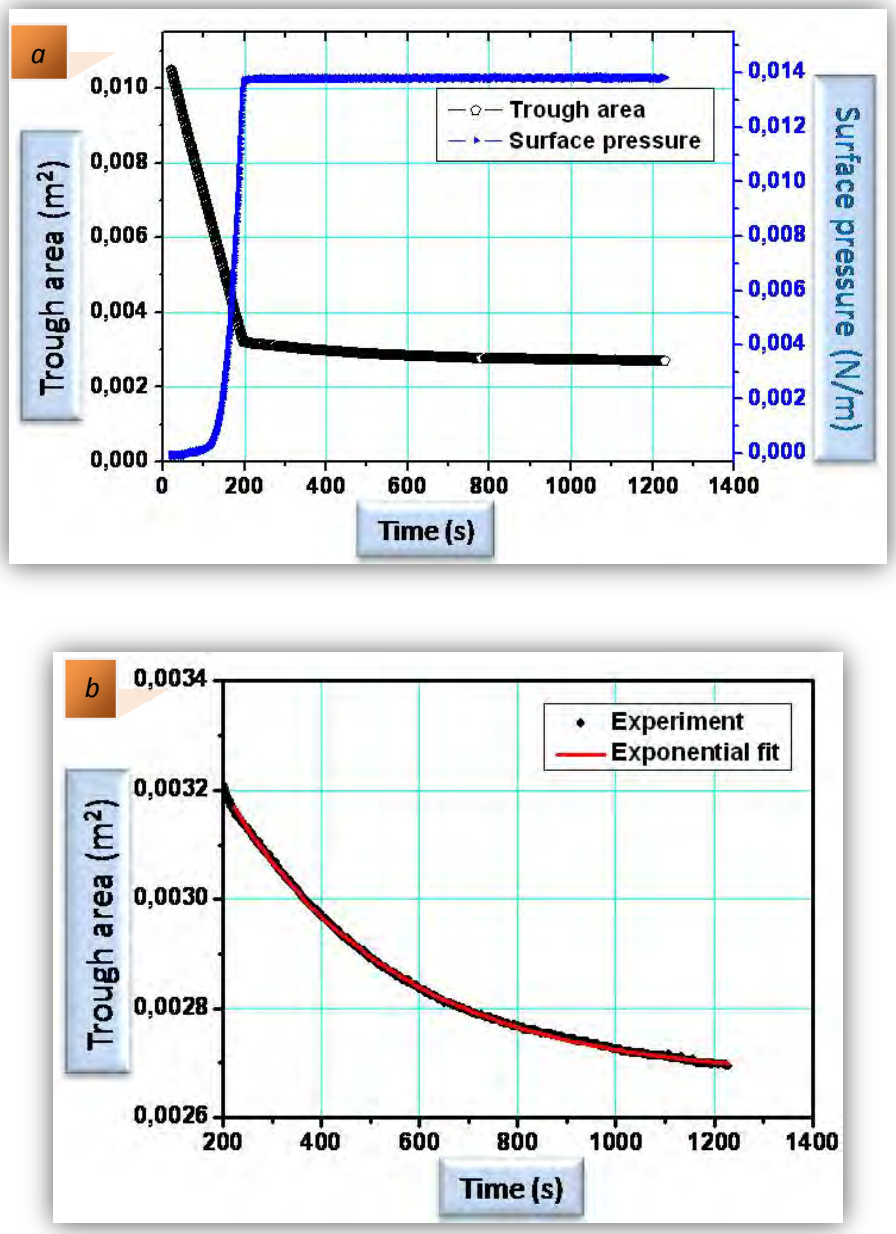

Figure 2. (*a*) Area Vs. Time curve to keep constant a given surface pressure value. In this case the surface pressure is set at 14 mN/m. This plot points out the molecular depletion. (*b*) By exponential fit of the onset of the trough area vs time curve where the pressure area is kept constant at 14 mN/m, we estimate the characteristic time of the process to be of the order of a few 10^2 s.

From this plot we estimate the surface molecular depletion characteristic time to be of the order of a few hundreds of seconds. We want to stress that in such cases, i.e. when the surface molecules number depletes, experiments should be performed in a time much shorter than the characteristic time of the depletion process, in order to be allowed to consider constant the number of molecules at

the interface during the whole experiment. Nevertheless this condition cannot be always fulfilled, as the compression speed cannot be made arbitrarily high because of possible instabilities in the Langmuir film structure. As a consequence, the actual number of molecules at the interface is generally unknown. In order to estimate the parameter *n*, i.e. the number of hydrophobin molecules present at the air-water interface, we compared the experimental isotherms to the equation of state expressed by Eq. 1. To do this we express the parameter *A*, i.e. the area per molecule, as the ratio between the trough area *S* and the number *n* of molecules present at the interface. Therefore Eq. 1 is modified as follows:

$$\Pi = \frac{mkT}{\frac{S}{n} - \omega} - \Pi_{coh} \qquad \text{Equation 2}$$

Equation 2 was then used to fit the experimental isotherm. Figure 3 shows the experimental (open circles) and the calculated (blue solid line) isotherms of the hydrophobin film. As one can see, this curve does not fit very well all the experimental points. We believe that the reason is associated with the surface molecular depletion, making the numbers of the molecules at the air-water interface not constant during the compression process. In order to validate this hypothesis, we performed a further fit over 10 subsets of the experimental points obtained by dividing the whole isotherm in 10 parts, providing that at least a few tens of points are considered for each data set.

This allowed us to virtually make faster the experiment by considering, for each fitting session, data collected in a fraction of the time needed for the whole isotherm acquisition. As result, we got a very good agreement between the experiment and the theoretical model. In doing this, we also noticed that the fit quality, expressed by the χ^2 value, although very good, reduces when the pressure increases. This may be due to the fact that the molecular depletion

becomes more important at higher surface pressure values. The resulting curves are joined in the red one reported in Figure 3. From both of the fitting methods, we obtained the same order of magnitude for the parameter n, in the order of 10^{14} molecules. From the same fit, we were also able to estimate the remaining parameter values in the model (eq. 2), summarized in the Table 1.

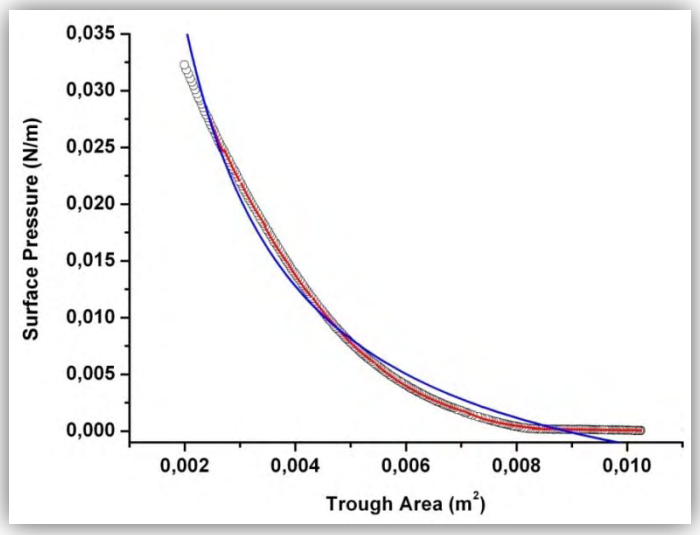

Figure 3. Experimental (open circles) and best fit from Volmer's equation (red and blue solid lines) isotherms for hydrophobins film. The blue solid line corresponds to the fit curve performed over all the experimental points. The red solid line corresponds to the fit performed on subsets of the experimental data (see the text for details). The values of the model parameters of equation 2 are listed in the table above.

Parameter	Whole Curve Fitting	Subsets Fitting (range)
m	60	**10 ÷ 40**
ω (nm^2)	10^{-2}	**1 ÷ 5**
Π_{coh} (N/m)	10^{-2}	**10^{-3} ÷ 10^{-2}**
n	1.5×10^{14}	**4×10^{14} ÷ 6×10^{14}**
χ^2	**1.1×10^{-6}**	**1.25×10^{-10} ÷ 4×10^{-8}**

Table 1. Parameter values of equation 2 as calculated from the best fit of the experimental isotherm for hydrophobin film at 18 °C. In the second column are listed the obtained fitting parameters related to the whole isotherm fitting, whereas in the third column is reported the range of the same parameters obtained by fitting the isotherm part by part.

We point out in particular that the obtained value for the parameter m is consistent with those reported in Ref [12]. Also the obtained values for the molecular area ω are in the correct order of magnitude for this kind of molecules, if we consider the second fit. Indeed, the diameter of the protein is approximately 2.5 - 3 nm, leading to a molecular area of the order of 7 nm^2 as explained in the first chapter.

By comparing this result to the number of molecules present in the hydrophobin solution as introduced into the Langmuir trough, 2.5×10^{15} molecules, we deduce that only about 1/10 of the total molecules contribute to the interfacial film formation. On one hand, one part of molecules went to the subphase when the hydrophobin molecules were introduced at the surface of water. Indeed, due to their nature, the hydrophobin molecules are not dissolved in volatile solution which allows to amphiphilic molecules to float at the interface, but they are dissolved in solvent mixture of 60 % ethanol in ultrapure water to avoid aggregates formation in solution. On the other hand, other molecules form aggregates at the interface or go to the subphase during film compression.

Using the obtained n values, we can now plot the experimental isotherm as a function of the area per molecule (Figure 4).

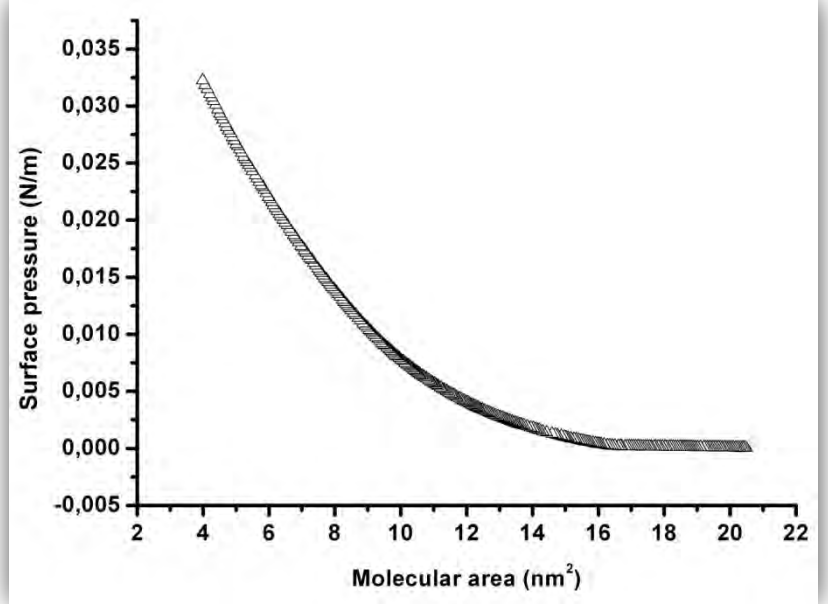

Figure 4. Experimental isotherm for the hydrophobin film as a function of the area per molecule, calculated as S/n, were S is the trough area and n = 5 10^{14} is the estimated number of hydrophobin molecules existing on the air-water interface as deduced from the experimental data fit.

The effect of the surface molecules depletion is also evident in the compression-expansion cycle shown in Figure 5. In fact, the expansion curve is shifted toward lower areas with respect to the compression curve. For HFBI and HFBII hydrophobins other authors attributed this shift to the formation of aggregates [4]. The formation of various aggregates by hydrophobins was noted very early. Takai described the formation of ''rods'' and ''fibrils'' by cerato-ulmin [13].

The observed molecular depletion in our system is certainly at least partly associated with the formation of aggregates during the film compression that do not disassemble during the expansion. This hypothesis is supported by the AFM analysis.

.

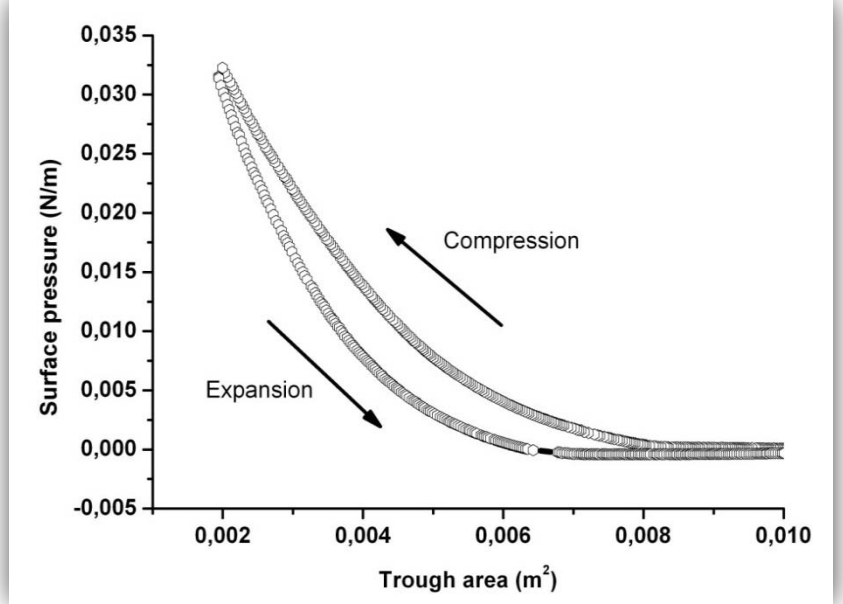

Figure 5. Experimental compression-expansion isotherm. The shift between the two branches is due to the molecular depletion occurring through the formation of hydrophilic rodlets.

4.4.2 Characterization of deposited hydrophobin films

Using Langmuir trough, we were able to obtain Langmuir films formed at the air–water interface. These films were then transferred onto solid substrates. For Langmuir films deposition, we have used two different methods: Langmuir-Blodgett (LB) technique that allows to obtain hydrophobin film with hydrophobic surface in contact with air. In this case SiO_2 surfaces have been used as substrates. On the other hand, Langmuir-Schaefer (LS) technique has been also used. This technique allowed us to obtain hydrophobin films with hydrophilic surface in contact with air. Silanized SiO_2 substrates were then used for film deposition.

Using atomic force microscopy (AFM), we have demonstrated that vmh2 hydrophobin protein formed homogenous films by both LB and LS techniques, with low roughness that is about 0.25 nm (see figures 6). The AFM images show that the the topography of both films is similar. This is normal, because the

films are the made from the same molecules and not modified by the interaction with substrate.

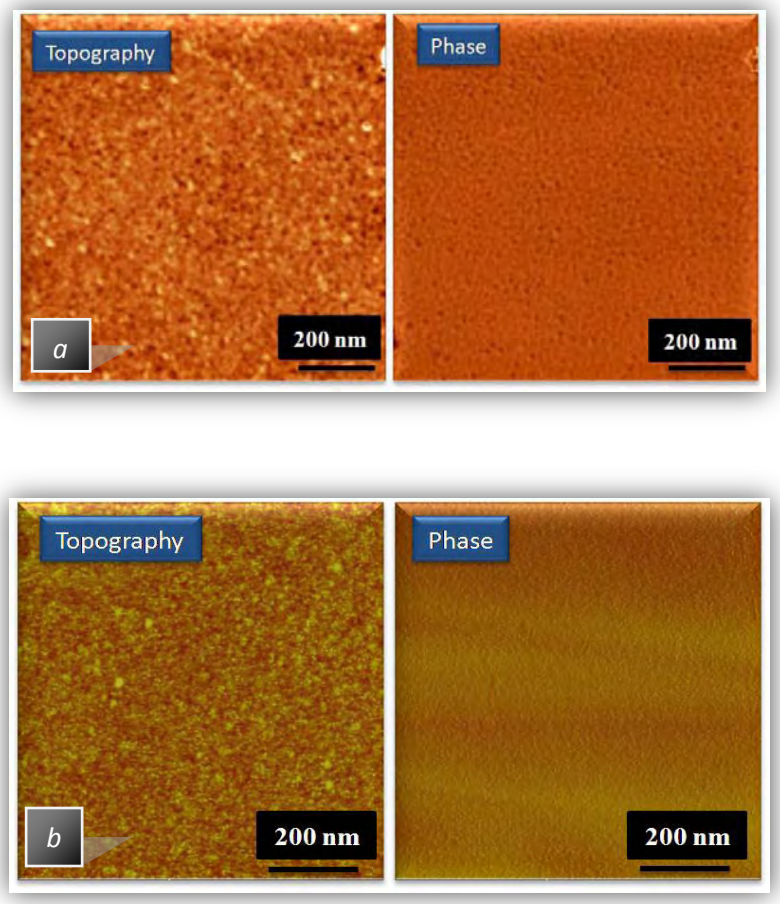

Figure 6. AFM topography and phase images of the obtained homogenous films: (*a*) LB film and (*b*) LS film, height scale 10 nm and 7 nm respectively.

On the other hand, the thickness of deposited films by both techniques was measured by AFM method thanks to some holes that exist into the films, as shown in the AFM images accompanied with cross section presented in the figure 7. The measured values were similar in both cases; they were about 2.5 ± 0.4 nm. It has to be noted that we had not access to films thickness using x-ray reflectivity technique because the thickness is too small to be detected by this method. Moreover, as it will be discussed later, when repeated compression-expansion cycles were performed, we have demonstrated that the aggregates

under form of rodlets which is characteristic of class I hydrophobins were formed. These rodlets are very difficult to dissolve and typically pure trifluoro acetic acid has been used for the purpose of dissolving these assemblies. This property makes them useful for application in nanotechnology [14]

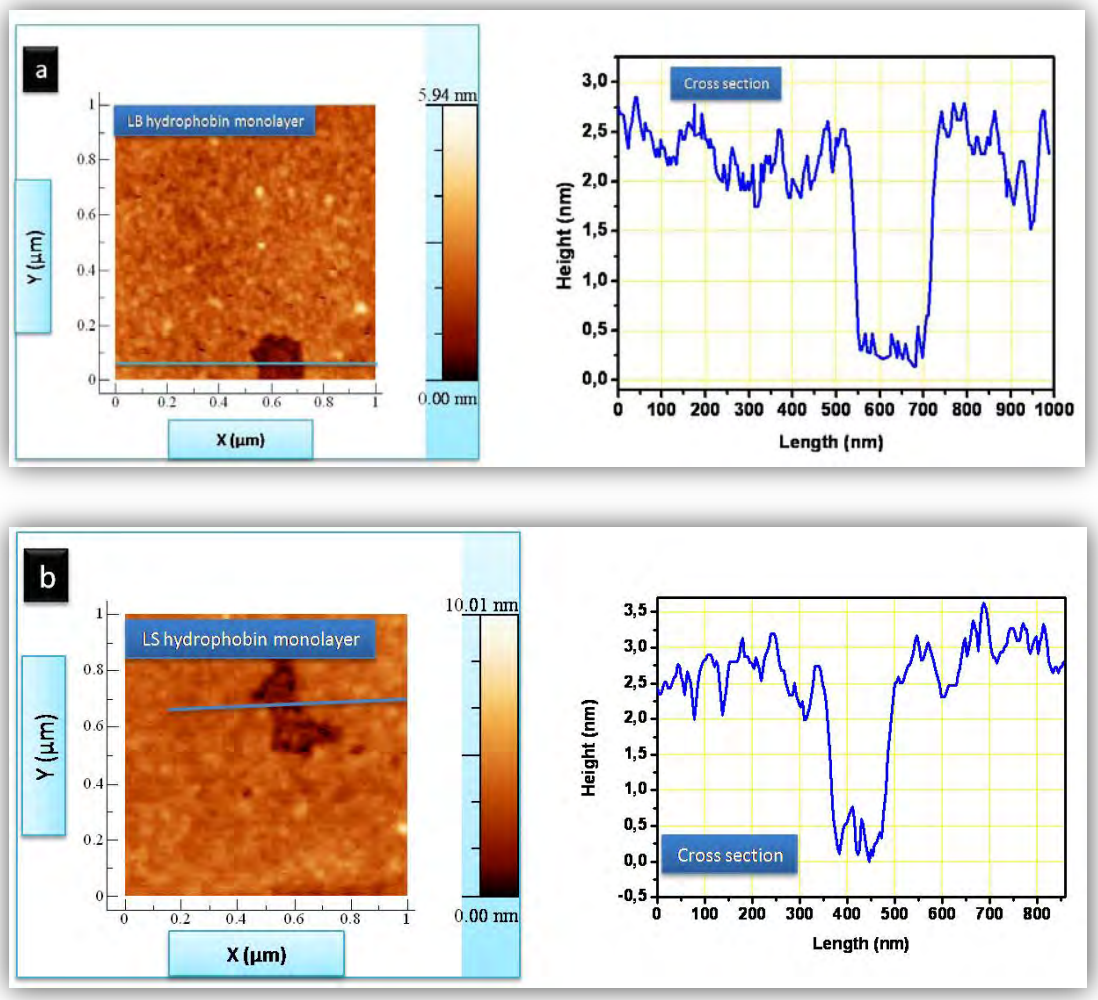

Figure 7. AFM topography image and cross profile of: hydrophobin LB monolayer (a), and LS monolayer (b), showing the accurate film thickness determination.

4.4.2.1 Modification of wetting properties of surfaces

We have investigated the wettability of the obtained hydrophobin films by performing contact angle measurements as illustrated in figure below, with the help of I. B. Malham (from INSP). We found that, the hydrophobin LB film exhibits a hydrophobic nature characterized by 81° contact angle. In contrast,

hydrophobin LS film displays a hydrophilic nature characterized by 43° contact angle (figure 8). This is consistent with the expected result. The surface of LB film should be hydrophobic, because, due to the LB method transfer on hydrophilic surface, hydrophobin molecules will adhere to the substrate by their hydrophilic parts, whereas the hydrophobic ones are exposed to the air. In contrast, the surface of LS film should be hydrophilic, since in the LS method transfer on hydrophobic surface, the hydrophobic side of monolayer will orient towards the solid surface, while the hydrophilic parts are exposed to the air. This is also consistent with results reported by other authors [15] which measured the contact angle on Teflon coated with a 10 nm thick by immersion in an aqueous solution of a class I hydrophobin, and found that the wettability of the hydrophilic side of assembled class I hydrophobins varies with a contact angle ranging from 36 to 63°. However the contact angle reported by Scholtmeijer et al [16] at hydrophobic side ranges from 115 to 121° for Sc3 hydrophobin. This variation in the wettability of hydrophobin coating is associated with the conformational change, as suggested by Janssen et al. [17] which have showed that, the transition from the α-helical form to the β-sheet state was accompanied by increased water contact angles. This may be also due to the deposition techniques, since the hydrophobins are often deposited on solid surfaces by immersion in aqueous solution or by incubation, resulting in uncontrolled thickness of the deposited films. In contrast, the LB and LS techniques allow to obtain the hydrophobin layer with well defined thickness.

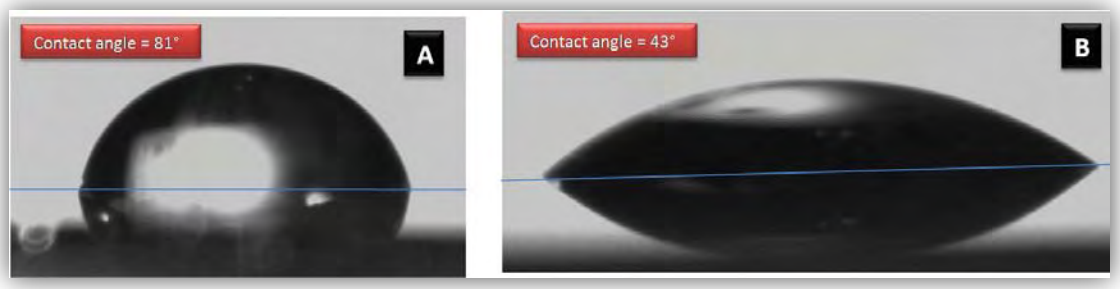

Figure 8. Water contact angle on LB hydrophobin films: (A) LB film deposited on hydrophilic SiO_2 surface and (B) on LS film deposited onto hydrophobic silinized SiO_2 substrate.

We have thus shown that with the hydrophobin protein, we can modify the wettability of a surface. Indeed, the hydrophobin LB monolayer turns the hydrophilic surface of SiO_2 into a hydrophobic one, while the hydrophobin LS monolayer turns the hydrophobic surface of silane into a hydrophilic one. This result is in agreement with results reported by other authors for other type of hydrophobins [18-21]. This is very interesting because the ability to switch between two different wettability regimes could be an important feature in designing bioactive interfaces for miniaturization not only of biosensors but also of medical devices [22]. The property of hydrophobins to self-assemble at hydrophilic-hydrophobic interfaces makes them interesting candidates for use in medical and technical applications [23]. On the other hand, the LB and LS techniques are particularly interesting methods to probe the different properties of the hydrophobic and hydrophilic parts of the same molecule, as it leads to films better controlled than ones obtained by incubation.

4.4.3 Characterization of Hydrophobin LB film transferred onto SiO_2 surface after repeated compression

We have seen in the precedent section that the LB and LS techniques allow to obtain homogenous monolayers when the films at the air-water interface are compressed once. In contrast when the films at the surface of water are compressed several times, AFM observations of LB hydrophobin film deposited onto hydrophilic SiO_2 substrates have revealed the formation of two kinds of assemblies: rodlets structure and homogeneous film (figure 9). This indicates that formation of rodlets occurs during compression of the film, which means that the compression triggers the aggregation process. Interestingly, this is a way to form different forms of assemblies from hydrophobin protein using the Langmuir trough. Recently L. Yu and co-worker [5] presented AFM images showing HGFI class I hydrophobin rodlets obtained by the Langmuir technique, but depending on the number of compression, only homogeneous film or only rodlets were observed.

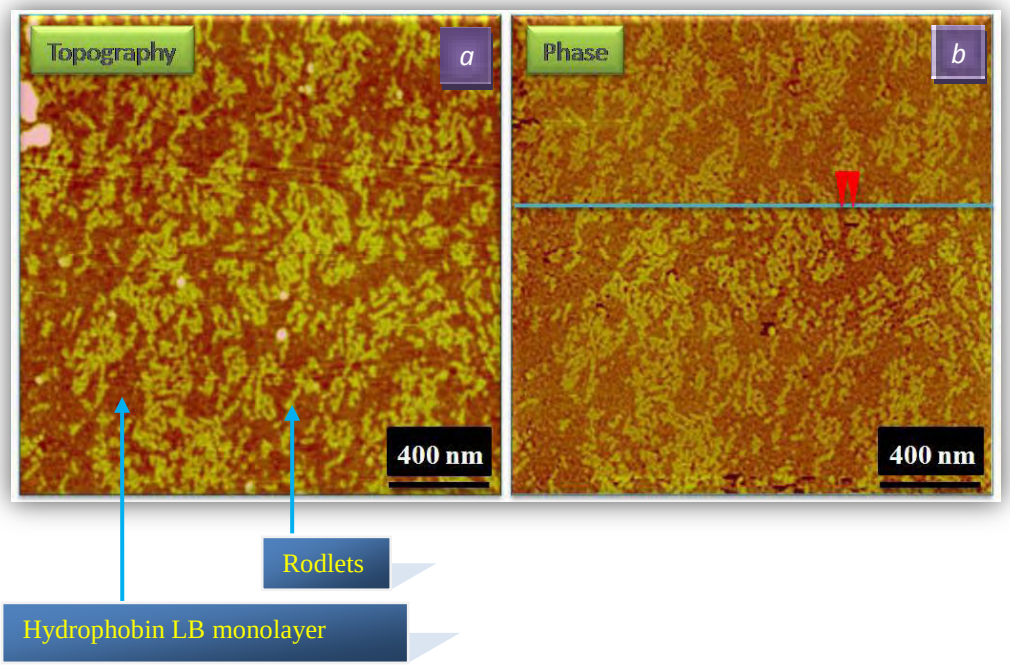

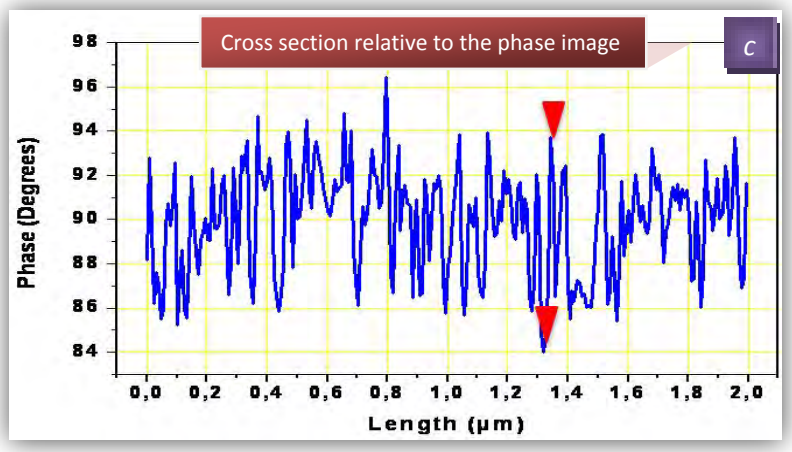

Figure 9. Tapping mode AFM characterization of hydrophobin LB film on SiO_2 wafer. Topography image (a) and phase image (b); the size of both images is 2 × 2 μm^2 and height scale 7 nm. (c) cross section that refers to the phase image. The phase difference between the top of rodlets and the surface of monolayer is about 8-10°. It is to be notted that the phase is presented here in real degrees and not in veeco degrees.

The thickness of the homogeneous film is measured by AFM by taking the cross section on the edge of the film along the line marked by the arrow, as shown in the figure 10 (the arrow in the left is placed in a hole, the other one is placed over SiO_2 surface without hydrophobin), it is about 2.5 nm. We can note that this value corresponds to the measured thickness for LB and LS hydrophobin films. Thus, the obtained homogeneous film in this case corresponds to the monolayer shown in the figure 7a when the LB film was deposited after one compression.

From figure 11, we have been able to estimate the rodlets size. The AFM image shows that the height of rodlets, measured from the upper surface of the monolayer, is about 2.3 nm. Consequently the height of rodlets is ca. 4.8 nm, (2.3 + 2.5 nm). The rodlets length ranges from 50 to 105 nm, and the width ranges from 19 to 24 nm. This last value has to be considered carefully because of the probe broadening effect. Taking into account a broadening by a 10 nm end radius tip, an actual rodlets width ranging from 6 to 11 nm appears consistent with our data and in agreement with data reported by other authors

[24] for different hydrophobins. On the contrary, measured heights are unaffected by the tip convolution effect and give a more reliable indication of particle size, as well as the length if it is significantly larger than 10 nm.

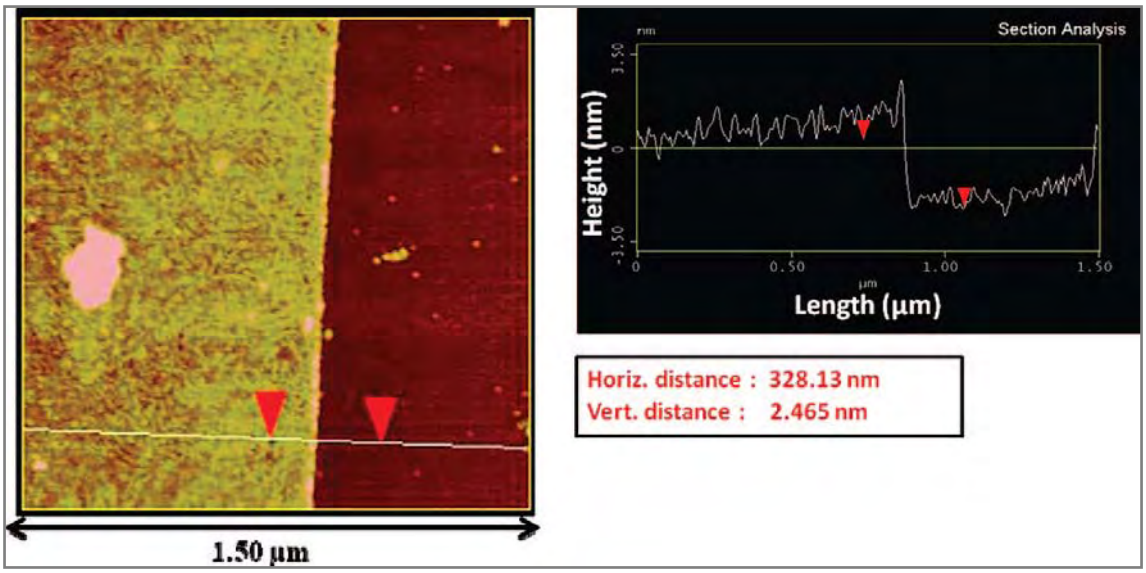

Figure 10. AFM topography image and section analysis of a hydrophobin LB film deposited on a SiO_2 substrate. The thickness of the monolayer is estimated as ca. 2.5 nm, image size is 1.50 × 1.50 µm2 and height scale 7 nm.

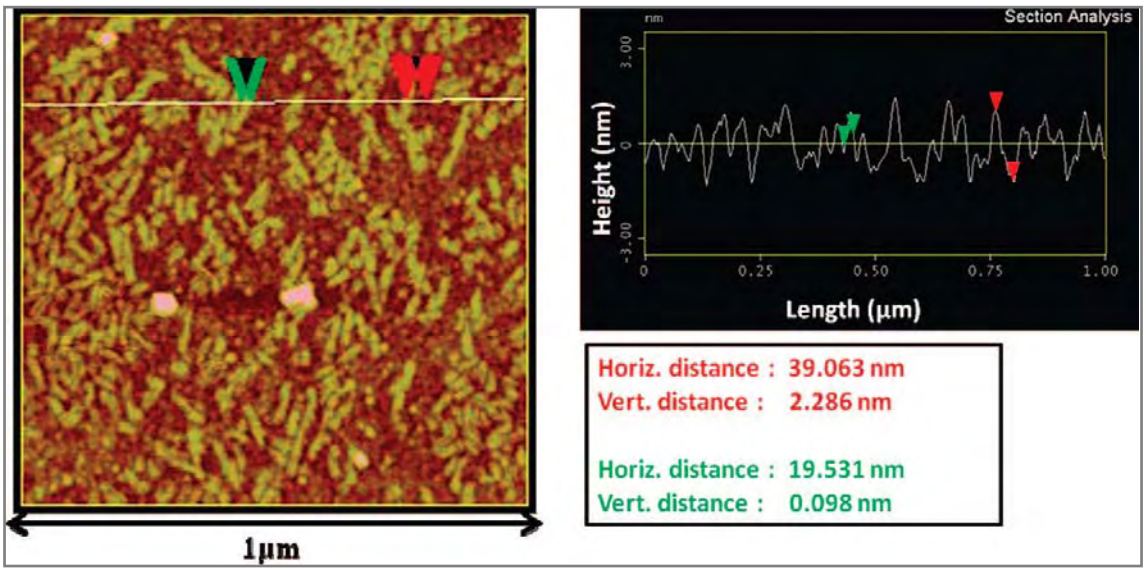

Figure 11. AFM topography images and section analysis of hydrophobin LB film deposited on silicon substrates: from (A) we estimate the rodlets height with respect to the LB monolayer as ca. 2.3 nm, image size is 1 × 1 μm^2 and height scale 7 nm.

The obtained thickness of monolayer is consistent with the result obtained by Wang et al. [25] for SC3 hydrophobin by ellipsometry measurements. They determined the thickness of the membrane formed at an air-water interface after several hours of incubation. When protein concentration was high (100 mg/ml), the membrane thickness after 10 min was determined to be 2.3 nm, and it slowly increased to the maximum of 3 nm after 5 hours incubation. This is may be due to the fact that the membrane formed at low protein concentration is less compact; either a larger space exists between molecules, or the orientation of the protein in the membrane is different.

4.4.3.1 A possible model for rodlets formation

Rodlets formation as bilayer: As it can be clearly observed in the phase image reported in Figure 6, a phase contrast exists between the top of the rodlets and the underlying monolayer, indicating that the AFM tip does not interact in the same way with the monolayer and the rodlets. Because of the LB film transfer procedure the upper surface of the hydrophobin LB monolayer must be hydrophobic as indeed verified by contact angle measurements. If we interpret this difference of phase contrast in terms of hydrophobicity, we could expect the upper surface of the observed rodlets to be hydrophilic. Hence the rodlets could be actually fragments of bilayer, whose hydrophobic sides are in contact, sinking in the LB monolayer (Figure 12). However, the molecular arrangement presented in the figure 12 may be more complicated than this, because the secondary structure of hydrophobins may change when they form rodlets, resulting in the changes in morphology [26]. The conclusion that the observed rodlets are hydrophilic would then suggest a possible molecular depletion mechanism: hydrophobins self-assemble into hydrophilic rodlets that can easily sink in the subphase. Other authors reported observations of the rodlets for other types of class I hydrophobin [27-29]. These rodlets are presumed to be

insoluble in water and have not been shown to exist in solution [30]. It is noteworthy that in our sample the rodlets concentration is very high in the sample area close to the upper end of the film (Figure10). This may likely due to the fact that the rodlets are preferentially formed close to the meniscus. This strongly suggests that the rodlets are formed at the air-water interface, as also discussed in Ref. [5].

Rodlets formation as monolayer: Although the described model of rodlets formation at the air-water interface as a hydrophilic bilayer using a Langmuir trough seems possible, due to the hydrophobin properties described in the chapter 1, especially related to the conformational change, another structure for the rodlets is possible. Indeed, the rodlets could be formed as monolayer as suggested by other authors [27]. In this case, since hydrophobin molecules adhere to the substrate by their hydrophilic part when the film is deposited by LB technique, the upper surface of rodlets should be hydrophobic. As we have highlighted by AFM measurements, the rodlets thickness is about 2 times higher than thickness of monolayer (figure 11). This suggests that the protein may adopt an extended conformation when rodlets are formed. This is already suggested by Zangi et al. [31] and Wösten et al. [32] concerning SC3 hydrophobin molecules for the same reason. At this point, both monolayer and rodlets are hydrophobic. However, as we have shown in the figure 6, the AFM tip-monolayer interactions and AFM tip-rodlets interactions are different. This could be due to the fact that, the hydrophobin molecules may contain hydrophobic parts that can present different degrees of hydrophobicity. Consequently, the rodlets show a hydrophobic side different from the hydrophobic one shown by the monolayer. And hence, during scanning of the sample, the tip interacts distinctly with the top of monolayer and the surface of rodlets.

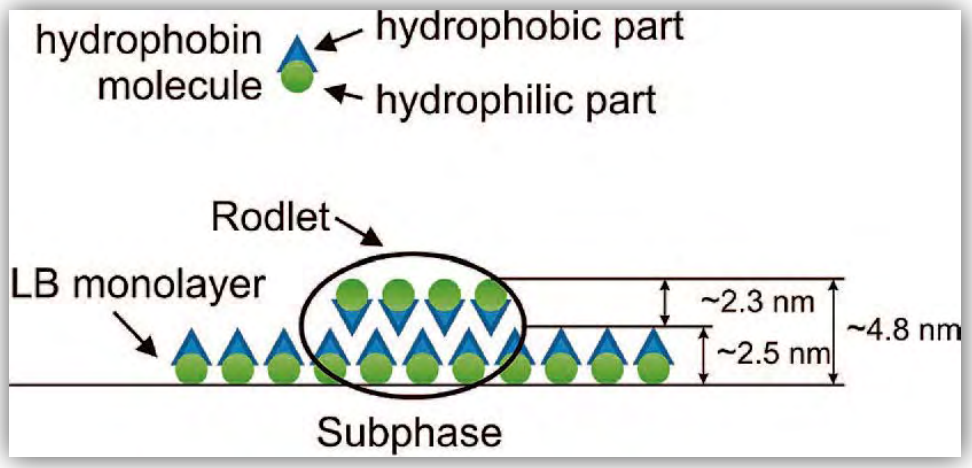

Figure 12. Oversimplified scheme of the molecular arrangement inside the LB monolayer and the observed aggregates.

4.4.3.2 Imaging of hydrophobin LB film in dry conditions

In order to understand the hydrophilicity properties of rodlets, the AFM imaging for hydrophobin LB film was performed in dry atmosphere (i.e 2 %RH). Figure 13 below shows the topography and phase AFM images associated with the cross section related to the phase image.

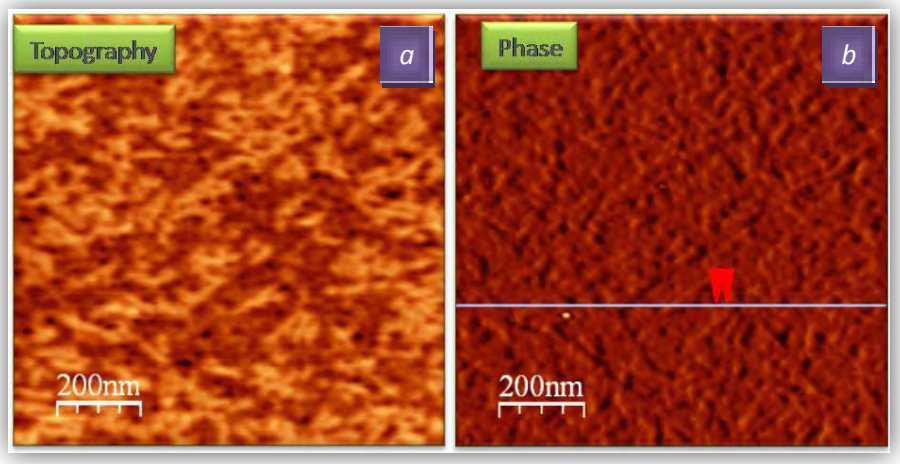

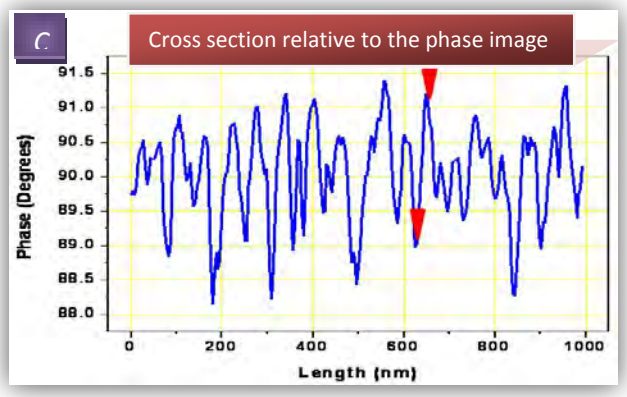

Figure 13. AFM images of hydrophobin LB film: (*a*) topography image, (*b*) phase image. image size is 1 × 1 µm^2 and height scale 4nm. (*c*) cross section that refers to the phase image. The phase difference between the top of rodlets and the surface of monolayer is about 2°. The phase is presented here in real degrees.

By comparison between the phase difference obtained between the top of rodlets and the surface of monolayer obtained in dry conditions (figure 13) and that obtained in ambient conditions (figure 9), we note that the phase contrast is considerably reduced; from ca. 8-10° in ambient conditions to ca. 2° at dry conditions. This could be interpreted in term of capillary forces that take part in the tip-rodlets interactions for the AFM measurements performed in ambient atmosphere, while at dry conditions the capillary effect is absent. The capillary interactions will be developed in the chapter 5.

The phase difference between the top of rodlets and the surface of monolayer is not significant. Because of the difference of height between the rodlets and the monolayer, this phase difference may be due to the artifacts related to the experimental parameters set in AFM imaging as setpoint amplitude and drive frequency. At this point, this AFM observation in dry conditions did not give us enough information capable to support one of the theses given above about the rodlets formation. For this aim, I have performed the approach-retract curves on rodlets but also in the LB monolayer; the results will be presented in the chapter 5.

4.5 Conclusion

In this chapter we have investigated the formation and the features of Langmuir films of class I hydrophobin from *Pleurotus ostreatus*. Compression-expansion cycles and constant pressure measurements demonstrated that the film at the air-water interface exhibits a molecular depletion toward the subphase. As consequence the number of molecules at the interface, and hence the area per molecule are unknown. In order to estimate the surface molecular concentration we analyzed the experimental pressure-area isotherms using a 2D equation of state Volmer-like. Moreover, when the Langmuir films are transferred onto solid substrates by LB and LS techniques, AFM observations revealed the formation of homogenous films with lower roughness. Furthermore, AFM images of the hydrophobin membrane after repeated compression cycles showed rodlets coexisting with LB monolayer. From these measurements we were able to estimate the rodlets size and the monolayer thickness: we suggest two possible models for rodlets formation: (i) the observed rodlets are actually formed by hydrophobin bilayers embedded in the LB monolayer. In this case, the observed rodlets could be hydrophilic supporting the hypothesis about a possible depletion mechanism occurring at least partly through the formation of hydrophilic rodlets. (ii) The rodlets can be formed as monolayer. In this case, the upper surface of rodlets should be hydrophobic when the film is deposited by LB technique suggesting that the protein adopts an extended conformation when the rodlets are formed.

Bibliography

[1] Luca De Stefano, Ilaria Rea, Paola Giardina, Annunziata Armenante, and Ivo Rendina, Adv. Mater. 2008, 20, 1529–1533.

[2] Qin, M., Wang, L., Feng, X., Yang, Y., Wang, R., Wang, C., Yu, L., Shao, B., Qiao, M., Langmuir, 2007**,** *23,* 4465-4471.

[3] Szilvay, G. R.; Paananen, A.; Laurikainen, K.; Vuorimaa, E.; Lemmetyinen, H.; Peltonen, J.; Linder, M. B., *Biochemistry*, **46**, 2345-2354, (2007).;

[4] Paananen, A.; Vuorimaa, E.; Torkkeli, M.; Penttilä, M.; Kauranen, M.; Ikkala, O.; Lemmetyinen, H.; Serimaa, R.; Linder, M. B., *Biochemistry*, **42**, 5253–5258., (2003).

[5] L. Yu, B. Zhang, G.R. Szilvay, R. Sun, J. Jänis, Z. Wang, S. Feng, H. Xu, M.B. Linder, M. Qiao, *Microbiol*., **154**, 1677, (2008)

[6] Kisko K, Torkkeli M, Vuorimaa E, Lemmetyinen H, Seeck OH, Linder MD, Serimaa R, Langmuir–Blodgett films of hydrophobins HFBI and HFBII. Surf Sci 2005; 584:35–40.

[7] Houmadi S, Ciuchi F, De Santo MP, De Stefano L, Rea I, Giardina P, Lacaze E, Giocondo M, **Langmuir 2008,** *24,* 12953-12957.

[8] Volmer, M. *Z. Phys. Chem. (Leipzig)*, **115**, 253, (1925)

[9] Fainerman, V.B., Vollhardt, D. *J. Phys. Chem. B,* **103**, 145, (1999)

[10] Vollhardt, D.; Fainerman, V.B.; Siegel, S. *J. Phys. Chem. B,* **104**, 4115., (2000).

[11] Fainerman VB, Vollhardt D. *J Phys. Chem. B*, **107**, 3107:3098, (2003).

[12] Wüstneck, R.; Fainerman, V.B.; Wüstneck, N.; Pison, U.; *J. Phys. Chem. B*, **108**, 1766-1770, (2004)

[13] Takai, S., *Nature*, **252**, 124–126, (1974).

[14] Identification of new members of hydrophobin family using primary structure analysis, K. Yang, Y. Deng, C. Zhang, M. Elasri. *BMC Bioinformatics* 2006, **7**(Suppl 4):S16

[15] Wösten HAB, de Vocht ML. Hydrophobins, the fungal coat unravelled. Biochim Biophys Acta 2000; 1469: 79 – 86.

[16] Karin Scholtmeijer, Meike I. Janssen, Bertus Gerssen, Marcel L. de Vocht, Babs M. van Leeuwen, Theo G. van Kooten, Han A. B. Wösten, Joseph G. H. Wessels1 J. G. *Appl. Environ. Microbiol.* **2002**, *68*, 1367–1373.

[17] M.I. Janssen, M.B.M. van Leeuwen, T.G. van Kooten, J. de Vries, L. Dijkhuizen, H.A.B. W.osten, Biomaterials 25 (2004) 2731–2739.

[18] R. Wang, Y.Yang, M. Qin, L. Wang, L. Yu,B. Shao, M. Qiao,C.Wang, X. Feng, Chem. Mater. 2007, 19, 3227.

[19] Wösten, H.A.B., Ruardy, T.G., van der Mei, H.C., Busscher, H.J., and Wessels, J.G.H. (1995). Coll. Surf. *B*. Bioint. *5*, 189–195.

[20] Wösten, H.A.B., Schuren, F.H.J., and Wessels, J.G.H. 1994.. *EMBO J.* **13:** 5848–5854

[21] Lugones LG, Bosscher JS, Scholtmeijer K, de Vries OMH, Wessels JGH. Microbiology **142** (1996), 1321-1329.

[22] R. Wang,Y.Yang, M. Qin, L. Wang, L. Yu,B. Shao, M. Qiao,C.Wang, X. Feng, Chem. Mater. 2007, 19, 3227.

[23] G.H. Wessels, *Adv Microb Physiol* **38**:1–45, (1997).

[24] M.B. Linder, G.R. Szilvay, T. Nakari-Setälä, M.E. Penttilä, *FEMS Microbiol Rev* **29**:877–896, (2005).

[25] X. Wang, Fuxin Shi, H. A. B. Wosten,§ H. Hektor, B. Poolman, G. T. Robillard, Biophysical Journal, 88 (2005) 3434–3443.

[26] de Vocht, M. L., Reviakine, I., Ulrich, W. P., Bergsma-Schutter, W., Wosten, H. A., Vogel, H., Brisson, A., Wessels, J. G., and Robillard, G. T. (2002) *Protein Sci.* **11,** 1199–1205

[27] Wösten H. A. B.; de Vries, O. M. H.; Wessels, J. G. H., *Plant Cell*, **5**, 1567-1574, (1993).

[28] Wösten, H. A.; Schuren, F. H.; Wessels, J. G. *EMBO J.*, **13**, 24, 5848-5854, (1994).

[29] Mackay, J. P.; Matthews, J. M.; Winefield, R. D.; Mackay, L. G.; Haverkamp, R. G.; Templeton, M. D., *Structure*, **9**, 2, 83-91, (2001).

[30] Stroud PA, Goodwin JS, Butko P, Cannon GC, McCormick CL, *Biomacromolecules* **4**, 956–967, (2003).

[31] R. Zangi , M.L. de Vocht, G.T. Robillard, A.E. Mark: *Biophys J*, **83**(1):112-124, (2002)

[32] Wösten, H.A.B., Asgeirsdottir, S.A., Krook, J.H., Drenth, J.H.H., Wessels, J.G.H., 1994. Eur. J. Cell Biol. 63, 122–129.

5. Beyond Topography using force spectroscopy measurements

5.1 Introduction

The atomic force microscopy has received an increasing attention during the last decade, and the number of possible applications of this technique increased significantly. In parallel, different modes of operation were developed in order to adapt the instruments according to the requirements given by specific sample types and scanning conditions [1]. In particular, different dynamic modes based on an oscillating cantilever driven by an external driver are applied to obtain topography of sample surface but also additional material specific properties. The atomic force microscope is a powerful tool for imaging a variety of systems and structures at the nanoscale [2-5] and characterizing them to get information about the local physico-chemical properties at nanoscopic scale [4].

The goal of this chapter is to develop a better understanding of the surface properties of the hydrophobin protein films when deposited onto solid substrates using force spectroscopy. It has to be noted that the hydrophobin proteins have been mostly investigated using scanning probe microscopy only in its topographic mode, although the force spectroscopic mode can provide meaningful information about the properties of samples. Its use for hydrophobins investigation remained very limited. To date, only three papers in the literature have studied the hydrophobins assemblies using the force spectroscopy [6] or the lateral force microscopy [7, 8]. Wang and co-worker [8] have reported an approach to modify the poly(dimethylsiloxane) (PDMS) surface with a class II hydrophobin HFBI. They employed the force curve

measurements in contact mode AFM with the Si_3N_4 tip functionalized using the protein bovine serum albumin (BSA) in order to probe the interaction between the tip and the surface of sample. They showed a weak adhesion force of 0.39 ± 0.01 nN between the BSA modified Si_3N_4 tip and the PDMS surface without hydrophobin, while a stronger one between the tip and the HFBI modified PDMS surface was revealed as 13.69 ± 0.01 nN. They attributed this stronger adhesive force between the BSA modified tip and HFBI modified PDMS surface to the conversion of PDMS surface groups from methyl to amine. This leads to the hydrogen bond formation between the tip and the amino functionalized PDMS surface. They concluded that the modification of the PDMS surface using HFBI biofilm turns the hydrophobic surface of PDMS to the hydrophilic one. This is consistent with the XPS and contact angle measurements that were reported in the same reference. However, the main problem associated with this study is that they did not take into account the possible formation of meniscus between tip the sample during AFM measurements.

On the other hand, de Vocht et al. [7] investigated the self-assembly of SC3 class I hydrophobin using the lateral force microscopy measurements performed in ethanol solution by chemically modifying the Si_3N_4 tip with amid groups. They highlighted a higher interaction between the hydrophilic AFM tip and hydrophilic surface of SC3 film. However, as I will demonstrate later in this chapter, I have found a strong interaction between the hydrophilic SiO_2 tip and hydrophobic surface of vmh2 hydrophobin.

In Tapping Mode, information on forces between AFM tip and sample may be obtained by measuring changes in phase lag, or/and amplitude of cantilever oscillation as a function of tip-sample distance. This allows to get information about the physicochemical properties of sample at a nanoscale resolution. In this chapter I will present the local properties investigation of the hydrophobin

films which were probed using atomic force spectroscopy in taping mode. I have determined the Hamaker constant related to van der Waals (vdW) forces of hydrophobin films from the phase versus distance curves, using an approach developed by R. D. Rodriguez [9] to analyze the region of the weakly interacting regime that is enclosed by a rectangle shown in figure 1. I have investigated the influence of the relative humidity on phase lag while operating an AFM in the tapping mode and studying the position of the jump from the attractive to the repulsive regime (see figure 1). I then give a demonstration of the use of AFM in Tapping Mode to characterize wetting properties as a function of humidity between hydrophobin films and AFM tip. It is shown that the formation of capillary meniscus can be detected at the nanoscale using approach-retract curves. Finall the presence of visco-elasticity in the tip-sample interactions directly linked to changes in phase was evidenced.

5.2 Experimental procedure

Hydrophobin films were prepared as described in the chapter 1. Force spectroscopy measurements have been performed using AFM in tapping mode at ambient humidity (ca. 40 % RH) and in dry conditions. Unlike the imaging mode, all approach-retract curves measurements were performed by exciting the cantilever at the resonance frequency. When the AFM scanner is operated controlled humidity, the microscope is placed inside a glass box. A self made humidifier allowed the control of the relative humidity by varying the ratio of dry/wet nitrogen flowing into the glass chamber. Humidity was measured using a commercial hygrometer with a range of measurements between 0 to 100 %RH with a precision of ±0.5 %RH. To avoid local gradients of water vapor, the system was left to stabilize for a long time, at least half an hour. Resonance frequency and Quality factor of the cantilever-tip system were determined experimentally from the resonance spectra as explained in the chapter 3. The

value of the quality factor was 20% lower in comparison to its free oscillation value as a consequence of changes in hydrodynamics of the surrounding air induced by the proximity of the sample surface [10]. We will see later that this error will play a role on the deduced values of tip radius but not on the deduced values of Hamaker constant. Free oscillation amplitude A_0 of the cantilever was determined from experimental approach-retract curves giving the variation of amplitude oscillations of cantilever as a function of tip-sample separation where A_0 corresponds to the amplitude when the tip is far from the sample (see figure 12 Chapter 3). Cantilever spring constant was determined taking into account its rectangular geometry using the Sader method [11]. Each series of experiment for all samples is carried out in the same conditions (i.e. same cantilever, same quality factor and same spring constant). In order to ensure that the tip radius remains unchanged during the measurements, the onset of the attractive forces in the phase distance curves measured for SiO_2 tip-SiO_2 surface before and after the measurements was analyzed. Only when the obtained tip radius was the same before and after measurements on the hydrophobin films, I recorded the measured data of the samples.

5.3 Theoretical aspect of the tip-sample interactions

5.3.1 Van der Waals force

The magnitude of the Hamaker constant reflects the strength of the vdW force between two particles, or between a particle and a substrate. It depends on the material properties of the interacting bodies and the intervening media [12]. Determination of Hamaker constants is an important field of research. A macroscopic approach based on quantum field theory, for determining Hamaker constants has been developed by Lifshitz [13]. In this approach, accurate calculations of Hamaker constants require the knowledge of the

dielectric and optical properties of the interacting materials over the entire frequency range of the electromagnetic spectrum. In general, this information is not readily accessible. Another approach is based on the measurement of force-distance curves using AFM in contact mode or surface force apparatus (SFA) [14] and a method based on the linear relationship of the yield stress with the square zeta potential (LRYSSZP) [15]. However, contact mode AFM method is limited by the instability introduced by the jump into contact, whereas SFA technique is adapted only to certain substrates such as mica support. On the other hand the (LRYSSZP) method is applicable only for particles in suspension in the liquid medium.

In this chapter, we have used the atomic force microscopy in dynamic mode by analyzing the phase versus tip-sample separation; we are concerned in this section by the weakly interacting regime that is indicated by a rectangle shown in figure 1 where long-range forces dominate. The important advantage to use tapping mode AFM is not only because it is a no-destructive method for soft and hard materials characterization, but also the fact that it can be operated in air, liquid and vacuum. This method has already been used previously, for example for a Ni tip interacting with a mica surface [11]. However, each time the tip radius was unknown which is a sever limitation for an exact determination of the Hamaker constant. Only recently in our group [9], we have developed a precise determination of the tip radius and consequently obtained a precise determination of the Hamaker constant of the SiO_2-SiO_2 system.

During AFM measurements, the first large distance contribution to the interaction between tip and sample is the long-range attractive van der Waals force, where the tip is assumed to be a sphere of radius R whereas the sample can be assumed to be flat.

For the sphere-flat geometry the van der Waals forces are represented by the relation [17]:

$$F_{vdw} = -\frac{HR}{6d^2}$$

where d is the tip-sample distance. This long-range force is directly related to the Hamaker constant H.

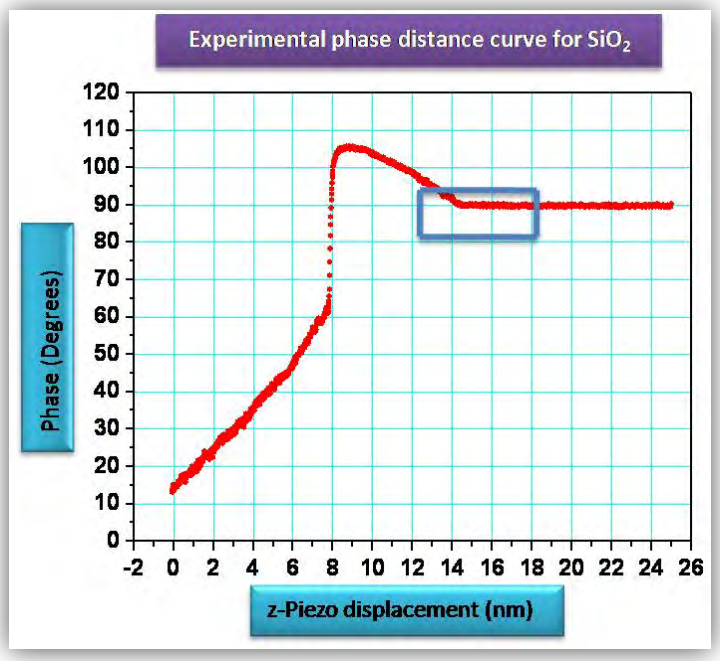

Figure 1. Experimental phase distance curve performed for a SiO_2 surface

Following the harmonic approximation, the effect of the tip-sample interaction can be accounted for as a shift in the effective spring constant of the cantilever [18]: $k_{eff} = k + \sigma$, where σ represents the sum of the force derivatives for all forces F_i acting on the cantilever

$$\sigma = \sum_i \frac{\partial F_i}{\partial z}$$

The phase ϕ of the interacting cantilever can be expressed as

$$\phi = \tan^{-1}\left(\frac{m\omega\omega_0}{Q\left(k + \sigma - m\omega^2\right)}\right)$$

where m, ω_0, ω, Q are respectively the effective mass, the resonance frequency, the vibrational frequency and the quality factor of the cantilever. Provided that σ is very small with respect to k. The phase angle $\phi$when the cantilever is exited at its resonance frequency is given by:

$$\phi = \tan^{-1}\left(\frac{k}{Q\sigma}\right)$$

If the cantilever is excited at its resonance frequency, the value of the phase when the tip is far from the sample (i.e. without tip-sample interaction) is ϕ_0 = 90°. The expression for the phase shift $\Delta\phi = \phi\text{-}\phi_0$ between the free and interacting cantilever is given by: $\Delta\phi \approx \frac{Q\sigma}{k}$. For van der Waals force, one gets the following equation in the framework of the harmonic approximation:

$$\sigma = \frac{\partial}{\partial z}\left(\frac{-HR}{6d^2}\right) = \frac{HR}{3d^3} \Rightarrow \phi = \phi_0 + \frac{QHR}{3k_c}\frac{1}{d^3} \qquad \text{Equation 1}$$

where the tip is represented as a sphere of radius R; Q is the cantilever quality factor, H is the Hamaker constant and d is the relative displacement between tip and sample.

Generally speaking, we are interested in this chapter by two important features: the attractive regime where the van der Waals forces dominate, in particular, the section of the phase curve where the onset of the attractive forces appears as indicated by the rectangle in figure 1 above, but also the position of the jump between attractive and repulsive regime (see figure 1). Although the harmonic approximation is generally not suitable to describe the dynamics of Tapping Mode due to the nonlinear effects that arise in the case of complex tip sample interaction and large cantilever amplitude, we will use it only for large tip-sample separations in which vdW force starts taking place. As previously shown, this allows to obtain an analytical expression that links the phase shift to the gradient of the interaction forces (see Eq. 1). In fact, by numerical

simulations for the SiO_2 tip-SiO_2 sample interaction, it has been previously demonstrated that the equation 1 is valid and the range within it holds has been defined (i.e. the region shown in a rectangle in Figure 1) [9].

In that reference a phase distance curve was obtained by numerical integration of Equation 2 shown below. The modeling by Equation 2 of the region shown in a rectangle in Figure 1 is presented in figure 2.

$$m\frac{d^2}{dt^2}z(t) + 2\beta m\frac{d}{dt}z(t) + k_c z(t) - F_0\cos(\omega t) = F_{ts}(z)$$

where $$F_{ts}(z) = \begin{cases} F_{vdw} = -\frac{HR}{6z^2}, & z > a_0 \\ F_{DMT} = \frac{4}{3}E^*\sqrt{R(a_0 - z)^3} - \frac{HR}{6a_0^2}, & z \le a_0 \end{cases}$$

Equation 2.

As previously described in chapter 3, z is the position coordinate of the cantilever, ω_0 and k_c are its resonance frequency and force constant in free oscillation respectively, m is the effective mass of the cantilever system, $F_0\cos(\omega t)$ represents the external driving force exiting the cantilever at the frequency ω. Dissipation with the surrounding atmosphere is taken into account by introduction of the term $\beta = \omega_0/2Q$.

Tip-sample interaction $F_{ts}(z)$ was associated with long range van der Waals force $F_{vdw} = -\frac{HR}{6z^2}$ and contact forces given by Derjaguin-Muller-Toporov contact mechanics (DMT): $F_{DMT} = \frac{4}{3}E^*\sqrt{R(a_0 - z)^3} - \frac{HR}{6a_0^2}$ where $a_0 = \sqrt{\frac{H}{24\pi\gamma}}$ is an intermolecular distance, E^* is the reduced elastic modulus of tip and sample, γ is the surface energy, H is the Hamaker constant and R the tip radius.

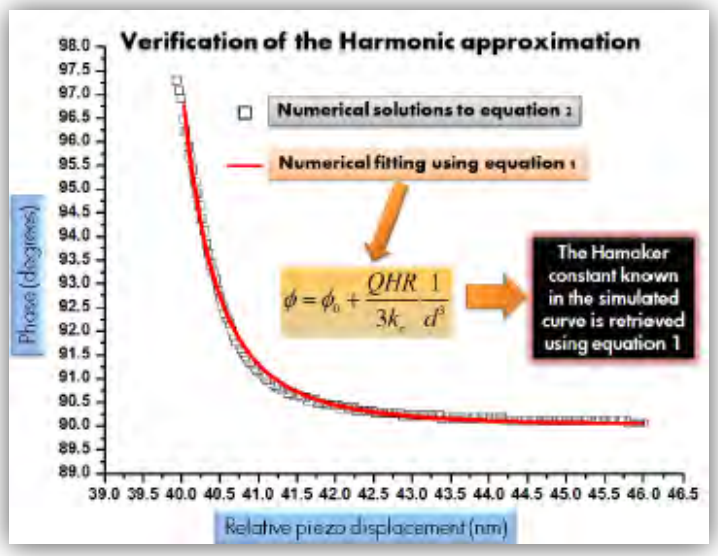

Figure 2. The square symbol is a numerical solution to Equation 2 calculated for a given average tip sample distance. It corresponds to a high resolution curve section (zoom) of the phase-distance curve marked by a rectangle in Figure 1. Continuous red line is given by numerical fit of Equation 1 to the symbol curve (solutions to Equation 2).

As shown in figure 2, at long distance the numerical fitting using equation 1 fits well the numerical solution to equation 2. Therefore, the harmonic approximation can be used for accurate Hamaker constant determination.

5.3.2 Wetting phenomenon and capillary forces

5.3.2.1 Introduction

The wetting phenomenon can be illustrated considering a small amount of liquid in contact with a solid. In one extreme case the liquid can wet the solid so well that it spreads completely. In the other extreme it avoids any contact with the solid and the droplet retains its individuality upon contact. The wetting depends on the affinity of the liquid for the surface. If the liquid is water and the surface is hydrophobic, no wetting is expected. Conversely, wetting by water will take place on hydrophilic surfaces. Between these extremes there is a range of intermediate situations in which the liquid meets the solid at a certain angle called the contact angle. Thus, the contact angle can be taken as a measure

of the relative hydrophilicity or hydrophobicity of the surface [19]. While macroscopic contact angle measurements provide averaged information on the wettability of the material substrate by the probing liquid over a large area, the use of AFM allows one to quantify wetting properties at nanoscale level. In fact, the AFM technique becomes now an important tool for studying and understanding of the capillarity phenomena including the capillary forces and adhesive forces as function of environmental conditions [20, 21]. The results obtained with contact AFM however appear to be not perfectly consistent. For example, for a Si_3N_4 tip radius 100 nm against a SiO_2 surface, the humidity at which a meniscus is measured varies from 35 to 50 %RH [22]. This discrepancy is related to the major role of the tip geometry in the meniscus formation. It is consequently important to determine hydrophilic behavior with tips of known geometry. Moreover, the disadvantage of AFM in contact mode is that it may damage soft samples. In contrast, the tapping mode AFM offers the possibility to investigate the effect of humidity on the soft materials such as biomaterials without wearing. By tapping mode AFM, Zitzler and co-worker [23] have investigated the effect of capillary force on the behavior of amplitude and phase of cantilever oscillations on Si surface. They show experimentally that during increasing of the relative humidity, the jump from the attractive to the repulsive interactions is suppressed. They explained this behavior using a model based on the intermittent formation of a capillary bridge between tip and sample close to the lower turning point of the cantilever oscillation. This finally demonstrates that, during tapping mode AFM measurements, a meniscus can be formed. This technique can thus be used to study a capillary phenomena at local scale. It is consequently interesting to use hydrophobin protein as a test material for the use of AFM in tapping mode to study hydrophobicity. As shown in chapter 4, we can indeed produce the same film presenting either the hydrophobic

surface, or the hydrophilic one towards the AFM tip. We have then decided to work in tapping mode, using tips of known geometry due to a careful analysis of the long distance approach-retract curves. This is an important step towards the study of more complex systems useful, for example, in biotechnology. Another novelty of this work is the use of phase lag as a function of humidity to detect the critical humidity for which capillary meniscus starts taking place.

Capillarity force arises from Laplace pressure caused by surface tension inside the meniscus, with also a direct surface tension component [12]. It is this latter term, surface tension, which drives spontaneous formation of meniscus. There is an energy cost to form the liquid bridge, bringing water molecules together from the vapor phase [24]. The energy required for this condensation is afforded by energy gained by wetting tip and surface. Meniscus will grow until mechanical equilibrium is reached which means that the pressure inside the meniscus has reached a stable value determined by the relative humidity, tip-surface distance, contact angles, principal radii of curvature and tip radius as shown in Figure 3.

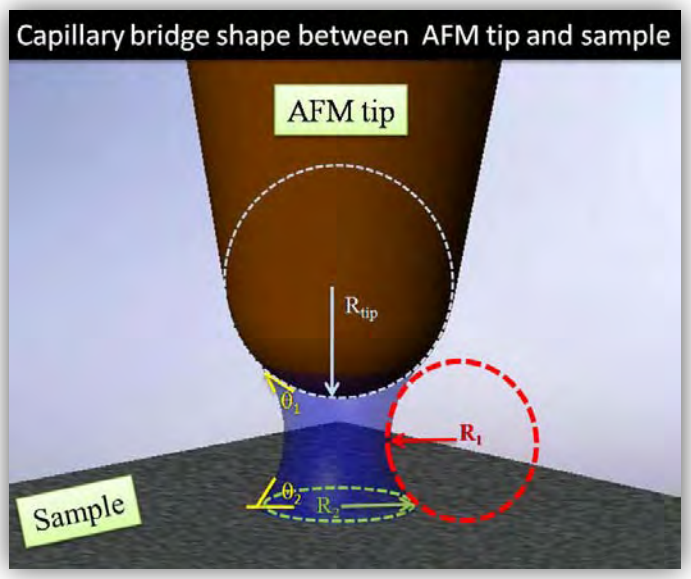

Figure 3. Schematic representation of meniscus between AFM tip with radius R_{tip} and sample. R1 and R2 are the two principal radii of curvature for the water meniscus, θ_1 and θ_2 are the contact angles for water on the tip and surface of sample respectively.

5.3.2.2 Theory

The Kelvin equation [25] represents the fundamental equation of capillary condensation at equilibrium. It describes the relationship between relative humidity and meniscus curvature formed between the AFM tip and the flat surface:

$$\frac{1}{R_K} = \left(\frac{1}{R_1} + \frac{1}{R_2} \right) = \frac{RT}{\gamma V_m} \ln\left(\frac{\%RH}{100} \right)$$

where R_K is the Kelvin radius, R_1 and R_2 are the principal radii of the meniscus as indicated in the figure 3, R is the gas constant, T the temperature, V_m the molar volume of the liquid, and γ the surface tension of the liquid.

The formation of a meniscus by capillary condensation leads to an attractive force between sphere and plate [26]. This so-called meniscus or capillary force is caused by the pressure difference between the liquid and the surrounding vapor phase. It is given by the Young–Laplace equation:

$$\Delta P = \gamma \left(\frac{1}{R_1} + \frac{1}{R_2} \right)$$

The capillary force F_{cap} between a plate surface and a sphere with radius R has been calculated by O'Brien and Hermann [26]. In the case of an AFM tip against plate surface (see figure 3) with radius R_{tip} much larger than the height of the water bridge h, the capillary force can be related to the tip sample separation d by two different expressions.

In the first expression, as the tip sample distance is changed, meniscus shape changes but its volume remains unchanged:

$$F_{cap}(d) = \frac{2\pi R_{tip} \gamma (\cos\theta_1 + \cos\theta_2)}{1 + \frac{d}{h}} \qquad \text{Eq. 3}$$

In the second approach, it is assumed that equilibrium is maintained, meaning that meniscus volume may change but not the Kelvin radius:

$$F_{cap}(d) = -2\pi R_{tip}\gamma(\cos\theta_1 + \cos\theta_2)\left(1 - \frac{d}{R_K(\cos\theta_1 + \cos\theta_2)}\right) \quad \text{Eq. 4}$$

If we further assume that both tip and sample are made of the same material, $\theta_1 = \theta_2 = \theta$, and that the surface tension force component is small enough to be neglected, both cases lead to the same maximum force value due to the liquid bridge when $d = 0$:

$$F_{cap} = 4\pi\gamma R_{tip}\cos\theta\,. \qquad \text{Eq. 5}$$

Under these assumptions the capillary force is actually humidity independent. This may be true at the macroscopic scale. However, it does not explain the behavior illustrated in Figure 3, since it does not take into account the variation of principal radii of curvature for the water meniscus that can be caused by the increase or decrease in water vapor. Thus, this expression usually is not applicable to nanometre sized menisci. Fisher and Israelachvili [27] measured the adhesion forces between curved mica surfaces in vapors such as cyclohexane and benzene and found that Eq. 5 is already valid once the relative vapor pressures exceed 0.1-0.2, corresponding to the meniscus radii of only 0.5 nm. It must be noted that this agreement was possibly related to the fact that the two interacting surfaces were similar to mica surface (i.e. similar geometry in particular).

The calculation performed by Pakarinen et al. [28] for the capillary pressure force showed that approximations which lead to the Equation 5 can be successful, but they become invalid at the nanoscale. They showed that for spheres of radius bellow 1 μm against a flat surface, capillary force depends strongly on humidity. They demonstrate using the exact profile method of capillary force at equilibrium that the constant volume approximation (i.e. Eq. 3) predicts for a spherical particle of 100 nm radius, that meniscus breaks off at a distance of 10 nm, while Equation 4 predicts that meniscus breaks already at

1.65 nm. Due to the fact that the tip movement is much slower than the time needed for meniscus to reach equilibrium [28], it can be concluded that the correct description is the one given by the Eq. 4. A careful analysis of AFM results could finally also help to discriminate between the two cases.

5.3.3 Energy Dissipation

When AFM is operated in dynamic mode, in addition to the amplitude phase distance curves, an interesting and complementary approach to analyze the forces involved in the tip-sample interaction is based on the analyzing of energy dissipated when the tip periodically interacts with the sample surface. Several studies have been devoted to the forces involved in tip–sample interaction in tapping-mode AFM. It was demonstrated that the phase lag depends on the energy dissipated between the tip and the sample [29-31].

The input dissipative power P_{in} can be decomposed into two terms: the power dissipated by the motion of the cantilever beam P_0 and that dissipated by tip–sample interaction P_{tip}

$$P_{in} = P_0 + P_{tip} \qquad \text{Eq. 6}$$

We are interested in the term P_{tip}, since it is a direct physical quantity which characterizes the tip–sample interaction. Cleveland et al. [30] have calculated P_{in} and P_0 for cantilever driven sinusoidally with amplitude A_d and frequency ω as follow:

$$P_{\text{int}} = \frac{1}{2} k_c A_d A \omega \sin\phi$$

$$P_0 = \frac{1}{2} \beta A^2 \omega^2$$

Then P_{tip} is obtained as:

$$P_{tip} = P_{in} - P_0 = \frac{1}{2}\frac{k_c \omega}{Q}\left[Q A_d A \sin\phi - A^2 \frac{\omega}{\omega_0} \right] \qquad \text{Eq. 7}$$

As already defined previously, A is the oscillation amplitude, ϕ is the phase lag, k_c is the spring constant, $Q = {k_c}/{\beta\omega_0}$ is the quality factor, β is a dissipation term, ω_0 the natural resonant frequency of the free oscillating cantilever.

When the driving amplitude is chosen to be ω_0, the relation can be simplified as below:

$$P_{tip} = \frac{1}{2}\frac{k_c A^2 \omega_0}{Q}\left[\frac{A_0}{A}\sin\phi - 1\right] \qquad \text{Eq. 8}$$

Equation 8 can finally be used to evaluate the energy dissipated between the tip and hydrophobin films.

5.4 Results and discussion

5.4.1 Determination of Hamaker constant

For Hamaker constant determination AFM scanner is operated in dry environment to avoid the capillary forces effect. As one can see in the equation 1, in order to determine the Hamaker constant the knowledge of tip radius is necessary. For this aim, I have used the SiO_2 tip-SiO_2 surface system whose Hamaker constant was determined in our group by R. D. Rodriguez [9]. The found value was 6. 10^{-20} J, in good agreement with the calculated ones using Lifshitz theory and full spectra data for SiO_2-SiO_2 system [32, 33]. Hence, for each experiment, phase distance curves performed for SiO_2 tip against SiO_2 surface were fitted using equation 1 (see figure 4). In figure 4, is presented an example of the phase vs distance curve where the region marked by a rectangle in figure 1 is fitted using the quality factor and the spring constant of the cantilever determined experimentally. For the example of figure 4, they were

respectively 449 and 30 N/m. From this fit the tip radius was extracted five times and values ranging from 11.5 to 14.5 nm giving average value of 13 ± 1.5 nm were obtained. It has to be noted that the error in the tip radius was calculated using $\frac{R_{max} - R_{min}}{2}$.

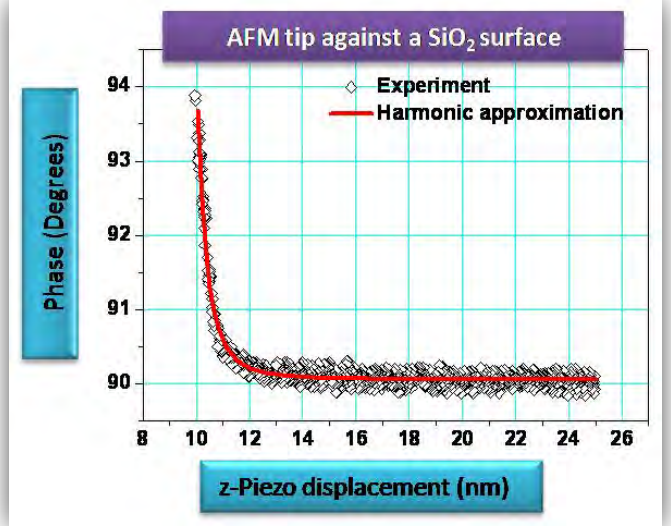

Figure 4. Experimental phase distance curve performed for SiO_2 : the region marked by a rectangle in figure 1 is fitted by the equation 1 giving the value of tip radius.

At this point, after the determination of the tip radius, we turn to experimental measurements of phase distance curves measured against hydrophobin LB film which was deposited on the SiO_2 surface and hydrophobin LS film deposited on silanized SiO_2 in order to experimentally deduce the Hamaker constant using equation 1 (see figure 5). In figure 5, an example of the fitted experimental phase versus distance curves which allowed the extraction of the Hamaker constant using the harmonic approximation is presented.

Phase-distance curves were measured against several hydrophobin films (see table 1). A fitting of experimental phase distance curves, using eq. 1, leads to *HR* value. Knowing the tip radius, the Hamaker constant value is then deduced for each tip radius.

In doing this, Hamaker constant values ranging from 1.92 to 3.52 × 10^{-20} J are obtained for LB hydrophobin film leading to an average value of 2.67± 0.8 × 10^{-20} J and ranging from 2.13 to 3.27 ×(10^{-20} J) are obtained for LS hydrophobin film leading to an average value of 2.18±0.57 × 10^{-20} J, as illustrated in the table 1 bellow. It has to be noted that, because of the product *HR* in the Eq.1 which is used for the fit of phase distance curves there is a direct contribution from the error in the tip radius which propagates to the value of the Hamaker constant as following : $\Delta H = \frac{\Delta R}{R} H$. Thus the error in the Hamaker constant presented in the table 1 is not a direct expression of the experimental error on *H* but it comes rather from the error in the tip radius which is actually related to the fit of the phase diatance curves performed for SiO_2 tip-SiO_2 surface.

As I reported above, the Harmonic approximation has been demonstrated valid at long distance for hard materials such as SiO_2 surface and the precise Hamaker constant of SiO_2/SiO_2 system in air was determined in the framework of this model [9]. However, this may be not true for soft maters, because in such case, it remains possible that the tip could penetrate the sample when the tip sample interactions start taking place. In this case, the tip should interact not only with hydrophobin film but also with the surface on which the film is deposited (i.e. SiO2 surface in the case of LB film and silane in the case of LS film). However, the fact that we obtain a *H* value smaller than that for SiO_2/ SiO_2 system suggest that the tip remains far from SiO_2. In particular, the distance where most of the van der Walls interactions take place as shown for SiO_2 [9]. Moreover, the results are not aberrant, since the difference of the obtained values is not excessively large, whereas the tip radius varies from 6 to 27 nm. Although *H* values have to be considered carefully, certain credibility could be given to these values.

We note then, that the obtained values for both films are of the same order of magnitude**.** This result shows that the AFM tip interacts in the same way with both LS film and LB one in the beginning of the tip-sample interactions. So, at long distance, when the tip approaches the sample and vdW force starts to take place, the tip interacts not only with the hydrophobic part of the LB monolayer (respectively hydrophilic part of LS monolayer) but with the average of both parts of hydrophobin molecule. This is interesting because the fact that both films posses the same order of magnitude of the Hamaker constant can be a way to be sure that both films transferred on solid surfaces by two different techniques are the same films; they differ only by the nature of the side in contact with air.

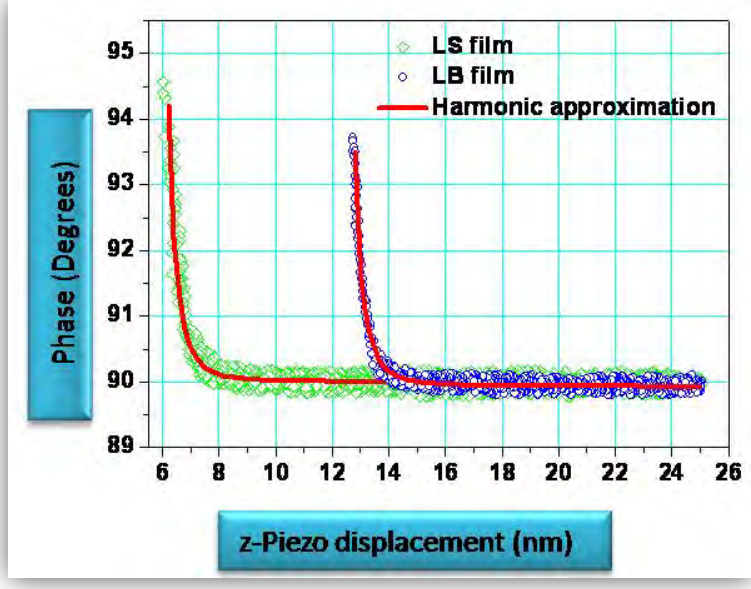

Figure 5. Experimental phase distance curves of LB film (blue) and LS one (green) fitted in the framework of harmonic approximation (red line) using the value of the tip radius obtained from figure 3 to estimate Hamaker constants of hydrophobin films.

Tip radius *(nm)*	R_1 6±1.8	R_2 9±2.2	R_3 13±1.5	R_4 18±2.1	R_5 27±2.6
***H* for LB film (10^{-20} J)**	2.35±0.70	1.92±0.46	2.90±0.33	3.52±0.41	2.70±0.26
***H* for LS film (10^{-20} J)**	3.27±0.98	2.13±0.52	2.7±0.31	2.8±0.32	3.12±0.30

Table 1. Hamaker constant measured for both hydrophobin films by analyzing experimental phase vs distance curves performed for different radius tip are summarized. radii are given in nm and Hamaker constants in (10^{-20} J) R_1, R_2, R_4 and R_5 were taken from the fit of data measured during several AFM sessions (not shown in the text), R_3 was obtained from data shown in Figure 4.

We note nonetheless, that the Hamaker constant measured for hydrophobin protein is small with respect to the reported one measured for SiO_2 surface [9, 32, 33]. This shows that the polarizability of protein is lower than the one of SiO_2. Generally speaking, materials with high polarizability (as reflected by their high dielectric constant and refractive index) present Hamaker constants which can be up to an order of magnitude higher than those with low polarizability [12].

5.4.2 Local wettability of hydrophobin films

One of the goals of this chapter is to find out using tapping mode AFM if we can observe effects of humidity in the behavior of the phase lag as a function of tip-sample distance and determine the critical relative humidity at which the formation of capillary meniscus starts to take place using tips of known radius. Indeed, tracking changes in the phase signal as a function of humidity could allow to study wetting phenomena between tip and sample at the local scale.

5.4.2.1 Wetting properties of hydrophobin LS monolayer

The evolution of phase distance curves were investigated for hydrophobin LS film as a function of relative humidity in order to detect the transition humidity for which meniscus condensation starts to take place.

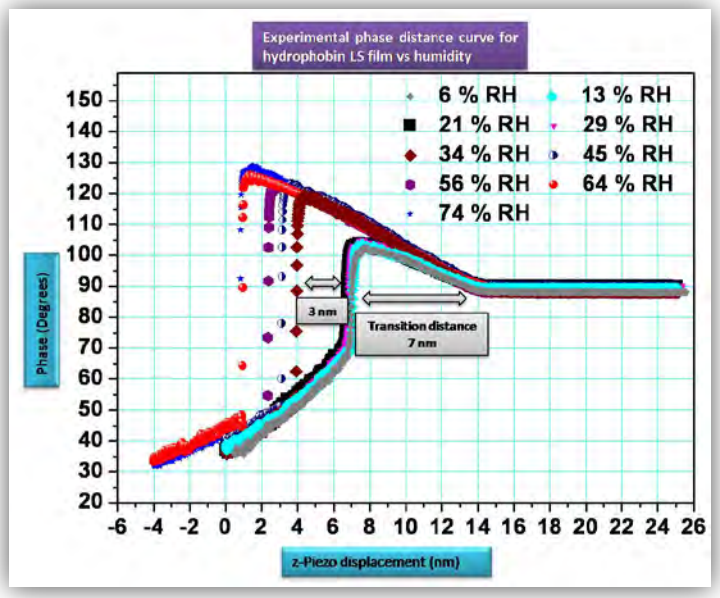

Figure 6. Experimental phase distance curves performed for LS hydrophobin film at different humidity using SiO_2 tip of radius ca. 28 nm.

In figure 6, approach curves in tapping mode AFM are presented at different humidity values, in the range 6% - 74%, for a tip of radius 28 ± 3 nm measured according to the procedure explained previously in the experimental procedure. In this case, I was not able to use the SiO_2 surface for the tip radius

determination; I determined then the tip radius using the obtained average value of *H* for the protein LS film to analyze the onset of the attractive forces in the phase distance curves measured for SiO_2 tip against LS film.

The jump from attractive regime to repulsive one takes place at 7 nm from the onset of phase increasing at "low" humidity (RH = 6%) (see figure 6). It appears that between RH 6 % and 34 % the jump position does not vary. On the other hand, the jump distance becomes higher when the relative humidity attains 34 % and continues to increase when the humidity is further increased. These results must be connected to the absence of meniscus between the tip and the sample at low humidity: for RH < 34 % the water vapor is not sufficient to condensate between tip and sample. Consequently, at low humidity level, in the attractive region, the tip-sample interaction is mainly dominated by vdW force. On the other hand, the jump shifts to the left when the relative humidity has attained 34 %, that is associated with the increment in the attractive forces due to the addition of capillary forces. This is the signature of capillary meniscus formation between tip and the surface of LS film giving rise to attractive capillary forces. We note also that the attractive region increases when relative humidity increases even when the RH value is above 34 %. This is not surprising because capillary forces depend on the size of meniscus formed between the tip and the sample as expressed by the equation 4 that relates the capillary force to the Kelvin Radius. When R_K increases F_{cap} increases, so, when the humidity increases the capillary force increases and thus the attractive interaction increases. However, it has to be noted that the attractive forces are equal for the case of 64 and 74 % RH. This is due to water saturation. Indeed, the meniscus grows in size, until the rate of evaporation and condensation is in equilibrium [28].

The variation of the phase signal vs humidity shows that the formation of capillary meniscus starts to take place at a critical value around 34 % RH. This confirms the obtained result in chapter 4 concerning the hydrophilic character of hydrophobin LS film. Indeed, water condensation able to form a capillary bridge between tip and surface requires less water vapor for hydrophilic samples than for hydrophobic ones, and already at 34 % RH, a meniscus can be formed between tip and surface. This method appears a new and interesting way to measure the hydrophilicity of samples at nanoscale level using AFM probe. R. D. Rodriguez [9] has similarly investigated the phase signal measured on the SiO_2 support at different humidities using SiO_2 AFM tip with effective radius of 16±5 nm. He found that no effect of humidity in the phase distance curve was observed at low RH, while around 20%RH an increase of the region corresponding to the attractive forces took place. However, comparison in hydrophilicity between different samples has a sense only if the tip radii are comparables, which is currently not the case.

In the figure 7, phase distance curves performed by the same SiO_2 tip for hydrophobin LS film and SiO2 surface at ambient humidity (figure 7a) and in dry condition (figure 7b) are presented.

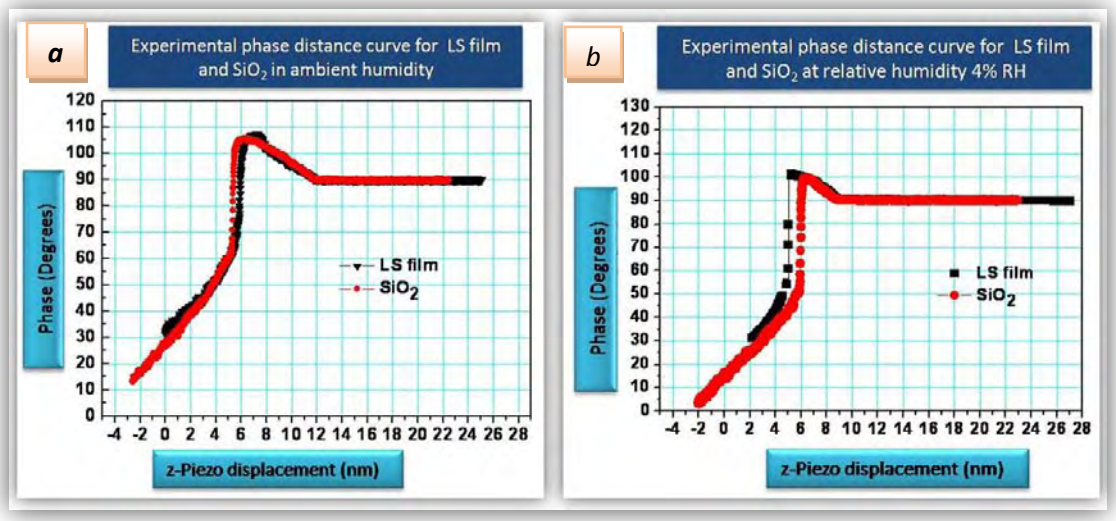

Figure 7. Experimental phase distance curves performed for hydrophobin LS film and SiO_2 surfce (a): at ambient humidity, (b) in dry atmosphere.

From these figures, for the same tip radius, we note that the jump position is similar for the tip-protein LS film system and for the tip-SiO_2 system at ambient conditions and in dry conditions. This suggests that the two surfaces are comparables in term of wettability: indeed for the same tip radius the formation of capillary meniscus starts to take place between the tip and SiO_2 surface in one hand and between the tip and protein LS film in the other at the same critical humidity. This result is in agreement with contact angles measurements which display similar values for LS film and SiO_2 surface equal to 43° and 37° respectively.

It has to be also noted that, while measuring phase-distance curves as a function of relative humidity, paying special attention to the tip radius is recommended, because the tip shape modification occurs frequently while measuring phase-distance curves, particularly when the capillary meniscus starts to take place. For this reason it is necessary to verify at the end of experiment that the radius tip did not undergo change.

It appears finally that AFM in tapping mode would reliably describe the hydrophobicity of one given sample if the curve of the critical humidity for

which the jump is modified can be obtained as a function of the tip radius. Such a curve could be used to compare different samples and their corresponding hydrophobicity. Together with the calculation of the meniscus geometry for a given tip radius, this could help to understand how the meniscus is formed in an AFM tapping mode experiment, and also this could help for a better understanding of the structure of meniscus between tip and sample at nanoscale.

Already our results confirm that, for AFM experiments, the capillary forces are not independent of humidity. Thus the hypothesis given by the Eq. 5 does not hold.

Moreover, based on the result of Pakarinen [28], which predicts that the meniscus would break already for a tip sample distance of 1.65 nm, the fact that meniscus formation is detected in our systems strongly suggests that, before the jump, the tip at the end of oscillating cycle, is extremely close to the sample, in other way, close to the contact point in order to establish a meniscus.

A description of meniscus formation as a function of the relative humidity would be interesting concerning the questions of tip radius determination. Indeed, for a given sample, determine and plot the critical humidity as a function of the known tip radii would now offer a possibility to determine from the plot unknown radius whatever the tip provided that the critical humidity is known.

5.4.2.2 Wetting properties of hydrophobin LB monolayer

In order to determine the local wettability of the hydrophobin LB film, the phase distance curves were studied at different RH for a tip of radius 28 ± 3 nm measured according to the way explained in the experimental procedure: I analyzed the onset of the attractive forces in the phase distance curves

measured for SiO_2 tip against SiO_2 surface before and after that performed for SiO2 tip against protein LB film.

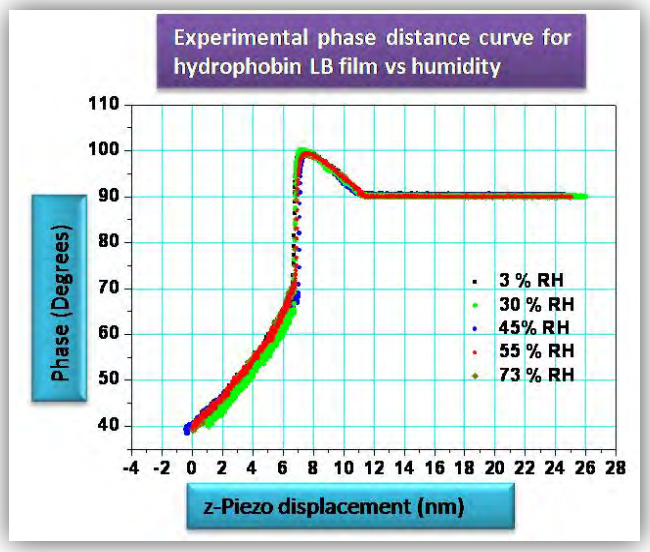

Figure 8. Experimental phase distance curve performed for hydrophobin LB film versus relative humidity (RH). For clarity phase signals measured at 10, 15, 20, 40, 50, 60 and 65 % RH are not shown in the graph. No change in the phase shift vs humidity was observed.

From the figure 8, we note that, by varying the relative humidity the phase versus distance curves remain unchanged even at extremely higher relative humidity as large as 73 %RH. This means that no meniscus is formed between the AFM tip and the sample, in agreement with the hydrophobic character of hydrophobin LB film. Thus, this result confirms the obtained result in the chapter 4 where the hydrophobic nature of hydrophobin LB monolayer was evidenced using contact angle measurements. This also confirms the ability of AFM in tapping mode to distinguish between hydrophobic and hydrophilic surfaces, in agreement with result obtained by Zitzler et al. [23] for AFM tip against hydrophilic (mica) and hydrophobic substrate. This later was obtained by exposing mica surface to a saturated vapor atmosphere of heptadecafluoro-1,1,2,2-tetrahydrodecyldimethylchlorosilane (PFS) for 1 to 2 hours. They studied the influence of the relative humidity on the oscillation amplitude of cantilever interacting with sample and have found that, if the free oscillation

amplitude A_0 exceeds a certain critical amplitude A_c, the amplitude phase distance curves showed a jump from an attractive regime to a repulsive one. For hydrophilic tip and sample this critical amplitude A_c is found to increase with increasing relative humidity. In contrast, no dependence on the relative humidity was found for hydrophobic sample. We now demonstrate that directly, the evolution of the jump with the humidity allows to study the hydrtophobicity. In particular the critical humidity where the meniscus between tip and sample is formed can be determined.

5.4.3 Phase distance curves and visco-elastic properties

5.4.3.1 Phase distance curves at ambient humidity

Figure 9 below shows the variation of the phase versus distance performed at ambient humidity, using the same tip for all the samples.

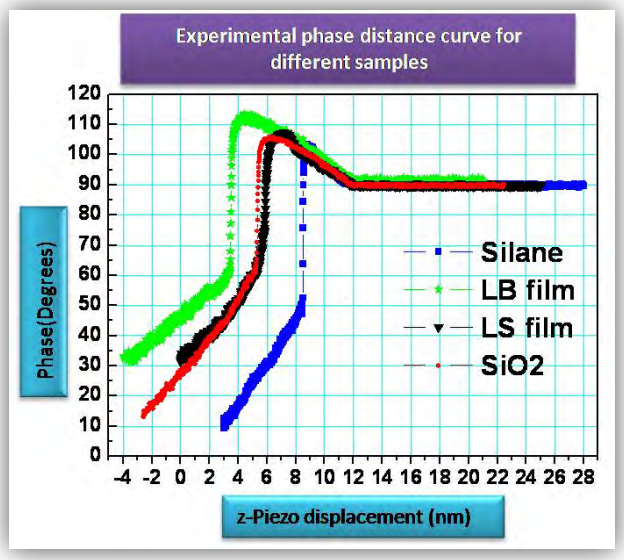

Figure 9. Experimental phase distance curves performed for hydrophobin films, SiO_2 and silanized SiO2 surfaces on air.

Experimental phase distance curve performed for hydrophobin films, SiO_2 and silanized SiO_2 surfaces in ambient conditions are presented in the figure 9. In the figure 9, one can see that the jump position is similar for the tip-protein LS

film system and for the tip-SiO_2 system; on the other hand, the jump occurs earlier for the AFM tip-silane system, whereas it occurs later for the tip-hydrophobin LB film system.

We can explain the behavior of the phase lag concerning tip against hydrophobin LS film and Tip against SiO_2 by the hydrophilic character of the system, also confirmed in the chapter 4 by contact angle measurements; the treatment of SiO_2 surface with piranha solution gives a hydrophilic character of SiO_2 [34]. So, the hydrophilic nature of these samples gives rise to meniscus formation between the tip and sample at ambient humidity (~ 40 % RH). On the other hand the surface of silanized SiO_2 is hydrophobic, and then the meniscus cannot be formed in this case, because water condensation able to form a capillary bridge requires more water vapor for hydrophobic samples in contrast to hydrophilic ones.

For hydrophilic samples, in addition to the vdW interaction, the capillary forces contribute to the tip-sample interactions. This is why the attractive forces are larger in the case of LS film and SiO_2 surface instead to the hydrophobic silanized SiO_2 substrate. The surprise came from the variation of the phase versus tip-hydrophobin LB monolayer separation. Indeed, as demonstrated before, the surface of the protein LB film is hydrophobic and then its hydrophobic character prevents the formation of the meniscus, thus the attractive forces between the AFM tip and LB film should be weak in the absence of capillary forces. As illustrated in the figure 9 the attractive regime seems to be predominant.

In order to confirm this interpretation, we have performed approach-retract curves in dry conditions to avoid effect of the capillary force (figure 10).

5.4.3.2 Phase distance curves in dry conditions

The figure 10 illustrates the variation of the phase lag versus distance for different samples at relative humidity 4% (i.e. dry atmosphere). As we can see, the region of attractive forces characterized by phase values higher than 90° is similar for the tip-hydrophobin LS film, tip-SiO_2 surface and tip-silane surface interactions. This is due to the fact that at low humidity there is not enough water vapor to condensate between tip and sample, so the capillary bridge can't be formed between the tip and hydropphobin LS film on one hand and between the tip and SiO_2 surface on the other. Therefore, there is not capillary forces contribution to tip-samples interactions. Consequently in the attractive regime only the van der Waals forces dominate in this case.

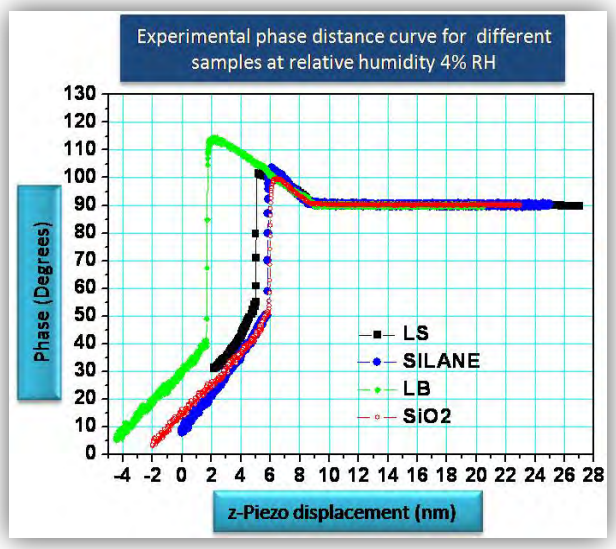

Figure 10. Experimental phase distance curve performed for hydrophobin films, SiO_2 and silanized SiO2 surfaces in dry atmosphere

In the figure 10, we not that the attractive forces dominate the tip-hydrophobin LB film interactions even at lower humidity. This confirms that the particular interaction highlighted between the tip and hydrophobin LB film on air and at dry atmosphere is not due to the capillary force contribution.

There are at least two possible interpretations:

a. The particular interaction could be of chemical nature related to nature of the hydrophobic side of protein molecules. As we have seen in the chapter 1 the hydrophobic part of hydrophobin is partially formed by hydrophobic aliphatic side chains [35]. However, the silanes also are believed to form chemically anchored monomolecular films with an array of aliphatic side chains [36]. According to the figure 10, the silane surface does not present any particular interaction with the AFM tip. We can then conclude that, the particular interaction highlighted between the tip and the hydrophobin LB film should not be associated with the hydrophobic part of the molecules in aliphatic chains. However, this interaction may be related to adhesion force between the AFM tip and the loop that links the strands in the beta barrel structure, since as reported by Kwan et al. [37], it is much larger in the class I hydrophobin in comparison to the class II and mainly hydrophobic [37], and thus a priori located at the surface of LB film.

b. A possible explanation may be associated with the viscoelastic nature of hydrophobin LB film with respect to the LS one. Indeed, instead of class II hydrophobins which have a globular structure (*see figure of HFBI molecule Chapter hydrophobin*) the structure of class I hydrophobins is asymmetric as we can see in the figure 13. Thus, when the hydrophobin is deposited onto hydrophobic substrates, a loop of molecule binds strongly to a hydrophobic surface in an α-helical state as reported by Wang et al. [38] on Teflon substrate for Sc3 hydrophobin, resulting in the formation of a stable monomolecular film. Fan et al. [39] have also showed that Sc3 hydrophobin may preferentially attach to a hydrophobic surface via the loop region between the third and fourth Cys and that this region is critical for the formation of the α-helical state on the substrate.

In contrast, when the hydrophobin molecules is deposited onto hydrophilic substrate, they adhere to the surface by their hydrophilic part and the adsorption on hydrophilic surface appears to have a significantly lower rate than the adsorption of hydrophobic side to the hydrophobic surface [40], indicating different modes of hydrophobin adsorption for these two surfaces. This suggests that the LS film when adsorbed to the hydrophobic silanized SiO_2 surface could form a more rigid monolayer than the LB film adsorbed to hydrophilic SiO_2 surface. In particular, the loop pointing at the surface in contact with air, for the LB films could be particularly soft.

At this point, the particular interaction highlighted in the figure 9 and 10 between the tip and the LB protein film may be due to the difference of rigidity between LS and LB films. In fact, this difference in rigidity makes the LB film more compressible during interaction with AFM tip than the LS film.

5.4.3.3 Adhesion force on hydrophobin films

In order to get more information about hydrophobin films in terms of adhesion, I have performed the force curve measurements in contact mode AFM for both hydrophobin films in dry conditions using the same cantilever for each series of experiments. Si_3N_4 V-shaped cantilevers were used with 0.06 N/m spring constant. Force is measured by collecting a force curve, which is a plot of cantilever deflection as a function of sample position along the z-axis. This plot is converted from volts to force unit as explained in the chapter 3. Five series of experiments were performed and better data reproducibility was achieved. The force at the pull-off point corresponds to the adhesion force between the tip and the sample as indicated in the figure 10.

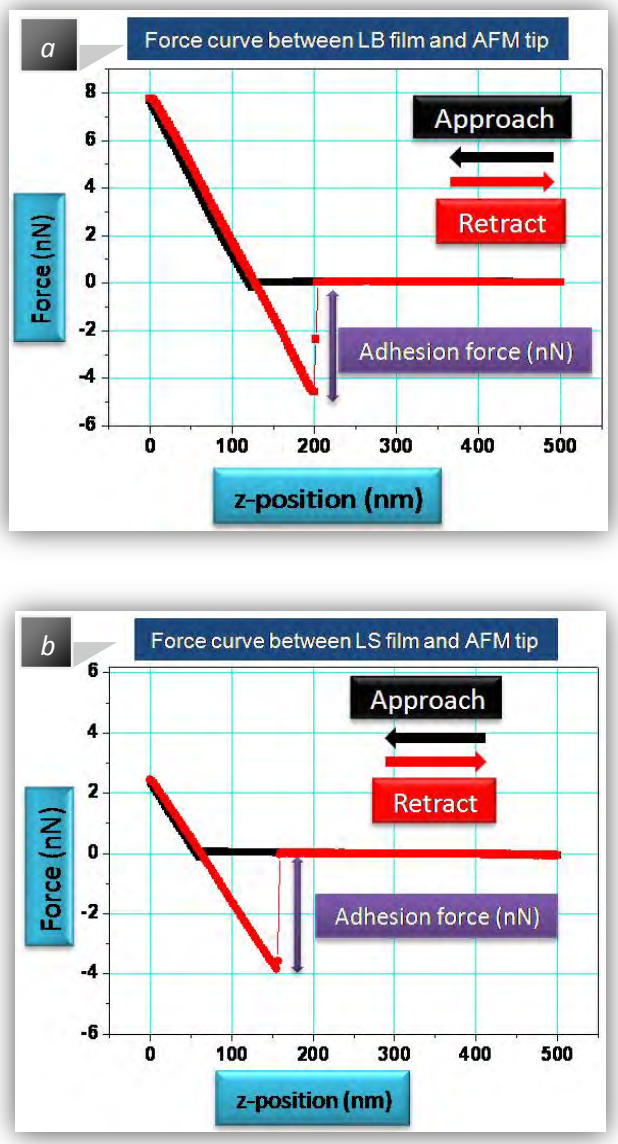

Figure 11. Typical force curve measurements: (*a*) hydrophobin Lb film and (*b*) hydrophobin LS film. Experiments are performed in dry conditions.

Typical force curve measurements obtained experimentally for the tip interacting with LB film (respectively LS film) are shown in the figure 11a (respectively 11b). A hysteresis due to the adhesion force is observed. An adhesion force of 4.59 ± 0.12 nN has been obtained for the LB film and 3.8 ± 0.1 nN for the LS one, on four measurements performed with different tips.

As one can see, the adhesion force measured between the tip and the LB film and the one measured between the tip and LS film are in the same order of magnitude. At this point, we have a demonstration that the loop does not play a

role in term of adhesion force, at least in front of Si_3N_4 tip. However, we will show in the chapter 6 that with Si_3N_4 tip a particular interaction exist with LB film, inducing a particular high friction coefficient, so the particular interaction between both Si_3N_4 and SiO_2 tips may not be due to the adhesion force.

5.4.3.4 Energy dissipation between the tip and hydrophobin films

The aim of this section is to extract the dissipative part of the tip–samples interaction from the amplitude and phase distance (APD) curves. To do so, analytical expression given by the equation 8 is used. This equation gives the power dissipated by the tip-sample interaction as a function of the experimental amplitude and phase lag, when the cantilever is exited at its resonance frequency. It has to be noted that, for each sample, the phase used in the eq. 8 to plot the power dissipation, is the one given in the figure 10, the corresponding oscillation amplitude is also used.

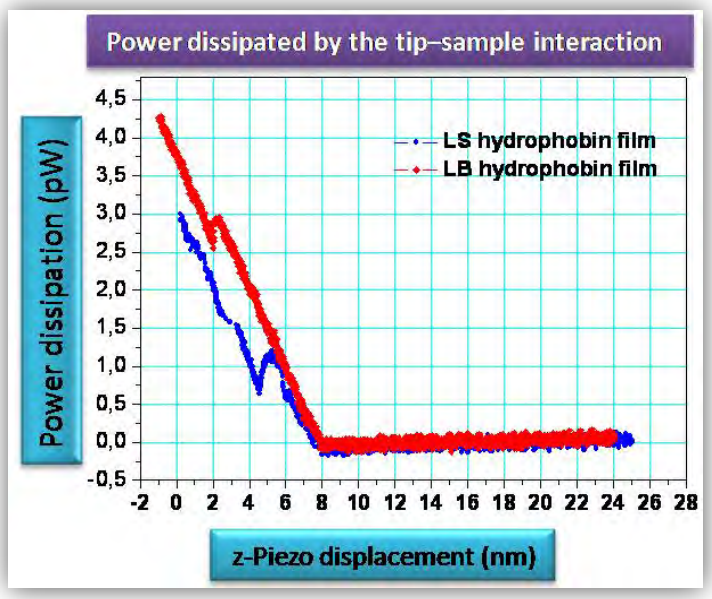

Figure 12. Power dissipated by the AFM tip during approach measurements: red color corresponds to the power dissipated by the tip-LB film interaction, and blue color corresponds to the power dissipated by the tip-LS film interaction.

In figure 12, the power dissipation as a function of the tip-sample distance is plotted for both systems, tip-LS film and tip LB film. The horizontal line

corresponds to the free oscillation amplitude where the tip is still far from surface sample, thus no energy dissipation takes place. The power dissipated by the tip increases when the tip-LB film (respectively tip-LS film) distance is decreased, as expected for soft materials. The dissipated power by the tip-LB film interaction is higher than the one dissipated by the tip interacting with LS film. This result appears surprising if we consider that the energy dissipated by the tip interacting with LB film should be the same that the one dissipated when the tip interacts with LS film since both the films are made from the same molecules. However this result may be interpreted using the assumption given above concerning the difference of the visco-elastic nature between the LB hydrophobin film and the LS one.

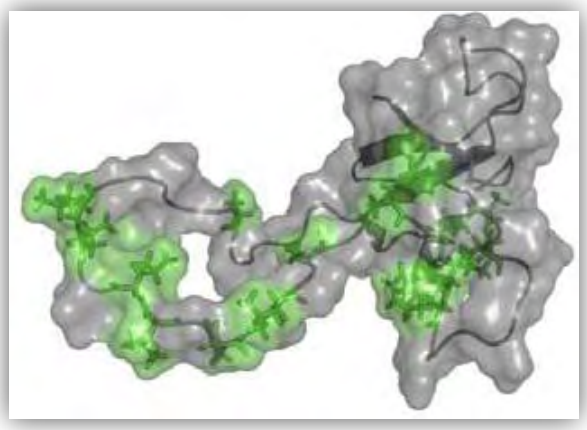

Figure 13. The structure of EAS class I hydrophobin. The hydrophobic amino acids of EAS in this region are shown ingreen [16].

5.4.3.5 Validation of the assumption by numerical simulations

Numerical simulations have been performed by R. D. Rodriguez in order to study the effect of a dissipative layer taking into account vdW attractive interaction, DMT contact interactions [41] as well as a damping within the smple. (see figure 14). It can be seen in the figure 14 that, in the presence of the dissipative thin layer inducing a damping, the jump position is shifted towards the left side together with an increase of the maximal phase value for the LB

film. This is in agreement with experimental results presented above in the figures 9 and 10. This consequently confirms the assumption given above suggesting that the hydrophobin LB film is less rigid that the LS one.

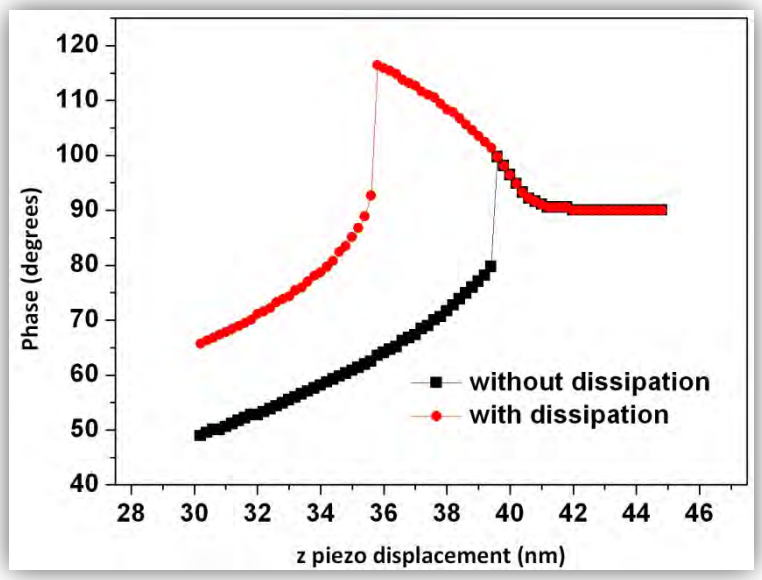

Figure 14. Numerical simulation performed taking into account the vdW and contact mechanics DMT forces (black color), and vdW, contact mechanics DMT and dissipative forces (red coulor).

5.4.4 Phase distance curves on hydrophobin LB monolayer and rodlets

For a more precise understanding of the difference already highlighted in the chapter 4 using AFM phase images between the two types of assemblies formed as hydrophobin LB monolayer and rodlets, the phase distance curves have been performed with the same tip in the same sample containing monolayer and rodlets in dry conditions and at ambient humidity as shown in the figure 15.

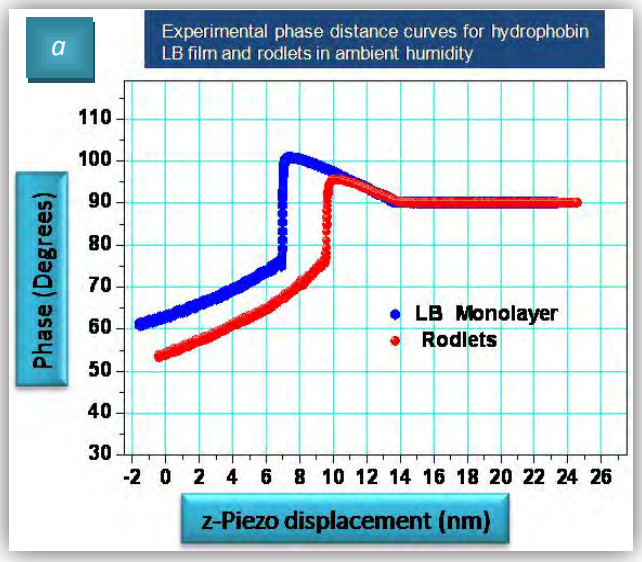

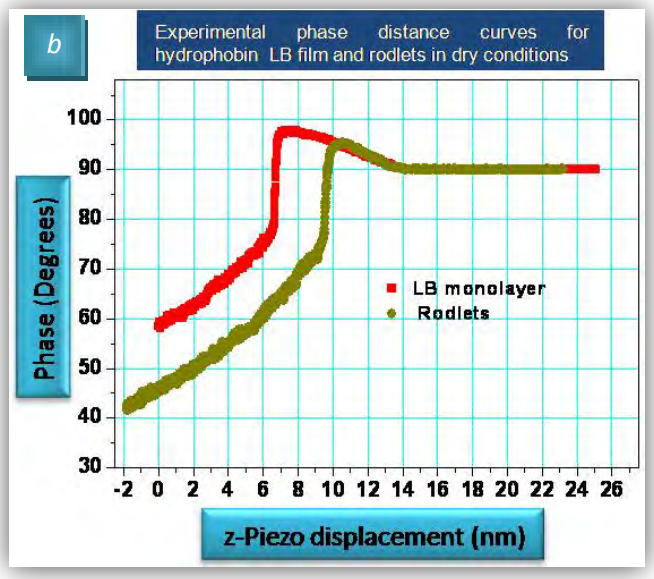

Figure 15. Experimental approach-retract curves performed (*a*): in ambient humidity, (*b*): in dry conditions for LB monolayer and rodlets.

In figure 15 it is shown phase versus distance curves measured for the tip-protein LB monolayer system and the tip–rodlets system in ambient humidity (figure 15*a*) as well as in dry conditions (figure 15*b*). As expected, due to the hydrophobic character of the hydrophobin LB monolayer, the jump position for the tip-LB monolayer system in ambient humidity and in dry conditions is similar. However, we note that the jump position for the tip-rodlets system in ambient humidity and in dry conditions is also similar. This implies that, there

is no humidity effect on the tip-rodlets interaction (i.e. no capillary force effect). This suggests strongly that the top of rodlets is hydrophobic, similarlysimilarly to the top of the monolayer

On the other hand, in the two cases (figure 15), the jump position for LB monolayer appears to be 3 nm after the one of the tip-rodlets system. This difference in the phase behavior confirms that, the surface of hydrophobin LB film and the one of rodlets are certainly different since the tip does not interact in the same way with the LB film and the rodlets. At this point, we have a demonstration that the top of rodlets is hydrophobic, and from the jump position in the phase distance curves (figure 15), the rodlets should be more rigid than the LB monolayer. They do not indeed present a large repulsive regime associated with visco-elastic damping of the tip within the film.

This result supports strongly the hypothesis suggested in the chapter 4 about the formation of rodlets as a hydrophobic monolayer. As we have shown in the chapter 4, the thickness of the rodlets is about two times higher than the one of the LB monolayer. Thus, these results strongly suggest that the vmh2 hydrophobin molecules adopt an extended conformation when they form rodlets as suggested by other authors [42, 22] for SC3 class I hydrophobin molecules. However, the hypothesis of rodlets as bilayer cannot be totally excluded. If the rodlets are bilayer, the two molecules facing each other can simply not be symmetric, leading to two interfaces, one hydrophilic and the other one is hydrophobic.

It has to be noted that, the phase imaging presented in the figure 13 of the chapter 4 and the approach-retract curves shown herein in the figure 15 are performed in the same conditions using the same cantilever-tip system. However the phase difference obtained between the top of rodlets and the surface of monolayer from the phase imaging reported in the chapter 4 was

small (ca. 2°), while the difference highlighted by the phase distance curves presented above in the figure 15 is distinctly visible. The phase curve measurements are then highly recommended for this type of comparison. Indeed, depending in the amplitude *setpoint* value the phase can be similar on rodlets and monolayer (large tip-sample distance), or very different (small tip-sample distance).

5.5 Conclusion

In this chapter, I have investigated using tapping mode AFM the wetting phenomenon of hydrophobin films as a function of humidity. I have demonstrated that the hydrophilic character of LS film can be highlighted at the nanoscale by detecting the meniscus formation between the AFM tip and surface of the monolayer. On the other hand, I have demonstrated no meniscus formation between the tip and the LB monolayer. These results confirm the hydrophobic character and the hydrophilic one of the LB film and the LS film respectively already demonstrated in the chapter 4 by contact angle measurements. The approach-retract curves in tapping mode are the good alternative to study wetting phenomena at the nanoscale without wearing.

In turn, using the harmonic approximation, the Hamaker constant of hydropobin protein was estimated from the phase distance curves. Moreover, by analyzing the phase versus distance curves performed in dry conditions for hydrophobin films, SiO_2 surface and silanized SiO_2 surface, more precisely the region corresponding to the jump from the attractive to the repulsive interactions, I have revealed the existence of a particular interaction in addition to the vdW interaction between the tip and the LB film. This particular interaction is finally shown to be due to the difference in the elastic properties between LB and LS films in particular through the calculation of the dissipation

power and in addition to numerical simulations. By the force curve measurements, I have shown that, no particular adhesion force was revealed between the Si_3N_4 tip and the protein LB film in comparison that the one between the tip and LS film.

On the other hand, the experimental phase distance curves performed for the hydrophobin LB film and the rodlets showed the difference in the jump positions, suggesting that the rodlets are more rigid than the LB monolayer.

Bibliography

[1] T.R. Albrecht, P. Grütter, D. Horne, D. Rugar, J. Appl. Phys. 69 (1991) 668.

[2] G. Binnig, C. F. Quate, and C. Gerber, Phys. Rev. Lett. 56, 930 (1986).

[3] M. Ternes, C. P. Lutz, C. F. Hirjibehedin, F. J. Giessibl, and A. J. Heinrich, Science 319, 1066 (2008).

[4] R. Garcia, R. Magerle, and R. Perez, Nature Mater. 6, 405 (2007).

[5] H. Holscher, Appl. Phys. Lett. 89, 123109 (2006)

[6] Rui Wang, Yan-Lian Yang, Ming Qin, Li-Kai Wang, Lei Yu, Bin Shao, Ming-Qiang Qiao, Chen Wang, Xi-Zeng Feng, *Chem. Mater. (*2007**),** *19,* 3227-3231.

[7] Marcel L. de Vocht, Karin Scholtmeijer, Eric W. van der Vegte,Onno M. H. de Vries, Nathalie Sonveaux, Han A. B. Wösten, Jean-Marie Ruysschaert, Georges Hadziioannou, Joseph G. H. Wessels, George T. Robillard, Biophysical Journal Volume 74 (1998) 2059–2068.

[8] Rahul Misra, Jun Li, Gordon C. Cannon, Sarah E. Morgan, Biomacromolecules 2006, 7, *1463 1470.*

[9] R.D. Rodriguez, Ph.D Thesis, Pierre and Marie Curie University 2008, advisors E. Lacaze and J. Jupile

[10] . Fontaine P., Guenoun P., Daillant J. 11, 1997, Rev. Sci. Instrum., Vol. 68.

[11] J. E. Sader, J. W. M. Chon and P. Mulvaney, Rev. Sci. Instrum., 70, 3967 (1999)

[12] Israelachvili, J.N. *Intermolecular and Surface Forces.* 2nd. s.l. : Academic Press Inc, 1992.

[13] Lifshitz, E. M. Soviet Phys. JETP 1956, 2, 73.

[14] Ackler D.H., French R.H., Chiang Y.M. 1996, Journal of Colloidal and Interface Science, Vol. 179, pp. 460–469.

[15] A.I. Gómez-Merino, F.J. Rubio-Hernández, J.F. Velázquez-Navarro, F.J. Galindo-Rosales, P. Fortes-Quesada, Journal of Colloid and Interface Science 316 (2007) 451–456

[16] Géza R. Szilvay, Ph.D thesis (2007), University of Helsinki, Finland

[17] R. Perez, Y. Stich, M. Payne, and K. Terakura, Phys. Rev. B 58, 10 835 (1998)

[18] Magonov S. N., Elings V., Whangbo M. H. 1997, Surface Science, 385-391.

[19] Lyklema, Fundamentals of Interface and Colloid Science, Vol. 1, Academic Press, 1993.

[20] S. Sounilhac, E. Barthel, and F. Creuzet. 1999, Journal of Applied Physics, Vol. 85, pp. 222-227.

[21] . C. Jai, J.P. Aime, D. Mariolle, R. Boisgard, and F. Bertin. 2006, Nano Letters, Vol. 4, pp. 2554-2560.

[22] Wösten, H.A.B., Asgeirsdottir, S.A., Krook, J.H., Drenth, J.H.H., Wessels, J.G.H., 1994. Eur. J. Cell Biol. 63, 122–129.

[23] Zitzler L, Herminghaus S and Mugele F 2002 *Phys. Rev.* B **66** 155436

[24] Frédéric Caupin, Eric Herbert, Sébastien Balibar, Milton W. Cole. 2008, Chemical Physics Letters, Vol. 463, pp. 283-285.

[25] Adamson, A. W. (1976). Physical chemistry of surface, 3rd ed., Wiley, New York and London

[26] W.J. O'Brien, J.J. Hermann, J. Adhes. 5 (1973) 91.

[27] Fisher, L. R., Israelachvili, J. N. (1981). Colloid surf. 3, 303-319.

[28] O H Pakarinen, A S Foster, M Paajanen, T Kalinainen, J Katainen, I Makkonen, J Lahtinen and R M Nieminen, Modelling Simul. Mater. Sci. Eng. 13 (2005) 1175–1186.

[29] J.P., Anczykowski B., Schmid A.E., Elings V.B. 1998, Applied Physics Letters, Vol. 72, pp. 2613-2615.

[30] Anczykowski B., Gotsmann B., Fuchs H., Cleveland J. P., Elings V. B. 1999, Applied Surface Science , Vol. 140, pp. 376-382.

[31] L. Nony, R. Boisgard, and J. P. Aimé, J. Chem. Phys., Vol. 111, No. 4, 22 (1999).

[32] Ackler D.H., French R.H., Chiang Y.M. 1996, Journal of Colloidal and Interface Science, Vol. 179, pp. 460–469.

[33] . Bergstrom, Lennart. 1997, Adv. Colloid Interface Sci., Vol. 70, pp. 125-169.

[34] A. B. Gurevich, M. K. Weldon, Y. J. Chabal, R. L. Opila, and J. Sapjeta. 1257, 1999, Appl. Phys. Lett. , Vol. 74

[35] Linder MB, Current Opinion in Colloid & Interface Science 14 (2009) 356–363

[36] X. Xiao and L. Qian, *Langmuir* 2000, *16,* 8153-8158

[37] Ann H. Kwan, Ingrid Macindoe, Paul V. Vukašin, Vanessa K. Morris, Itamar Kass, Rima Gupte, Alan E. Mark, Matthew D. Templeton, Joel P. Mackay and Margaret Sunde, J. Mol. Biol. (2008) 382, 708–720

[38] X. Wang, H. P. Permentier, R. Rink, J. A. W. Kruijtzer, R. M. J. Liskamp, H. A. B. Wösten, B. Poolman, G. T. Robillard, Biophysical Journal Volume 87 (2004) 1919–1928.

[39] Hao Fan, Xiaoqin Wang, Jiang Zhu, George T. Robillard, and Alan E. Mark. Proteins: Structure, Function, and Bioinformatics 64:863–873 (2006)

[40] Linder M, Szilvay GR, Nakari-Setala T, Soderlund H, Penttila M, PROTEIN SCIENCE, 11 (2002) Pages: 2257-2266.

[41] Garcia R., Paulo Alvaro San. 7, 1999, Physical Review B, Vol. 60

[42] Zangi , M.L. de Vocht, G.T. Robillard, A.E. Mark: *Biophys J*, **83**(1):112-124, (2002).

6. Nanotribological properties of hydrophobin films

6.1 Introduction

Friction is one of the oldest phenomenon in the history of mankind. It appears in every technical application, going from macro to nanoscale. At macroscopic scale, it is often encountered in daily life, and it is exploited from simple tasks like walking, to modern machinery.

The science of tribology (Greek *tribos*: *rubbing*) concentrates on contact mechanics of moving interfaces that generally involve energy dissipation. It encompasses the science fields of adhesion, friction, lubrication and wear. The first recorded systematic studies of friction were made by Leonardo da Vinci (1452-1519). He measured the friction force F needed to slide a mass M (equivalent to an external load F_l) across a surface [1] and made two important observations: first, he concluded that the friction force doubled when the weight was doubled (i.e., that F was proportional to F_l); second, he concluded that the friction force was independent of the way the objects were positioned on the surface (i.e., that F did not depend on the area of contact A between the moving surfaces). These observations were later confirmed by Amontons (1663-1705) [2], and Coulomb (1736-1806) [3] noted the velocity independence of the friction force. These three observations give the friction coefficient μ as the ratio of the frictional force F to the external load F_l independently of the contact area A and sliding velocity v, as follows: $\mu = F/F_l$ = constant. Bowden and Tabor [4] also investigated friction from the perspective of a purely elastic sliding process. They used a simplified single asperity model of contact based on the *Hertzian*

elastic theory, and found a non-linear friction-load dependence $\left(F \propto F_l^{2/3}\right)$, which clearly contradicted Amontons' law and the experiments conducted at that time. It was Archard [5], who recognized that there was no contradiction between an elastic single asperity model and Amontons' law that is based on a contact that involves many asperities. Instead of assuming a constant number of asperities as Bowden and Tabor did, Archard assumed a load dependent number of asperities. With this assumption the controversy between the elastic multiple asperity hypothesis and Amontons' law could be resolved. Greenwood and Williamson [6] further improved the method with a Gaussian and exponential distributions of asperities. They showed that, for two rough (non-adhering) surfaces having an exponential distribution of asperity heights (all asperities were assumed to have spherical caps of equal radius), the real contact area would indeed be proportional to the applied load if the asperities deformed elastically. For adhering surfaces, Derjaguin [7] proposed the following modified version of Amontons' equation:

$$F = \mu\left(F_l + F_a\right)$$

Equation 1

where a constant term F_a is added to the external load F_l to account for the intermolecular adhesive forces.

6.2 Friction at nanoscale

The understanding of friction on small length scales is becoming increasingly important with the development of AFM technique [8], and the growing field of nanoscience. Thanks to the AFM method, it became possible to explore the physical and tribological properties of engineering and biological surfaces at nanoscale and microscale levels [9, 10]. Indeed, during last decade, the AFM technique has proved to be important tools for nano-tribological experiments,

ranging from proteins [11, 12] to polymeric materials [13, 14]. The basic idea is to exploit the local interactions with a very sharp probe for obtaining microscopic information on surfaces in lateral resolution.

Despite the potential utility of hydrophobin coatings in biotechnology, such as for personal care or biomedical applications, the tribological properties of hydrophobins are very little investigated until now. Only two papers in the literature [15, 16] have discussed the tribological aspect of hydrophobin assembly using the AFM technique. Misra and co-workers [15] have investigated using Si_3N_4 cantilever, thin coatings of SC3 hydrophobin isolated from the fungus *Schizophyllum commune* prepared via spin coating and adsorption techniques onto polymeric surfaces, resulting in the films of 12 nm and 20 nm thicknesses respectively, with hydrophilic side in contact with air. They studied the friction on polymer surfaces and polymeric surfaces modified with Sc3 hydrophobin films and have shown that friction coefficients were dramatically reduced for polymeric surfaces coated by Sc3 film: values in the range of 0.01-0.02 have been obtained for all hydrophobin-coated surfaces, corresponding to 50-80 % reduction in friction in comparison to unmodified polymeric surfaces. On the contrary, by the lateral force image AFM in ethanol solution with the Si_3N_4 cantilever chemically modified with amid groups, de Vocht and co-workers [16] have highlighted a strong interaction between the hydrophilic tip and the SC3 protein layer. As it will be discussed later, in this latter case, SC3 hydrophobin was deposited by incubation onto Teflon substrate with a thickness of 7-8 nm.

In this chapter, we study the friction properties between triangular Si_3N_4 AFM cantilever and hydrophobin films obtained by LS and LB techniques. As we have shown in the chapter 4 and 5 the LS film has the hydrophilic side in contact with air, while in the LB film, the hydrophobic side is in contact with

air. The results have been obtained at ambient conditions, but also in dry atmosphere in order to probe the humidity effect on the friction. The Amontons' law expressed by the Eq. 1 was used for the results interpretation.

6.3 Experimental procedure

The vmh2 hydrophobin protein was purified from the fungus *Pleurotus ostreatus* according to previously described procedures in in the chapter 1.The Langmuir Blodgett (LB) and Langmuir Schaefer (LS) films were prepared as described in the chapter 4. The hydrophobin bilayers were deposited as follows: in order to have a bilayer with hydrophilic surface in contact with air, a monolayer was deposited onto hydrophobin LB film using LS technique (this bilayer is named hereafter LB+LS). By contrast, in order to obtain a bilayer with hydrophobic surface in contact with air, a monolayer was deposited onto hydrophobin LS film using LB technique (this bilayer is named hereafter LS+LB).

AFM measurements were performed using a Nanoscope Dimension 3100 (Veeco Instruments, Santa Barbara, CA). The triangular Silicon Nitride Si_3N_4 probes having a nominal spring constant of 0.06 N/m furnished by *Budget sensor* were used. Friction measurements were obtained by operating the AFM in the friction mode in ambient conditions (i.e. 40 % RH) as well as in dry atmosphere as already described in the chapter 3. In each case, four series of friction measurements were carried out. For each series, the experiments were performed in the same conditions, with the same cantilever, for the purpose of direct comparison.

When the measurements were carried out in dry conditions the microscope was placed in a closed chamber equipped with an inlet for dry nitrogen. Before the measurements, the chamber was purged with nitrogen, and during AFM measurements, the humidity in the chamber was maintained constant at 2% RH.

To perform friction measurements, firstly, the image is centered on the point of interest where the friction measurements will be performed (see figure 1). The friction signal was measured under a constant load using a 90° scan angle, while the normal force acts in the direction perpendicular to both the scan direction and the friction force direction. The measurements were performed at a constant sliding velocity of 0.2 $\mu m.s^{-1}$. To ensure comparisons of friction data, I checked that the AFM tip underwent minimal change during the entire experiment by checking the AFM tip's frictional properties on SiO_2 surface before and after the measurements. Only when the obtained results on SiO_2 surface were the same before and after measurements on the hydrophobin films, I recorded the measured friction data of the samples.

6.4 Result and discussions

6.4.1 Frictional properties of hydrophobin monolayers in ambient humidity

The homogeneity of hydrophobin LB film and hydrophobin LS film were confirmed by AFM contact mode as we can see in the AFM images presented in the figure 1, in agreement with the images obtained in AFM tapping mode, presented in the chapter 4.

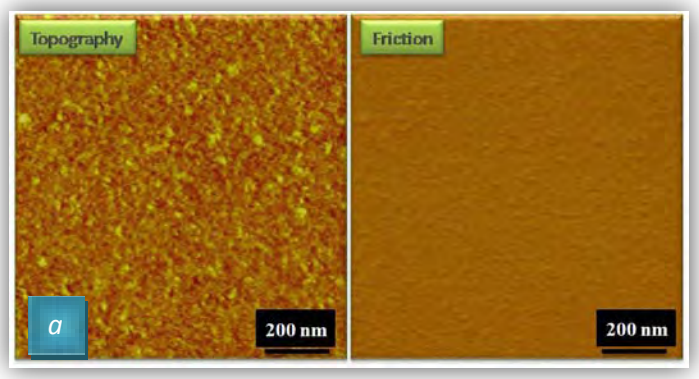

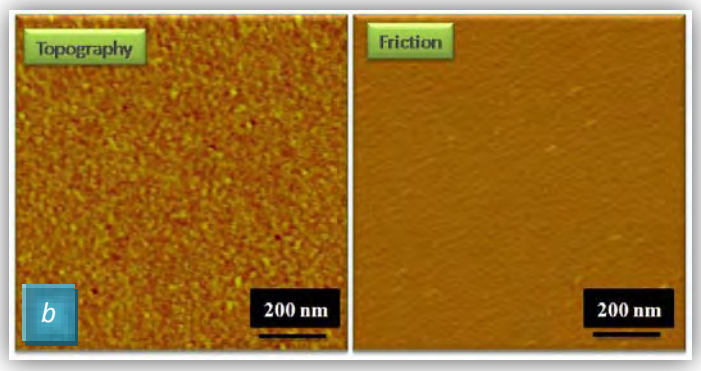

Figure 2. AFM topography and friction images of the obtained films: (a) LB film and (b) LS film, height scale 7 nm.

We have then studied the friction force between the AFM tip and hydrophobin films by recording the lateral torsion of the tip cantilever, while the sample was scanned. The lateral torsion is directly proportional to the signal called TMR (Trace minus Retrace) in the scope mode display according to the calibration method already explained in the chapter 3, The TMR signal measures the voltage difference between the Trace and the Retrace scan directions. This corresponds to the amount of total tip twist that occurs as the tip scans back and forth across the sample. The resulting curve, the so-called friction loop is presented in the figure 2. The gap between the trace and retrace friction curves is reduced for the hydrophobin LS monolayer as well as SiO_2 surface, indicating reduction in friction for these samples in comparison to the hydrophobin LB one.

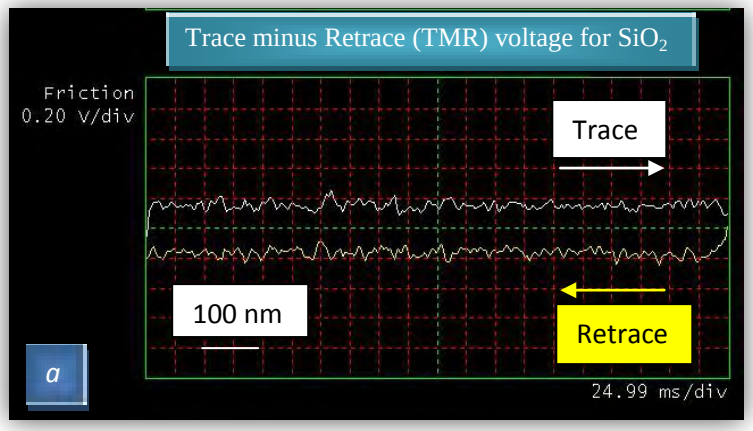

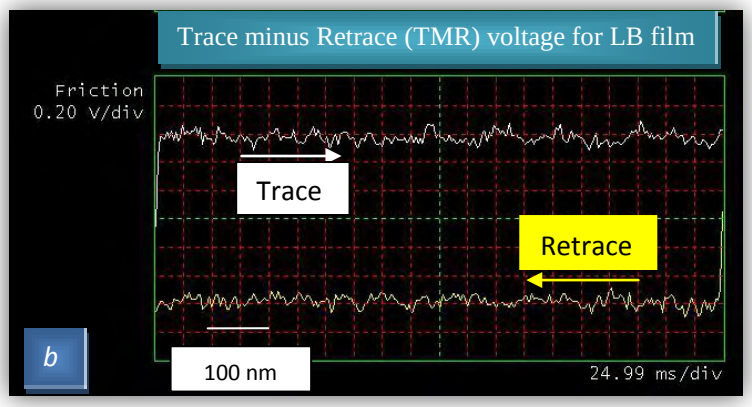

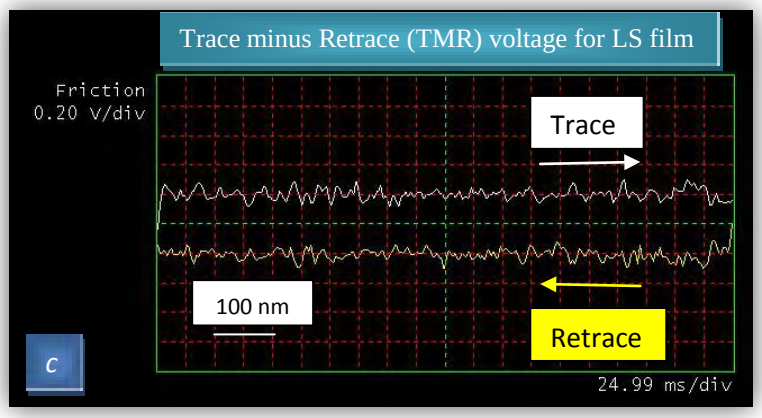

Figure 3. typical friction loops giving TMR voltage for (*a*) SiO2 surface, (*b*) hydrophobin LB film and (*c*) hydrophobin LS film performed in ambient humidity at the setpoint 2 v.

In varying the applied load F_l and recording the friction force F, we have found that the force F varies linearly with the applied load F_l for all samples, as it can be seen in the figure 3. The friction coefficients were obtained from the slope of a plot of F as a function of F_l and summarized in Table 1.

In AFM measurements we should be in the situation of the single asperity contact. However, we find linear friction-load dependence for all samples. In disagreement with the single asperity model, based on the *Hertzian elastic theory*. This can be explained by the fact that the soft nature of the protein films leads to the multi-asperity contact. On the other hand, for SiO_2 surface, the

multi-asperity contact situation may be caused by the presence of the meniscus between the tip and the sample.

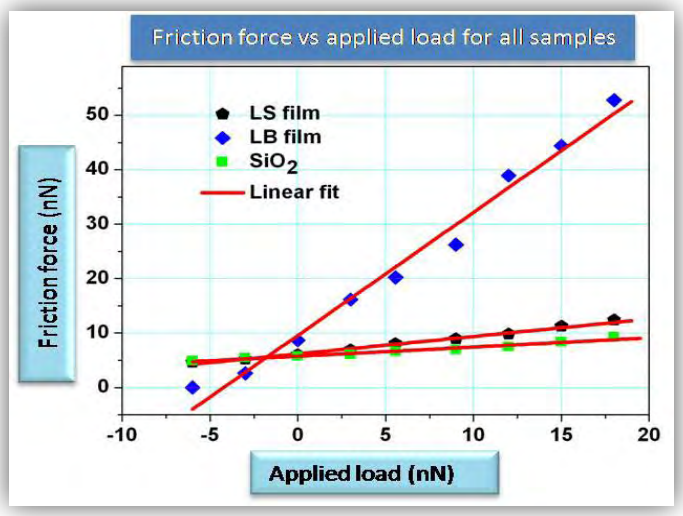

Figure 4. The friction force vs applied load data recorded for SiO2, hydrophobin LB film and hydrophobin LS film in ambient conditions.

Sample	Friction coefficient (μ_1)	Friction coefficient (μ_2)	Friction coefficient (μ_3)	Friction coefficient (μ_4)
SiO_2	0.16	0.19	0.11	0.31
LB film	2.26	3.9	0.25	3.24
LS film	0.32	0.23	0.17	0.4

Table 1. Values of the obtained friction coefficient for SiO_2 surface, hydrophobin LB monolayer and hydrophobin LS monolayer in ambient conditions. μ_1 are obtained from the figure 3; μ_2, μ_3, μ_4 were taken from the fit of data measured during other AFM sessions , performed with different tips

An example of the obtained friction force vs applied load is presented in the figure 3. The surface of hydrophobin LS monolayer demonstrates very low friction, with reductions in the friction coefficient in comparison to that measured for the hydrophobin LB film. Except μ_3 (column 4 in the table 1), for the LB monolayer, the friction coefficients are about a factor 10 higher than those obtained for the LS monolayer. Furthermore, the surface of hydrophobin LS and SiO_2 sample yield similar friction coefficient. From these measurements,

we note on one hand that, the LB film presents a specific tribological behavior in interaction with the Si_3N_4 tip. On the other hand, friction coefficients were measured repeatedly over a period of several weeks with consistent results obtained in all measurements indicating stable attachment of vmh2 hydrophobin onto SiO_2 and silanized SiO_2 surfaces, as well as stable surface properties.

6.4.2 Effect of relative humidity on the of friction coefficient for hydrophobin films and SiO_2 Surfaces.

In the chapter 5 we have demonstrated that, during AFM measurements, the capillary meniscus can be formed between the SiO_2 tip and the LS film, but also between the SiO_2 tip and SiO_2 surface in ambient humidity. We can then ask the question about the role of capillarity on the friction between the Si_3N_4 tip and samples. We have consequently performed the friction measurements in dry conditions (2 % RH) in order to study the relative humidity (RH) effect on the tribological behavior of hydrophobin films and SiO_2 surface. A typical curve of friction force versus applied load, in dry condition, is presented in the figure 4 below. As we can see in the figure 4, the friction force varies linearly with the applied load for all samples. The friction coefficient is then again deduced from the plot. The obtained results for all experiments performed in dry conditions are summarized in Table 2.

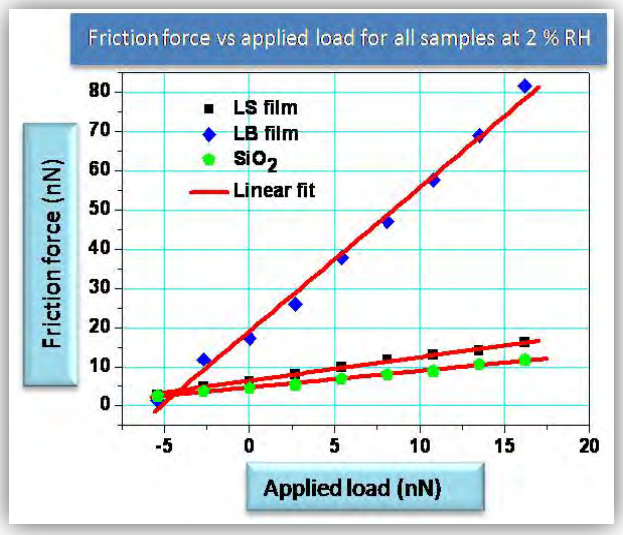

Figure 5. The friction force vs applied load data recorded for SiO2, hydrophobin LB film and hydrophobin LS film in dry conditions.

Sample	Friction coefficient (μ_1)	Friction coefficient (μ_2)	Friction coefficient (μ_3)	Friction coefficient (μ_4)
SiO_2	0.41	0.35	0.42	0.47
LB film	2.91	2.74	3.66	3.24
LS film	0.67	0.44	0.6	0.53

Table 2. Values of the obtained friction coefficient for SiO_2 surface, hydrophobin LB monolayer and hydrophobin LS monolayer in dry conditions. μ_3 are obtained from the figure 4; μ_1, μ_2, μ_4 were taken from the fit of data measured during other AFM sessions (not shown in the text).

From data presented in the table 1 and 2, we note that the friction coefficients obtained for SiO_2 surface against Si_3N_4 tip, are in the same order of magnitude that the results found in the literature [17]. Moreover, even in absence of capillarity, the behavior of the friction force versus applied load is linear; this suggests that definitely, a Hertz contact does not correctly describe the contact interaction between tip and surface in AFM experiments even for hard surfaces as the SIO2 one. On the other hand, the results presented in the table 2 show that, on the SiO_2 surface and the hydrophobin LS film the friction coefficients are widely lower than those obtained on hydrophobin LB film. This is consistent with the obtained results in ambient conditions presented in the table 1. However, it can be noted that, in dry condition there is some increase in the

friction coefficients obtained for Si_3N_4 tip-SiO_2 surface and Si_3N_4 tip-LS film; they are about two times larger than those measured in ambient conditions. This may be due to the presence of layer of water molecules bound to the surface. Thus, in ambient humidity, for LS film and SiO_2 surface, the interaction between the surface and the tip is mediated by the water layer. In this case, the water can act as a lubricant resulting in the low viscosity in the surface of sample, while in dry conditions there is no lubricant. The fact that similar influence of humidity is obtained for SiO2 and LS hydrophobin film is consistent with the observation of similar hydrophilic properties, as demonstrated in chaper 4. Binggeli et al. [18] have studied the influence of capillary condensation and humidity to friction on a hydrophilic SiO_2 surface against a tungsten cantilever at relative humidity below 75 %, no dependence of humidity was observed, whereas at humidity level above 75 % a dependence of the friction properties on the humidity was clearly observed: when the relative humidity increases, above 75%, the friction coefficient decreases and values ranging from 0.25 to 0.5 were obtained. The difference in the onset of the humidity effect between their system and ours is certainly attributed to the fact that they used a tungsten cantilever instead a Si_3N_4 cantilevers which we have used in our experiments, resulting in the difference in the sensitivity and hydrophilicity. It suggests that the tungsten tip is more hydrophobic than the Si_3N_4 one, leading to the formation of meniscus between tip and sample for lower humidity in this latter case. It is also interesting to observe that friction coefficient are modified with humidity for LS film and SiO2, since it demonstrates that, similarly to SiO2 tips, with Si_3N_4 tips, a meniscus is formed at ambient humidity.

On the other hand, the frictional properties of the LB film against the Si_3N_4 in dry conditions are almost the same that those obtained in ambient atmosphere,

which means that; they remain insensitive to the humidity effect. This is due to the hydrophobic character of the surface of the hydrophobin LB film that is insensitive to the humidity level. This data confirms the obtained result in the chapter 5 by the phase versus distance curves, highlighting the hydrophobic nature of the LB film. This is also consistent with contact angle measurements shown in the chapter 4.

We have then seen a large difference between the frictional properties of the hydrophobin samples. The hydrophobic part (LB) of the hydrophobin monolayer presents a higher friction coefficient with respect to the hydrophilic (LS) part of the protein monolayer, whether in ambient humidity or in dry conditions. This is Interesting because, as we have seen in the chapter 5, we have shown that the LB film presented a specific interaction with the SiO_2 tip in tapping mode, and demonstrated that this interaction is due to the elastic nature of the hydrophobin LB film that appears less rigid than the LS one. Thus, the higher friction coefficient measured for the LB film can be associated with the same physical characteristic, a high viscoelasticity at the air interface which does not exist for the LS film.

De Vocht et al. [16] have studied the Sc3 hydrophobin deposited by incubation onto Teflon substrate resulting on 7-8 nm thick, by the lateral force microscopy and found that the Si_3N_4 AFM tip chemically modified with amid groups, interacts strongly with the hydrophilic side of the hydrophobin. They explained this behavior by the softness of the protein film and by the hydrophilic nature of the surface after binding of SC3 to a hydrophobic substrate. We report here that LS films which are hydrophilic interact similarly to the SiO2 surface. Anyway we demonstrate, in agreement with Binggeli et al. [18] that the presence of a water layer decreases the friction between tip and surface. Consequently, if the hydrophilicity of hydophobin is associated with strong

interactions between tip and surface in friction experiments, this has to be related to particular chemical interactions between modified tips and substrate. Moreover we demonstrate, through our results, that the geometry of hydrophobin molecules has to be well controlled with respect to the tip, since different orientations for identical film thickness can induce considerable variation of tip-sample interactions and consistently variation of friction, The result of De Vocht et al [16] has consequently to be considered carefully: the thickness of the hydrophobin coating when deposited by incubation onto solid surface cannot be well controlled and probably the geometry as well. By contrast the Langmuir technique allows to obtain well known thickness and even more importantly, well-defined geometries.

6.4.3 Frictional properties of hydrophobin bilayers

In order to study the frictional properties of hydrophobin as bilayer deposited onto solid substrate, we have deposited hydrophobin bilayers onto SiO_2 substate and silanized SiO_2 surface respectively according to the procedure explained in the experimental procedure. A typical curve of the friction force versus applied load for hydrophobin bilayers is presented in the figure 5.

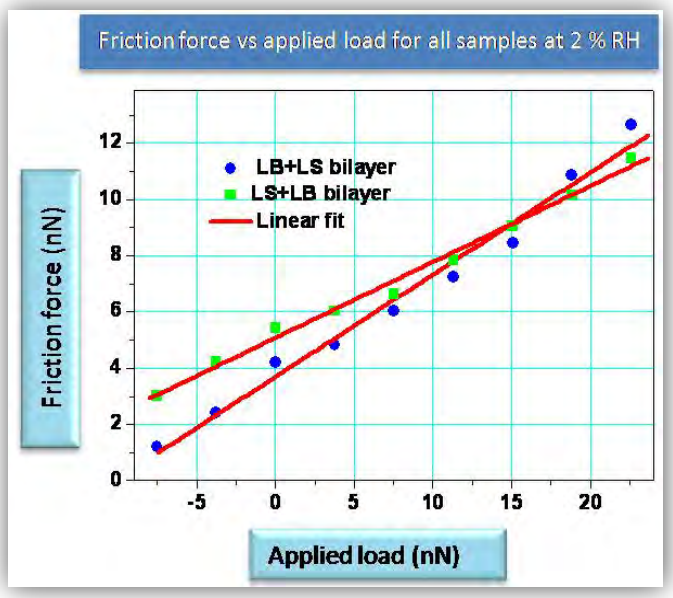

Figure 6. The friction force vs applied load data recorded for hydrophobin bilayers in dry conditions. For clarity the friction force of SiO_2 is not shown.

Sample	Friction coefficient (μ_1)	Friction coefficient (μ_2)	Friction coefficient (μ_3)	Friction coefficient (μ_4)
SiO_2	0.41	0.47	0.35	0.32
LB + LS bilayer	0.32	0.30	0.25	0.16
LS + LB bilayer	0.27	0.36	0.31	0.21

Table 3. Values of the obtained friction coefficient for hydrophobin bilayer in dry conditions. μ_1 are obtained from the figure 5; μ_2, μ_3, μ_4 were taken from the fit of data measured during other AFM sessions (not shown in the text).

The friction coefficients obtained from the friction force versus applied load curves are summarized in the table 3. We note on one hand that, hydrophobin bilayers presented low friction coefficients in both cases, on the other hand they are very similar for both systems. The obtained values are finally close to the friction coefficient of LS films. Furthermore, as we can see in the AFM images presented in the figure 6, the topography of the samples are very similar. This suggests strongly that, at least in one of the two systems, the hydrophobin molecules change the conformation, hence, they restructured when the bilayer is formed, leading probably to the same side in contact with air in both systems.

The low friction highlighted between the tip and hydrophobin bilayers is very likely a result of adopting a compact and rigid bilayer.

It would be now extremely interesting to compare more generally the properties of these bilayers with the one of rodlets themselves (approach-retract curves in particular but also presence of β-sheet) to evidence if their structure is finally equivalent or not. The rigidity of the bilayers must be verified by approach-retract curves in the future, as well as their hydrophilicity or hydrophobicity. Depending on the results, it could be a way to evidence how the hydrophobin loops interact between each other in bilayers structure, which could be a clue of rodlets structure themselves. Finally these results confirm the fact that with hydrophobins it would be extremely difficult to build multi-layers of controlled geometry, as already found for systems where 16 layers of hydrophobins has been deposited on SiO_2 surface by the LB technique, leading to extremely inhomogeneous systems [19].

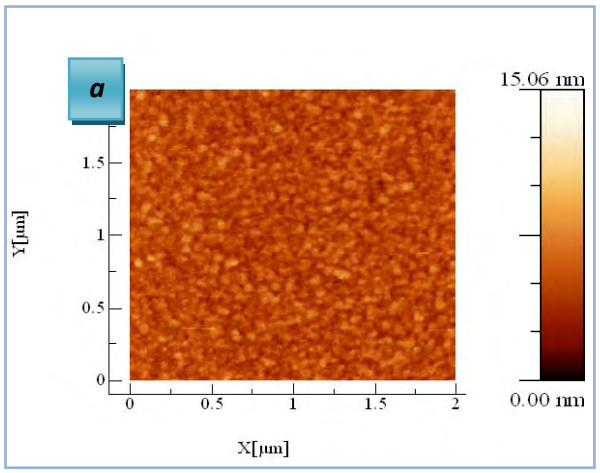

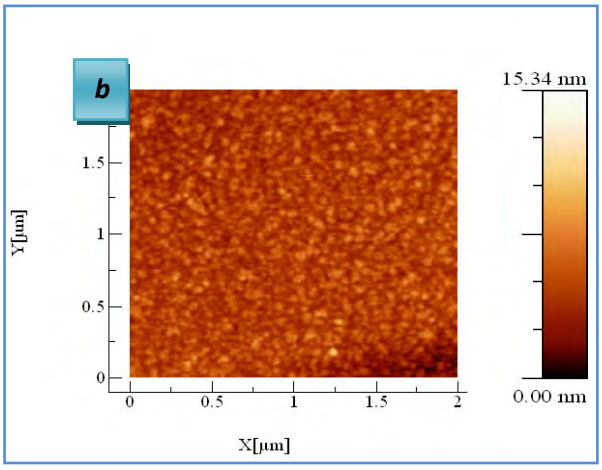

Figure 7. AFM topography images of the obtained bilayers: (a) bilayer deposited onto silanized SiO2 surface by LS+LB and (b) bilayer deposited onto SiO2 surface by LB+LS.

6.5 Conclusion

Thin films of vmh2 hydrophobin were prepared via Langmuir technique. Nanotribological analysis using lateral force microscopy with Si_3N_4 cantilever indicates very low friction coefficient for LS hydrophobin monolayer surface in comparison to the LB one. The obtained results for LS monolayer are comparables to those obtained for SiO_2 surface. The friction coefficient measured for LS film and SiO_2 surface in dry atmosphere (2% RH), are slightly larger than those measured in ambient conditions, suggesting that in ambient conditions the water can act as a lubricant between the tip and these hydrophilic samples, while in dry condition, the absence of water suppresses lubricating effect. By contrast, no humidity effect was observed for the LB monolayer confirming the hydrophobic character of this sample. On the other hand, we have shown that the friction coefficient for hydrophobin bilayers is low, whether deposited by LB + LS or LS +LB transfer, suggesting the formation of similar, compact and rigid bilayers.

The results indicate that for future biomedical applications requiring lubricious, low-friction surfaces, LS film and bilayers of hydrophobin are privileged for use.

Bibliography

[1] Dowson, D. *History of Tribology*; Longman: London, 1979.

[2] Amontons, G. *Mémoires de l'Académie Royale A*; 1699, pp 257- 282.

[3] Coulomb, C. A. *Mém. Math. Phys. (Paris)* **1785**, 161.

[4] Bowden F. P.; Tabor, D. *Proc. R. Soc. London* **1939**, *A169*, 391.

[5] Archard, J.F., 1953. "Contact and rubbing of flat surfaces". *Journal Applied Physics,* **24**(8), pp. 981–988.

[6] Greenwood, J. A.; Williamson, J. B. P. *Proc. R. Soc. London* **1966**, *A295*, 300.

[7] Derjaguin, B. V. *Z. Phys.* **1934**, *88*, 661.

[8] Binnig, G.; Quate, C. F.; Gerber, Ch. *Phys. Re*V. *Lett*. **1986**, *56*, 930.

[9] Bhushan, B.; Israelachvili, J. N.; Landman, U. *Nature* **1995**, *374*, 607.

[10] Leckband, D.; Israelachvili, J. N. *Quart. Re*V. *Biophys*. **2001**, *34*, 105.

[11] Viscoelastic Study of the Mechanical Unfolding of a Protein by AFM Masaru Kawakami, Katherine Byrne, David J. Brockwell, Sheena E. Radford, and D. Alastair Smith, Biophysical Journal: Volume 91, Pages L16-L18 (2006).

[12] Stretching, Unfolding, and Deforming Protein Filaments Adsorbed at Solid-Liquid Interfaces Using the Tip of an Atomic-Force Microscope, Douglas B. Staple, Marko Loparic, Hans Jurgen Kreuzer, and Laurent Kreplak, Physical Review Letters, 102, 128302 (2009).

[13] Determination of viscoelastic moduli at a submicrometric scale, EUROPEAN PHYSICAL JOURNAL-APPLIED PHYSICS**,** C. Basire, C. Frétigny, Volume: 6 Pages: 323-329, (1999)

[14] Michel, D.; Kopp-Marsaudon, K.; Aime, J. *Tribol. Lett.* 1998, *4*, 75- 80.

[15] Nanoscale Reduction in Surface Friction of Polymer Surfaces Modified with Sc3 Hydrophobin from Schizophyllum commune Rahul Misra, Jun Li, Gordon C. Cannon, Sarah E. Morgan, Biomacromolecules 2006, 7, *1463 1470.*

[16] Structural Characterization of the Hydrophobin SC3, as a Monomer and after Self-Assembly at Hydrophobic/Hydrophilic Interfaces, Marcel L. de Vocht, Karin Scholtmeijer, Eric W. van der Vegte,Onno M. H. de Vries, Nathalie Sonveaux, Han A. B. Wösten, Jean-Marie Ruysschaert, Georges Hadziioannou, Joseph G. H. Wessels, George T. Robillard, Biophysical Journal Volume 74 (1998) 2059–2068.

[17] Tribological properties of self-assembled monolayers and their substrates under various humid environments, Linmao Qian, Fang Tian, Xudong Xiao, Tribology Letters, Vol. 15, No. 3 (2003).

[18] Influence of capillary condensation of water on nanotribology studied by force microscopy, M. Binggeli, C. M. Mate, Appl. Phys. Lett. 65 (4), (1994).

[19] Kisko K, Torkkeli M, Vuorimaa E, Lemmetyinen H, Seeck OH, Linder MD, Serimaa R, Langmuir–Blodgett films of hydrophobins HFBI and HFBII. Surf Sci 2005; 584:35–40.

7. Conclusion

In this thesis, we have investigated the formation and the features of Langmuir films of class I hydrophobin from *Pleurotus ostreatus*. Compression-expansion cycles and constant pressure measurements demonstrated that the film at the air-water interface exhibits a molecular depletion toward the subphase. As a consequence, the number of molecules at the interface, and hence the area per molecule are unknown. In order to estimate the surface molecular concentration we analyzed the experimental pressure-area isotherms using a 2D equation of state Volmer-like. Moreover, when the Langmuir films are transferred onto solid substrates by LB and LS techniques, AFM observations revealed the formation of homogenous films with lower roughness. Furthermore, AFM images of the hydrophobin film after repeated compression cycles showed rodlets coexisting with LB monolayer. From these measurements we were able to estimate the rodlets size and the monolayer thickness: we suggest two possible models for rodlets formation: (i) the observed rodlets are actually formed by hydrophobin bilayers embedded in the LB monolayer. In this case, the observed rodlets could be hydrophilic supporting the hypothesis about a possible depletion mechanism occurring at least partly through the formation of hydrophilic rodlets. (ii) The rodlets can be formed as monolayer. In this case, the upper surface of rodlets should be hydrophobic when the film is deposited by LB technique suggesting that the protein adopts an extended conformation when the rodlets are formed.

On the other hand, I have investigated using tapping mode AFM the wetting phenomenon of hydrophobin films as a function of humidity. I have demonstrated that the hydrophilic character of LS film can be highlighted at the

nanoscale by detecting the meniscus formation between the AFM tip and surface of the monolayer. On the other hand, I have demonstrated no meniscus formation between the tip and the LB monolayer. These results confirm the hydrophobic character and the hydrophilic one of the LB film and the LS film respectively already demonstrated in the chapter 4 by contact angle measurements. The approach-retract curves in tapping mode are the good alternative to study wetting phenomena at the nanoscale without wearing. This method has also been used to analyze hydrophilicity of the rodlets. It finally revealed an equivalent hydrophobicity of LB film and rodlets at least partly in disagreement with hypothesis (i).

In turn, using the harmonic approximation, the Hamaker constant of hydrophobin protein was estimated from the phase distance curves. Moreover, by analyzing the phase versus distance curves performed in dry conditions for hydrophobin films, SiO_2 surface and silanized SiO_2 surface, more precisely the region corresponding to the jump from the attractive to the repulsive interactions, I have revealed the existence of a particular interaction in addition to the vdW interaction between the tip and the LB film. This particular interaction is finally shown to be due to the difference in the elastic properties between LB and LS films in particular thorough the calculation of the dissipation power and in addition to the numerical simulations. Indeed, using force curve measurements in contact mode, I have shown that, no particular adhesion force is observed between the Si_3N_4 tip and the protein LB film in comparison that the system tip-LS film.

On the other hand, the experimental phase distance curves performed for the hydrophobin LB film and the rodlets revealed a strong difference in the jump positions of both systems, demonstrating that the rodlets are more rigid than the LB monolayer. These results finally appear in agreement with hypothesis

(ii) whereas it can not be excluded that rodlets are bilayer with the second layer of hydrophobins in a different conformation with respect to the first layer.

It will be now very interesting to study Langmuir films of HFBII class II hydrophobins using the force spectroscopy measurements, since the molecular structure of this protein is well known and the loops that are formed between the strands in the β-barrel structure are much smaller in comparison with the ones in the classe I hydrophobins. This could allow to understand precisely the role of these loops in the LB film and to better control how visco-elasticity take place in phase-distance curves.

Nanotribological properties of hydrophobin films were also investigated using the lateral force microscopy with Si_3N_4 cantilever. We have demonstrated very low friction coefficient for LS hydrophobin monolayer surface in comparison to the LB one. The obtained results for LS monolayer are comparable to those obtained for SiO_2 surface. The friction coefficient measured for LS film and SiO_2 surface in dry atmosphere (2% RH), are slightly larger than those measured in ambient conditions, suggesting that in ambient conditions the water can act as a lubricant between the tip and these hydrophilic samples, while in dry condition, the absence of water suppresses lubricating effect. By contrast, no humidity effect was observed for the LB monolayer confirming the hydrophobic character of this sample. The high friction coefficient obtained for LB films have finally been attributed to the presence of visco-elasticity interactions between tip and surface, similarly to the situation of approach-retract curves. On the other hand, we have shown that the friction coefficient for hydrophobin bilayers is low, whether deposited by LB + LS or LS +LB transfer, suggesting the formation of similar, compact and rigid bilayers.

It will be now very interesting to study the frictional properties of hydrophobin rodlets in order to compare to the frictional properties of bilayers and to well

understand how the bilayers are formed. In particularly similarities between bilayers and rodlets have been demonstrated suggesting, at least, a strong interactions between the two hydrophobin layers in this system. It will be important to test further the similarity/difference between bilayers and rodlets.

Generally speaking, these measurements have demonstrated how powerful can be AFM for measurements of surface physico-chemical properties, beyond the simple topography. Due to the preparation of Langmuir films of well defined geometries and hydrophilicities, the physico-chemical properties of monomolecular films have been revealed, but also the ones of more complex assemblies, as rodlets ones, as well as the induced tribological properties.